Multiscale Modelling of Twin Roll Casting

Yi Qiu

Supervisors: Hamid Assadi, Zhongyun Fan

Brunel Centre for Advanced Solidification Technology (BCAST)

A thesis submitted in partial fulfilment of the requirements for the degree of
Doctor of Philosophy at Brunel University London

January 2021

Abstract

Twin roll casting (TRC) is an emerging material processing technique to manufacture thin metal strips directly from liquid metal. Formation of unfavourable microstructural features during TRC, such as centreline segregation and columnar grains, prompted experimental and modelling studies on the effects of various casting conditions on the as-cast microstructures of different alloys. Previous modelling work focuses on low speed TRC with large rolling effect. By increasing nuclei density in the melt, via addition of grain refiners or melt conditioning, the effect of solidification can be significantly improved.

This thesis concerns the development and application of multiscale multiphysics modelling techniques to provide an insight into the evolution of microstructure during solidification processing of metals, with a focus on twin-roll casting of thin strips of light alloys. The effects of various casting conditions on the as-cast microstructures are investigated using the multiscale model.

The first part of the multiscale model is a macroscale thermal-mechanical model, which predicts the temperature and stress distributions developed in the metal strips during TRC, under the influence of various casting conditions, including casting speed, roll temperature and air convection. The theoretical maximum casting speed is calculated from a quasi-1D solidification model, which can be used to give a guideline for casting conditions used in models and experiments.

The second part is a microscale model which predicts the as-cast microstructure, via a phase field-Potts model which simulates the evolution of phase field, alloy concentration and grain orientation during solidification, coupled with a Bingham lattice Boltzmann model which simulates the velocity field in fluid flow. The temperature profile obtained from the macroscale model is used as the thermal boundary condition of the microscale model.

To validate the model, temperature data obtained from experiments of Al and Mg TRC is compared with the results of the macroscale model. More experimental data of the as-cast microstructure and texture is required to validate the microscale model.

Conferences and Publications

1. Y. Qiu, H. Assadi and Z. Fan. Modelling of Microstructure Evolution in Twin-Roll Casting of Magnesium, Proceedings of the 5th Decennial International Conference on Solidification Processing, 2017.
2. Y. Qiu, H. Assadi and Z. Fan. Macroscale Modelling of the Twin Roll Casting Process (conference presentation), Mg2018: 11th International Conference on Magnesium Alloys, 2018.
3. Y. Qiu, H. Assadi and Z. Fan. Multiscale Modelling of Twin Roll Casting (poster), 5th International Conference on Advances in Solidification Processes, 2019.

Abbreviations and Symbols

Abbreviation

BC	Boundary condition
CET	Columnar to equiaxed transition
FEM	Finite element model
LBM	Lattice Boltzmann model
MC	Melt conditioning
TRC	Twin-roll casting
SSM	Semisolid metal

Symbol

p_i	Pressure field of fluid *i*
ρ_i	Density of fluid *i*
η_i	Viscosity of fluid *i*
u_i	Velocity of fluid *i*
SF_{sing}	Singular surface tension force at the interfaces
g	Gravitational acceleration
f	Particle distribution function
f^{eq}	Equilibrium distribution function
Ω_f	Collision operator
ξ	Microscopic velocity
τ	Non-dimensional relaxation time
τ_f	Relaxation time
c_i	Lattice velocities in direction *i*
δx	Lattice spacing
Q	Discharge
u	Macroscopic velocity
ρ	Macroscopic density
F	Ginzburg-Landau type free energy

f	Bulk free energy function
ϕ	Phase field parameter
W	Diffuse thickness parameter
M	Mobility constant
$\sigma(\theta)$	Anisotropy function
δ	Strength of anisotropy
θ	Grain orientation angle
T	Temperature
v	Velocity
$\tau_{\alpha\beta}$	Shear stress
$\dot{\gamma}_{\alpha\beta}$	Shear rate
μ	Plastic viscosity
τ_y	Yield stress
$\Pi_{\alpha\beta}$	Momentum flux tensor

Table of contents

Abstract 1

Conferences and Publications 2

Abbreviations and Symbols 3

Table of contents 5

List of Figures 8

1. Introduction **12**

- 1.1. Background and motivation 12
- 1.2. Research objectives 13
- 1.3. Thesis outline 14

2. Literature review **16**

- 2.1. Previous work on twin roll casting 16
- 2.2. Fluid Flow Modelling 18
  - 2.2.1. Navier-Stokes Equations 18
  - 2.2.2. Lattice Boltzmann Method 19
    - 2.2.2.1 Lattice Boltzmann models for immiscible two-phase flows 21
    - 2.2.2.2 Forcing schemes in lattice Boltzmann models 27
    - 2.2.2.3 Boundary conditions in lattice Boltzmann models 28
    - 2.2.2.4 Lattice Boltzmann models for unstructured grids 31
  - 2.2.3. Comparing Traditional Navier-Stokes Solvers with the Lattice Boltzmann Method 33
- 2.3. Modelling of Solidification 34
  - 2.3.1. Phase Field Method 34
    - Phase field model for alloy solidification 35
  - 2.3.2. Modelling Dendritic Growth 36
  - 2.3.3. Modelling Polycrystalline Solidification and Grain Rotation in the Presence of Melt Convection 38
    - 2.3.3.1. Problems with the Grain Orientation Evolution Model 41
  - 2.3.4. Approaches to Solving the Phase Field Equation 43
    - 2.3.4.1. Spectral Method 44
    - 2.3.4.2. Lattice Boltzmann Method 45
  - 2.3.5. Comparing Different Solvers of the Phase Field Equation 47

2.4. Coupling Fluid Flow with Phase Field Modelling 48
  2.4.1. Free Energy Model 48
  2.4.2. Hybrid Lattice Boltzmann Finite Volume Method 50
  2.4.3. Phase Field-Lattice Boltzmann Method for Modelling Dendritic Growth with Melt Convection 52
2.5. Previous models of rheological behaviour of semisolid metal slurries 53
3. Multiscale model 56
3.1. Multiscale model outline 56
3.2. Reasons for using a multiscale model 56
4. Macroscale model 58
4.1. FEM model description 58
4.2. Model parameters 59
4.3. Material parameters 59
4.4. Parameter studies 60
5. Microscale model 63
5.1. Fluid flow model 63
  5.1.1. Modelling motion of solid grains in fluid flow in a continuous domain 63
  5.1.2. Bingham fluid model 64
  5.1.3. A modified incompressible lattice Boltzmann model for Bingham fluid 64
5.2. Phase field-Potts model 67
6. Coupling Models and Different Length Scales 69
6.1. Implementation of the LB model and coupling to phase field-Potts model 69
6.2. Coupling FEM and microlevel models 70
  6.2.1 Thermal boundary conditions 70
    Example of implementation 71
  6.2.2 TRC geometry 73
  6.2.3 Velocity boundary conditions 73
7. Macroscale model results and discussion 75
7.1. Calibration of thermal conductance at roll-strip interface 75
7.2. Effects of casting speed 78
7.3. Effects of roll temperature 80
7.4. Quasi-1D solidification model for pure systems 81

7.5. Effects of air cooling 85
8. Microscale model results and discussion 90
8.1. Bingham LB model 90
Effects of Bn and λ on velocity profiles 90
Effects of domain size on the velocity fluctuations 93
Effects of inlet velocity on the velocity fluctuations 94
Implications for microscale model 95
8.2. Phase field-Potts model 96
8.2.1. Floating dendrite 96
8.2.2. Pinned dendrite 98
9. Multiscale model results and discussion 99
9.1. Multiscale model 99
9.1.1 Input from the macroscale model 99
9.1.2 Model set-up and material parameters 99
9.2. Effects of Bingham LBM model parameters 102
9.3. Effects of surface nucleation 103
10. Experimental verification 105
10.1. Verification of macroscale model 105
11. Impact on TRC manufacturing practices 110
11.1 Macroscale model 110
11.2 Microscale model 110
12. Summary 112
13. Further developments 113
References 115
Appendix 1. Material properties used in the macroscale model 121
1.1. Mg material *properties* 121
1.2. Al material *properties* 130
1.3. AZ31 material *properties* 132

List of Figures

Figure 1. Schematics of the solidification mechanism for (a) TRC and (b) MCTRC samples [4] 12

Figure 2. Lattice velocity indexing in the D2Q9 lattice [23] 20

Figure 3. Study of the lattice pinning problem: comparison of results from recolouring operators by Reis and Phillips (Particle I) and by Leclaire et al. (Particle II), and the analytical solution [31] 26

Figure 4. Schematics of lattice nodes at inlet and outlet regions [39] 29

Figure 5. Comparison of discharge Q at the inlet and outlet of a straight channel [39] 31

Figure 6. Schematic showing the 1-ring neighbourhood of points P_k around a grid point P. The green regions represent the finite volumes defined around point P [35] 31

Figure 7. The change in order parameter at a diffuse interface [48] 34

Figure 8. Double well potential f controlled by parameter m [49] 36

Figure 9. Crystal growth with different latent heat values [49] 37

Figure 10. Crystal growth with different strengths of anisotropy [49] 38

Figure 11. Modelled phase field (a) without rotation, (b) after a 45^o rotation, (c) without considering change of orientation angle after rotation; (d) superimposed solid-liquid boundaries corresponding to grains in (a) and (b) [50] 39

Figure 12. Schematic of phase field (ϕ) and angle (θ) profiles across a bicrystal, according to the phase field model by Warren et al. [52] 41

Figure 13. KAM (kernel average misorientation) vs. distance from grain boundary obtained from scans with spatial resolutions of 2.5, 1, 0.5, and 0.2 μm [54] 42

Figure 14. (a) Bar chart of the misorientation angles perpendicular and parallel to grain boundaries; (b)-(c) perpendicular and parallel plots of misorientation vs. distance to grain boundary [54] 42

Figure 15. Schematics showing three levels of grid refinement, with increasingly finer grids at the interface region [61] 44

Figure 16. Mesh for coupling the lattice Boltzmann model (solid line) and the finite volume model (dashed line) [55] 50

Figure 17. Viscosity vs time graph while step changing the shear rate under isothermal conditions, from Modigell et al. [81] 55

Figure 18. Apparent viscosity of Al-6.5 wt.% Si alloy calculated as a function of effective solid fraction, compared with experimental data at various shear rates [82] 55

Figure 19. Framework of the multiscale model for TRC 56

Figure 20. Set up of the macroscale TRC model in ABAQUS 58

Figure 21. The temperature measured along the centreline of the strip, taken at different simulation times. The model is of pure Al TRC, with a casting speed of 2 m/min and without melt superheating. 61

Figure 22. The centreline exit temperature measured as a function of time, for models with different mesh sizes in the strip. The model is of pure Al TRC, with a casting speed of 2 m/min and without melt superheating. 62

Figure 23. Plot of the temperature profile from the macroscale model (mesh), and the temperature profile generated from the fitted parameters (dots) 72

Figure 24. Contour plot of the temperature profiles from the macroscale model and from the fitted model 72

Figure 25. Air gap between the roll and the strip due to imperfect contact affects heat transfer between strip and roll 75

Figure 26. Effect of gap conductance on the centreline exit temperature of the strip in pure Al TRC 76

Figure 27. Effect of gap conductance on solidus position in pure Al TRC 77

Figure 28. Strip temperature distributions of Al TRC at different casting speeds 78

Figure 29. Centreline and surface temperatures obtained at the exit vs casting speed 79

Figure 30. Temperature of a fixed point at the centreline of strip produced at different rolling speeds. Dashed lines indicate the time when the chosen point leaves the rolls. 79

Figure 31. Strip temperature distribution of Al at different roll temperatures, with a casting speed of 60 m/min 80

Figure 32. (a) Schematics for the quasi-1D solidification model for TRC. Only one roll and half the metal strip are shown as the system is symmetrical about the centreline of the strip; (b) Assumed relation between temperature (T) and distance from roll surface (x) for Stefan condition. Tm = melt temperature, and TR = roll surface temperature. 81

Figure 33. Theoretical solidus position vs roll temperature at different casting speeds 83

Figure 34. Enlarged graph of theoretical solidus position vs roll temperature, showing only slight decrease in solidus position from bite as roll temperature changes significantly 83

Figure 35. Schematics for calculating the theoretical upper bound casting speed 84

Figure 36. Theoretical upper bound casting speed vs strip thickness, for pure Al and Mg 85

Figure 37. Set up of the modified macroscale model, with an additional horizontal segment placed just above the strip, representing the effects of air cooling after the strip exits the rolls 86

Figure 38 Normalised viscosity against shear rate for different values of Bn and λ 90

Figure 39 Streamwise velocity distributions of 2D channel flows with different values of Bn and λ. The vertical line indicates where velocity profiles are measured. Inlet velocity is 0.5 m/s. 91

Figure 40. Velocity profiles measured in the middle of the 2D channel, when inlet velocity is 0.5 m/s 91

Figure 41 Streamwise velocity profiles of Bingham fluid with different λ values at Bn = 18.4, with inlet velocity of 0.5 m/s 92

Figure 42 Streamwise velocity profiles of Bingham fluid with different Bn values at λ = 0.6, with inlet velocity of 0.5 m/s 93

Figure 43 Velocity profiles for 2D channel flow with a doubled channel width (domain size is 202 × 602), with different values of Bn and λ, with inlet velocity of 0.5 m/s 94

Figure 44. Velocity profiles measured in the middle of the 2D channel, with inlet velocity of 0.05 m/s 95

Figure 45. Concentration and velocity distributions of a floating dendrite in fluid flow from left to right of the domain, with a normalised fluid velocity of 0.005 (left) and 0.01 (right), captured after 10000 timesteps 96

Figure 46. Concentration and velocity distributions of a floating dendrite in fluid flow from left to right of the domain, with a normalised fluid velocity of 0.01, with the nuclei starting in the middle of the channel (left) and near the wall (right), captured after 10000 timesteps 97

Figure 47. Concentration and velocity distributions of a pinned dendrite in fluid flow from left to right of the domain, with a normalised fluid velocity of 0.005 (left) and 0.01 (right), captured after 10000 timesteps 98

Figure 48. Orientation and velocity distributions using different Bingham LB model parameters, after 1000 timesteps. Velocity is measured in m/s. 102

Figure 49. Orientation distribution with only roll surface nucleation 104

Figure 50. Orientation distribution with no roll surface nucleation 104

Figure 51. Experimental data of pure Al TRC, from P Thomas et al. [92] 105

Figure 52. Modelled solidus position vs time for pure Al TRC with a casting speed of 2 m/min 106

Figure 53. Experimental set up for Mg TRC 108

Figure 54. Comparison between modelled and experimentally obtained exit surface temperatures for pure Mg TRC 108

Figure 55. Schematics indicating cells used to generate the as-cast microstructure 113

1. Introduction

1.1. Background and motivation

Twin roll casting (TRC) is an energy efficient way of producing sheets of magnesium alloys [1]. The cooling rate in TRC is higher than in conventional ingot casting. Mg sheets produced by TRC also have a weaker basal texture compared to those produced by ingot casting [2], allowing some thickness reduction during hot rolling of the sheets. However, unfavourable microstructural features such as coarse columnar dendrite grains and centreline segregation, where fine equiaxed grains are present [3]. Therefore, the as-cast alloy strips need to be thicker than the required thickness and subsequent machining of the strips are needed to remove the chemical inhomogeneities and microstructural defects, making the process less energy efficient and more expensive.

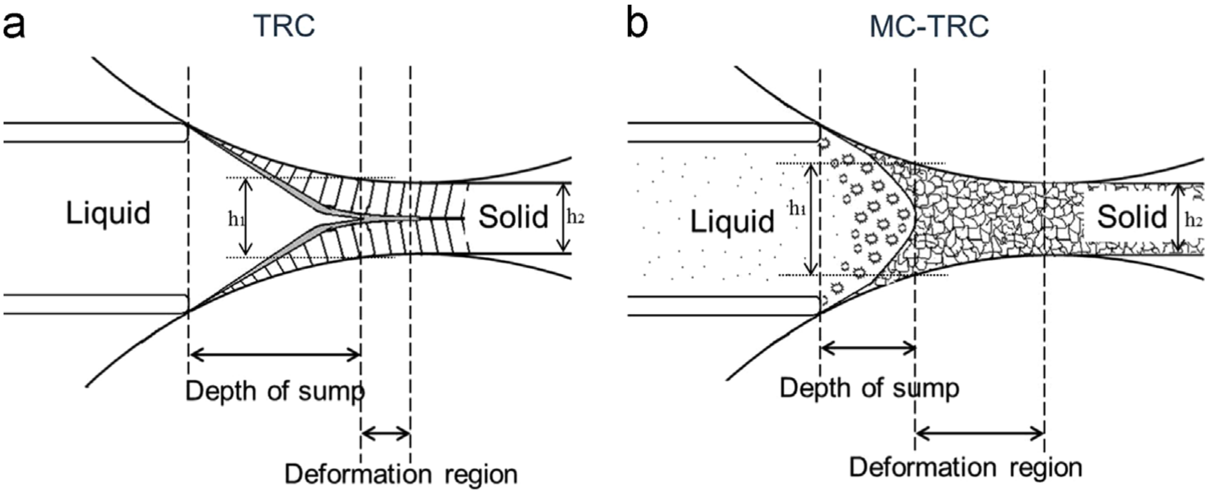

Figure 1. Schematics of the solidification mechanism for (a) TRC and (b) MCTRC samples [4]

Due to the high cooling rates at the surface, the as-cast TRC microstructure contains a thin layer of chill zone near the strip surface. Underneath the chill zone, columnar dendritic grains are formed in the opposite direction to the heat transfer direction, which is normal to the roll surface, and the columnar grains are inclined towards the nozzle entry as the rolls rotate [3], as shown in Figure 1 (a). Due to the accumulation of solute atoms at the solidification front, equiaxed grains with a different composition to the bulk and significantly smaller grain sizes are formed at the centreline. Intergranular cracks can also form above the centreline due to contraction during cooling, which could affect further processing after solidification.

Huang et al. [5] showed that by melt conditioning (MC) before the TRC process, centreline segregation in the as-cast Mg alloy can be eliminated, and a refined and uniform microstructure can be formed in the as-cast strips. This technique is referred to as MCTRC, in which grain refinement occurs because of the fine oxide particles forming from oxide films in the melt and dispersing uniformly in the melt during the melt conditioning process [4]. The oxide particles act as nucleation sites and an equiaxed fine-grained microstructure is formed.

Overall, TRC with or without melt conditioning is a complex manufacturing process, with respect to the variety of the relevant physical phenomena, ranging from fluid flow and heat transfer to solidification and plastic deformation, hence positing a challenging yet interesting problem for process optimisation. Modelling attempts have been made to investigate the complex melt flow and solidification mechanisms during the TRC process, in order to avoid defect formation in the casting strips and understand the influences of different casting parameters. Previous simulations of twin roll casting investigated the effects on casting parameters, like casting speed, casting temperature, shape and temperature of the die, setback, roll gap, cooling rate and roll material, on the temperature profile in the melt, as-cast microstructure, and stress and strain distributions. However, there have been few attempts to model the process on different length scales, from macroscopic level down to the microstructure level.

1.2. Research objectives

The present study aims to explore the problem further by considering a range of physical phenomena, including heat transfer, fluid flow, deformation, nucleation, and growth at different length scales. The modelling work starts with using finite element method (FEM) to calculate the thermal and mechanical fields. The calculated thermal fields are subsequently used for microstructure simulations. A major part of the work consists of developing a novel lattice-Boltzmann formulation to simulate Bingham plasticity, with is subsequently coupled to a phase-field model of phase transformation for simulation of TRC under realistic processing conditions as obtained from an experimentally informed FEM model.

1.3. Thesis outline

The structure of the thesis is as follows.

Chapter 1 states the problems with current TRC manufacturing techniques, and previous efforts in experiments and modelling of TRC in order to reduce defect formation.

Chapter 2 gives a review of previous macroscale TRC models, microscale solidification and fluid flow models.

Chapter 3 gives an outline of the proposed multiscale model for TRC.

Chapter 4 presents the set-up of the macroscale thermal-mechanical model.

Chapter 5 presents principles of the microscale model, including a phase field-Potts model for dendritic growth, and a Bingham lattice Boltzmann model for fluid flow.

Chapter 6 describes the coupling of phase field-Potts model and fluid flow model in the microscale model, and the coupling of the macroscale and microscale models.

Chapter 7 presents results from the macroscale model. Calibration and sensitivity tests of uncertain model parameters are shown. The effects of various casting conditions on the temperature profile of the strip are studied. A quasi-1D solidification model for TRC is used to calculate the theoretical upper bound casting speed for various alloys, to provide a guideline for model and experiments.

Chapter 8 presents results of 2D channel flow of Bingham fluid from the Bingham lattice Boltzmann model, and dendritic growth in a Phase field-Potts model under the influence of fluid flow. The effects of different model parameters on the velocity profile are investigated.

Chapter 9 presents the modelled microstructure evolution resulted from selected casting conditions and material parameters, according to the multiscale model. The effects of nuclei distribution and roll surface nucleation on the as-cast microstructure are investigated.

Chapter 10 shows experimental verifications of the macroscale and microscale models, and discusses sources of errors and limitations in the verification methods.

Chapter 11 discusses how findings from this research can impact current TRC manufacturing practices.

Chapter 12 shows the summary of the current study, and chapter 13 gives suggestions for future developments of the model and experimental verification methods.

2. Literature review

2.1. Previous work on twin roll casting

The effect of casting parameters, such as casting speed, pouring temperature and plastic deformation, on the microstructure and texture of the as-cast alloys and the material behaviour during subsequent processing has also been studied by Huang et al. [5]. It was found that a decreased casting speed or a reduced pouring temperature results in plastic deformation having a larger influence on microstructure evolution, due to the reduced mushy zone and decreased temperature at the exiting point [5]. The enhanced stored energy in alloy strips from plastic deformation also triggers dynamic recrystallization during the rolling process and results in a more fine-grained microstructure in further heat treatment processes. It is also shown that further homogenisation processes after the MCTRC process results in a stronger textured alloy, while the alloy homogenised in the MCTRC process has a weaker texture and better formability [5].

Chen et al. [6,7] used a micro mathematical model to simulate the solidification structure of Al alloy strips made by twin roll casting. Grain nucleation was modelled by Rappaz's nucleation model [8], and the KGT model was modified to model the constrained dendrite tip growth during solidification. Then, a columnar to equiaxed transition (CET) model was used to model internal nucleation in the dendrites. Solidification was modelled kinetically using the cellular automata model by Rappaz and Gandin [8]. The micro mathematical model predicted similar effect of pouring temperature on mean grain deviation and effect of interfacial heat transfer coefficient on mean grain size to those observed in experiments. However, there were errors in predicting the effect of pouring temperature on mean grain size, and the ability to predict grain regularity and phase information were not validated experimentally. The model simplified the nucleation step by neglecting melt oxidation, dendrite fragmentation, and effect of convection on nucleation, and centreline segregation was not considered in the model.

Zeng et al. [9] used computational fluid dynamics (CFD) modelling to simulate the temperature profile in a Mg alloy twin roll casting strip. A realisable k-ε turbulence model was used to model the turbulence in the melt pool. Solidification enthalpy was modelled with a temperature-dependent heat capacity, and the solidification process was modelled by considering a temperature-dependent viscosity and mushy zone formation. This model was used to study the influence of casting speed and gauge on melt flow and solidification field and showed good agreement between modelled and experimentally measured temperature distributions in the strips. Reversed flow was also observed by the model. The k-ε turbulence model was also used by Zhao et al. [10], who used a coupled analysis of temperature and flow with a linear solid fraction-temperature relation to model the effect of cooling rate and melt flow on the resulted microstructure and observed two symmetric vortexes in the cast-rolling zone, which affects grain refinement. Equiaxed dendrites with larger secondary dendrites spacing were observed in the centre of the microstructure modelled using this method.

Apart from CFD models, FEM methods were also used to model solidification in twin roll casting, by Hu [11] and He et al. [12]. FEM models were used to obtain acting forces and stress and strain rate profile within the strips. However, the influence of convection is not considered in the FEM models.

Hadadzadeh et al. [13] modelled the horizontal twin roll casting of Mg alloy strips using a 2D thermal-fluid-stress mathematical model and the mechanical behaviours were analysed using the commercial FEM code, ALSIM. The effects of set-back distance, heat-transfer coefficient, casting speed, and exit thickness on strip exit temperature, microstructure, stress, and strain, were investigated. Due to symmetry, only half of the melt pool is studied, which enforces symmetric solutions. However, previous modelling attempts were not backed up by reasonable experimental validations. For example, models by Chen et al. [6,7], Saitoh et al. [14] and Hwang et al. [15] show only partial coincidence between the modelled and experimental results. Previous models also did not consider the effects of pre-processing on TRC microstructure evolution, and the development of residual stress, grain regularity, and porosity during solidification. This project aims to understand the effects of cooling conditions, flow velocity and nuclei distribution on the as-cast microstructure in twin roll casting.

2.2. Fluid Flow Modelling

Fluid flow plays a central role in many solidification processes, including TRC. Inevitably, modelling of fluid flow should be considered in a multiphysics modelling of TRC. There are two main approaches to fluid flow modelling, which are explained in this section. However, the focus will be given to lattice Boltzmann method, which has been adopted for this study and further developed to include Bingham plasticity through a novel formulation.

2.2.1. Navier-Stokes Equations

Immiscible and incompressible multicomponent fluid flows can be described by the following Navier-Stokes equations.

$$\rho_i \left(\frac{\partial u_i}{\partial t} + u_i \cdot \nabla u_i \right) = -\nabla p_i + \nabla \cdot [\eta_i \, (u_i + u_i^T)] + SF_{sing} + \rho_i \, g \tag{1}$$

$$\nabla \cdot u_i = 0 \tag{2}$$

where the index $i = 1, 2$ denotes the two fluids, ρ_i is the density, u_i is the fluid velocity, p_i is the pressure field, η_i is the fluid viscosity, SF_{sing} is the singular surface tension force at the interfaces. and g is the gravitational acceleration. To model multiphase systems with variable densities, the Boussinesq approximation can be applied to eq. (1), which introduces a constant background density ρ_*, and adjusts the buoyancy force term to account for the differences between the actual density and the background density [16,17].

$$\rho_* \left(\frac{\partial u_i}{\partial t} + u_i \cdot \nabla u_i \right) = -\nabla p_i + \nabla \cdot [\eta_i \, (u_i + u_i^T)] + SF_{sing} + \rho_i(\phi) \, g \tag{3}$$

The Navier-Stokes equations can be solved by various finite element methods (FEM) and spectral methods. Karniadakis et al. used a high-order splitting scheme for the incompressible Navier-Stokes equations, which combines high accuracy in space and time with flexibility in geometry [16,18]. Kim and Lowengrub used a second-order projection method to decouple the solutions of the momentum equations and the continuity equation, to solve the incompressible Navier-Stokes equations in three-phase flows [19]. Mariano et al. proposed a pseudospectral method for solving the Navier-Stokes equations [20], in which the pressure term is eliminated by transforming to the Fourier space and considering incompressibility. Since the linear terms are cheaper to compute in the Fourier space, and the nonlinear terms are cheaper to compute in the physical space, each time step is solved by obtaining the derivatives in the Fourier space, and transforming the velocities and derivatives to the physical space, where the nonlinear terms are calculated and transformed back to the Fourier space. However, this method assumes periodic boundary conditions, and is unsuitable for fluid systems with variable densities and viscosities.

2.2.2. Lattice Boltzmann Method

The lattice Boltzmann (LB) method is a particle-based discrete method which predicts macroscopic properties. It originated from the lattice gas automata method, in which the space, time, and particle velocities are all discretised [21]. The lattice Boltzmann equation is derived from the Boltzmann equation [22], which is given by

$$\frac{\partial f}{\partial t} + \xi \cdot \nabla f = \Omega_f \tag{4}$$

where f is the single particle distribution function, ξ is the microscopic velocity, and Ω_f is the collision term. For a model with single relaxation time τ_f, the Bhatnagar–Gross–Krook (BGK) collision operator is used, which is expressed as

$$\Omega_f = -\frac{f - f^{eq}}{\tau_f} \tag{5}$$

where f^{eq} is the continuous Maxwell-Boltzmann distribution function. By discretising the velocity ξ into a set of lattice velocities in a DdQn lattice model, where d and n are the spatial dimension and the number of lattice velocities, the discrete Boltzmann-BGK equation can be written as

$$\frac{\partial f_i}{\partial t} + c_i \cdot \nabla f_i = -\frac{f_i - f_i^{eq}}{\tau_f} \tag{6}$$

where $\{c_i\}$ is the lattice velocities. In a two-dimensional nine-velocity (D2Q9) lattice model, the lattice velocities are given by

$$c_i = \begin{cases} (0,0), & i = 0 \\ c\,(\cos\left[(i-1)\frac{\pi}{2}\right], \sin\left[(i-1)\frac{\pi}{2}\right]), & i = 1,2,3,4 \\ \sqrt{2}\,c\,(\cos\left[(2i-9)\frac{\pi}{2}\right], \sin\left[(2i-9)\frac{\pi}{2}\right], & i = 5,6,7,8 \end{cases} \tag{7}$$

where $c = \delta x/\delta t$, δx is the lattice spacing, and the index i denotes the direction of the lattice velocity, as shown in Figure 2.

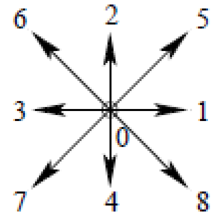

Figure 2. Lattice velocity indexing in the D2Q9 lattice [23]

The equilibrium particle distribution function f_i^{eq} is obtained as

$$f_i^{eq} = \rho w_i[1 + 3e_i \cdot u + \frac{9}{2}(e_i \cdot u)^2 - \frac{3}{2}u^2] \tag{8}$$

The weights w_i of a D2Q9 lattice are given by

$$w_i = \begin{cases} \frac{4}{9}, & i = 0 \\ \frac{1}{9}, & i = 1, 2, 3, 4 \\ \frac{1}{36}, & i = 5, 6, 7, 8 \end{cases} \tag{9}$$

By integrating eq. (6) over a time interval δt and assuming a constant collision term over the time interval, the standard lattice Boltzmann equation can be obtained.

$$f_i(x + c_i\delta t) - f_i(x, t) = -\frac{f_i - f_i^{eq}}{\tau} \tag{10}$$

where $\tau = \frac{\tau_f}{\delta t}$ is the non-dimensional relaxation time.

By discretising the domain so that $c_i\delta t$ is the distance between two neighbouring grid points, domain discretisation can be coupled with velocity discretisation, and the lattice Boltzmann equation can be considered as a collision process followed by a streaming process. The collision process is completely local,

$$f_i^*(x, t) = f_i(x, t) - \frac{f_i(x, t) - f_i^{eq}(x, t)}{\tau} \tag{11}$$

and the streaming process is completely linear.

$$f_i(x + c_i\delta t) = f_i^*(x, t) \tag{12}$$

Since most of the computations occur locally at the collision process, parallel computing can be easily applied to the lattice Boltzmann model [24].

Macroscopic equations can be derived from the lattice Boltzmann equations via the Chapman-Enskog expansion. The macroscopic variables, mass and momentum, can be deduced from the first two moments of the particle distribution functions, and are conserved in each time step.

$$\rho = \sum_i f_i \tag{13}$$

$$\rho u = \sum_i f_i \, C_i \tag{14}$$

According to Chen and Doolen [25], the following momentum equation can be derived from discrete LBE using Chapman-Enskog expansion.

$$\rho\left(\frac{\partial u_\alpha}{\partial t} + \frac{\partial (u_\alpha u_\beta)}{\partial x_\beta}\right) = -\frac{\partial P}{\partial x_\alpha} + \nu \frac{\partial}{\partial x_\beta}\left(\frac{\partial \rho u_\alpha}{\partial x_\beta} + \frac{\partial \rho u_\beta}{\partial x_\alpha}\right) \tag{15}$$

where the kinematic viscosity is $\nu = \frac{2\tau-1}{6}$, and the pressure is $P = \frac{\rho}{3}$.

2.2.2.1 Lattice Boltzmann models for immiscible two-phase flows

The Rothman-Keller-type model

The colour-gradient lattice Boltzmann model was proposed by Gunstensen et al. [26], who used red and blue particles to represent different fluid phases in multiphase flow simulations. Reis and Phillips [27] further developed the lattice Boltzmann model for immiscible two-phase flows, based on the Rothman-Keller model [26,28], in which the surface tension, density ratio and viscosity ratio of the phases can be controlled independently. The proposed model uses a D2Q9 lattice, and a lattice Boltzmann equation with a single relaxation parameter for each phase. A single-particle distribution function is defined for each fluid phase at the nodes, and the total particle distribution at node $\boldsymbol{x}$ and time t is expressed as

$$f_i(\boldsymbol{x}, t) = f_i^r(\boldsymbol{x}, t) + f_i^b(\boldsymbol{x}, t) \tag{16}$$

where r and b denotes the colour ('red' or 'blue') of the two phases. Assuming a time step of $\Delta t = 1$, the evolution equation of each phase is

$$f_i^k(\boldsymbol{x} + \boldsymbol{c}_i, t + 1) = f_i^k(\boldsymbol{x}, t) + \Omega_i^k(\boldsymbol{x}, t) \tag{17}$$

where $\boldsymbol{c_i}$ is the velocity vector, and Ω_i^k is the collision operator consisting of two processes, single-phase collision and perturbation, given by

$$\Omega_i^k = (\Omega_i^k)^{(1)} + (\Omega_i^k)^{(2)} \tag{18}$$

$(\Omega_i^k)^{(1)}$ is a single-phase collision operator representing relaxation to a local equilibrium state, and a standard BGK operator is used.

$$(\Omega_i^k)^{(1)} = -\omega_k(f_i^k - f_i^{k(e)}) \tag{19}$$

where ω_k is the relaxation parameter of phase k, which is a function of the fluid kinematic viscosity v_k.

$$\omega_k = 1/(3\, v_k + 0.5) \tag{20}$$

In order to account for the difference in viscosity between the two phases and ensure a smooth change in viscosity across the interface, an interpolation is used to obtain the relaxation parameter at the interface [28]. The colour field parameter ψ is defined as

$$\psi = \frac{\rho_r - \rho_b}{\rho_r + \rho_b} \tag{21}$$

which controls the relaxation function ω

$$\omega = \begin{cases} \omega_k, & \psi > \delta \\ y_r(\psi), & \delta \geq \psi > 0 \\ y_b(\psi), & 0 \geq \psi \geq -\delta \\ \omega_b, & \psi < -\delta \end{cases} \tag{22}$$

where $y_r(\psi)$ and $y_b(\psi)$ are functions chosen so that ω and its derivatives are continuous, and $\delta \leq 1$ is a free parameter which affects the thickness and dynamics of the interface.

$f_i^{k(e)}$ is the equilibrium function of phase k defined as

$$f_i^{k(e)} = \rho_k(\phi_i^k + W_i[3\boldsymbol{c_i} \cdot \boldsymbol{u} + \frac{9}{2}(\boldsymbol{c_i} \cdot \boldsymbol{u})^2 - \frac{3}{2}(\boldsymbol{u})^2\,]) \tag{23}$$

where W_i is the weight of lattice defined in eq. (9), and ϕ_i^k is defined as

$$\phi_i^k = \begin{cases} \alpha_k, & i = 0 \\ (1-\alpha_k)/5\,, & i = 1,2,3,4 \\ (1-\alpha_k)/20\,, & i = 5,6,7,8 \end{cases} \tag{24}$$

Grunau et al. [28] introduced an assumption for the density ratio γ in order to obtain a stable interface, which is

$$\gamma = \frac{\rho_r}{\rho_b} = \frac{1-\alpha_b}{1-\alpha_r} \tag{25}$$

The pressure of phase k is expressed as

$$p^k = \frac{3\,\rho_k\,(1-\alpha_k)}{5} = \rho_k\,(c_s^k)^2 \tag{26}$$

where c_s^k is the sound of speed in phase k, controlled by parameter α_k, which affects the hydrodynamic pressure at interfaces. In the case where $\rho_r \geq \rho_b$, the condition $\alpha_b \leq 1$ must be achieved in order to avoid negative pressures, and the following constraint can be deduced.

$$\frac{\rho_r - \rho_b}{\rho_r} < \alpha_r < 1 \tag{27}$$

The perturbation operator $(\Omega_i^k)^{(2)}$ is a function of the colour gradient F and defined as

$$(\Omega_i^k)^{(2)} = \frac{A_k}{2}\,|F|\,[W_i \frac{(F\cdot c_i)^2}{|F|^2} - B_i] \tag{28}$$

where A_k is a free parameter controlling surface tension, and B_i is given by

$$B_i = \begin{cases} -\frac{4}{27}, & i = 0 \\ \frac{2}{27}, & i = 1,2,3,4 \\ \frac{5}{108}, & i = 5,6,7,8 \end{cases} \tag{29}$$

The colour gradient defined in terms of the colour difference is expressed as

$$F(\boldsymbol{x}) = \sum_{i=1}^{8} \boldsymbol{c_i}\,[\rho_r\,(\boldsymbol{x}+\boldsymbol{c_i}) - \rho_b(\boldsymbol{x}+\boldsymbol{c_i})] \tag{30}$$

As the colour gradient is perpendicular to the interface between the two colours, the perturbation operator serves to redistribute the single-particle distribution at node $\boldsymbol{x}$, by adding to the particle distribution moving along the normal of the interface, and removing particle distributions moving parallel to the interface. As the colour densities are not conserved in this process, a recolouring step is required promote phase segregation at the interface.

Recolouring schemes

In the recolouring algorithm proposed b Gunstensen et al. [26], diffusion of colour at the interface is minimised by maximising the work done against the colour gradient $\boldsymbol{W}$, which means forcing the flux of colour at the interface to align with the colour gradient.

$$\boldsymbol{W} = \boldsymbol{K} \cdot \boldsymbol{F} \tag{31}$$

The colour flux vector $\boldsymbol{K}(\boldsymbol{x})$ is given by

$$\boldsymbol{K}(\boldsymbol{x}) = \sum_{i=1}^{8} \boldsymbol{c_i} \left(f_i^r - f_i^b\right) \tag{32}$$

The recolouring process is subjected to the following constraints of mass and total momentum conservation.

$$f_i^{r\prime\prime} + f_i^{b\prime\prime} = f_i^{\prime\prime} \tag{33}$$

$$\sum_i f_i^{r\prime\prime} = \rho_r \tag{34}$$

where the double prime denotes post perturbation quantities. The function of $\boldsymbol{W}$ vs. the particle distribution function of fluid k after perturbation yields no turning points, which means that the Lagrangian multiplier technique cannot be applied for the optimisation [27].

The optimisation algorithm based on eq. (31) leads to a maximum separation of the two colours, but generates spurious currents in the interface region [26]. In order to minimise velocity fluctuations at the interface, Tölke et al. [29] proposed a modified recolouring algorithm, which does not generate velocity fluctuations at a plain interface. The modified algorithm compares the particle distribution functions of both colours in antiparallel pairs of velocity vectors, and for each pair of velocity vectors, finds the minimum particle distribution between the two velocities and colours, which is resolved along the interface normal. The resolved particle distribution is the amount of red particles being moved along the colour gradient, and the amount of blue particles being moved in the opposite direction. The recolouring algorithm by Tölke et al. results in a weaker separation of colours, but has a higher stability, compared to the method by Gunstensen et al. [29].

In the lattice Boltzmann model proposed by Reis and Phillips [27], an optimisation method similar to that of Tölke et al. is used, in which the maximum number of red particles are sent along the colour gradient, and the blue particles are sent in the opposite direction, while subjecting to the mass conservation constraints. However, this recolouring model can result in lattice pinning [30], in which the interface gets pinned to the lattice when the flow at the interface is too weak to move many particles close to or on the interface.

Latva-Kokko and Rothman [30] suggested an alternative recolouring scheme to prevent lattice pinning, in which the recolouring process is defined as

$$(\Omega_i^r)^{(3)}(N_i^r) = \frac{\rho_r}{\rho} N_i + \beta \frac{\rho_r \, \rho_b}{\rho^2} \cos(\varphi_i) \; N_i^{(e)}(\rho, 0) \tag{35}$$

$$\left(\Omega_i^b\right)^{(3)}\left(N_i^b\right) = \frac{\rho_b}{\rho} N_i - \beta \frac{\rho_r \, \rho_b}{\rho^2} \cos(\varphi_i) \; N_i^{(e)}(\rho, 0) \tag{36}$$

where φ_i is the angle between the colour gradient and the velocity vector $\boldsymbol{c_i}$, and β is a parameter controlling interface thickness. As the parameter β decreases, the interface thickness increases. The condition $0 < \beta < 1$ must be reached to ensure positive particle distribution functions [30]. The single-particle distribution functions after perturbation are used as the input distribution functions N_i^k in eq. (35)-(36). $N_i^{(e)}(\rho, 0)$ is the colour-blind equilibrium function evaluated at the combined density and zero overall velocity. The above recolouring technique uses a constant value of α_r and α_b.

Leclaire et al. [31] proposed a colour gradient model that combines the Reis-Phillips model with the Latva-Kokko and Rothman recolouring scheme, in which the sound speed is considered a free parameter. Therefore the recolouring scheme is adapted to

$$(\Omega_i^r)^{(3)}(N_i^r) = \frac{\rho_r}{\rho} N_i + \beta \frac{\rho_r \, \rho_b}{\rho^2} \cos(\varphi_i) \sum_k N_i^{k\,(e)}(\rho_k, 0, \alpha_k) \tag{37}$$

$$\left(\Omega_i^b\right)^{(3)}\left(N_i^b\right) = \frac{\rho_b}{\rho} N_i - \beta \frac{\rho_r \, \rho_b}{\rho^2} \cos(\varphi_i) \sum_k N_i^{k\,(e)}(\rho_k, 0, \alpha_k) \tag{38}$$

where the colour-blind equilibrium function in the Latva-Kokko and Rothman recolouring scheme is replaced with the sum of the equilibrium distribution function of each fluid, evaluated at the respective value of α_k.

It is found that the recolouring scheme by Leclaire et al. has a smaller computational cost per time step, compared to the scheme by Latva-Kokko and Rothman [31]. The modified recolouring operator also leads to a stationary solution of complex fluid flow problems in fewer iterations than the recolouring operator used by Reis and Phillips. As shown in Figure 3, when convection is low, the average horizontal velocities of the two particles are the same as the local fluid flow velocity, but the particle gets pinned when the Reis-Phillips recolouring operator is used, whereas the initially pinned particle gets unpinned as time increases if the recolouring operator by Leclaire et al. is used. It is found that as $t \to \infty$, the relative error of the particle position tends to 0 in the model by Leclaire et al., compared to infinity in the Reis-Phillips model. Results from the modified recolouring operator also suggest that a lower speed of sound can diminish the lattice pinning problem. Lattice pinning can also be reduced by decreasing the β parameter, which will lead to increase in interface thickness.

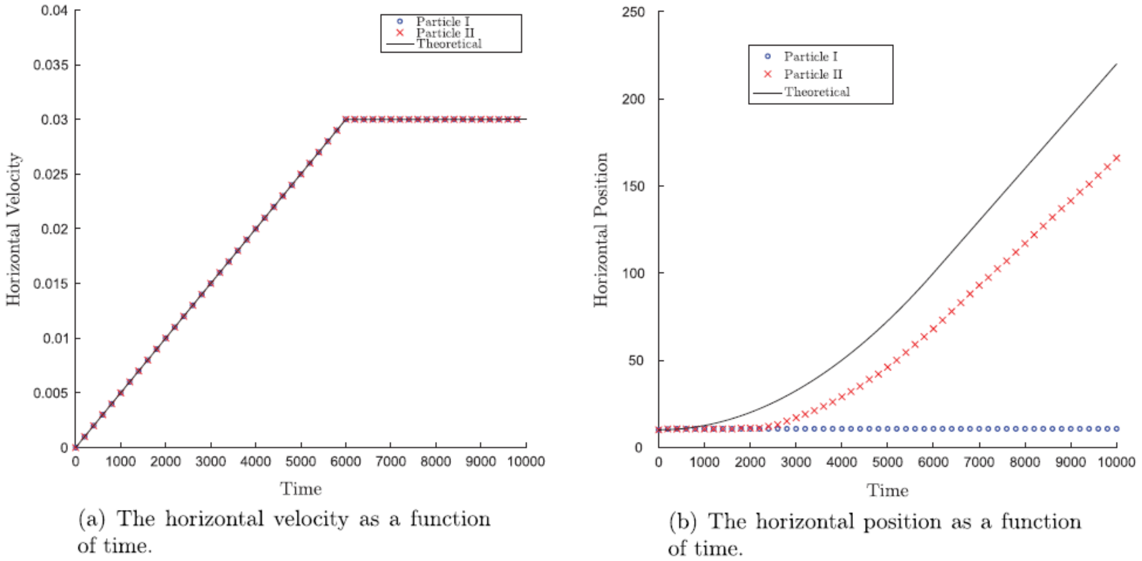

(a) The horizontal velocity as a function of time.

(b) The horizontal position as a function of time.

Figure 3. Study of the lattice pinning problem: comparison of results from recolouring operators by Reis and Phillips (Particle I) and by Leclaire et al. (Particle II), and the analytical solution [31]

In the 3D lattice Boltzmann simulations of binary flow through porous media by Tölke et al. [29], it is shown that the Rothman-Keller type LBGK model can be used to model immiscible binary fluid flow and obtain quantitative results. However, severe stability limitations are observed in the simulations, even at low Reynolds numbers. Moreover, when modelling the flow of two fluid components with different viscosities, the viscosity difference can lead to instabilities like viscous fingering [32]. Pooley et al. [32] demonstrated that strong spurious currents which drive the contact line out of equilibrium are observed when the lattice Boltzmann relaxation parameter is not held at unity. The problem cannot be avoided if the two fluids have different viscosities, which are controlled by the relaxation parameters.

It is suggested that stability can be improved by using multiple relaxation time (MRT) models [32]. In the MRT lattice Boltzmann model proposed by Pooley et al. [32], two particle distribution functions are defined at each point, the summations of which represent the fluid density and phase field parameter, respectively. This MRT model gives accurate simulations of binary fluid flow where the two fluids have different viscosities, which is reflected through the relaxation times in the collision operator. However, it is also shown that numerical instabilities still exist in MRT models, when large single-grid Reynolds numbers are used [33]. Therefore, the relative efficiency and suitability in solving complex fluid flow problems of LBGK models over other models is yet to be proven.

2.2.2.2 Forcing schemes in lattice Boltzmann models

Body forces can be applied in the lattice Boltzmann model via different forcing schemes. Buick and Greated [34] suggested different methods of implementing gravity in a lattice Boltzmann model. In the first method, the equilibrium distribution function is altered so that the corresponding Navier-Stokes equation incorporates the gravity term in an altered pressure tensor, which is suitable for systems with no density gradients. The second method introduces gravity by defining the equilibrium distribution function as a function of the equilibrium velocity, which is deduced from the lattice Boltzmann velocity and the change of momentum due to gravitational force. The third method adds an additional term to the collision function to represent the effect of gravity. The new collision term is defined as

$$\Omega_{\mathrm{i}} = -\frac{1}{\tau}\left[f_i - f_i^{(e)}\right] + 3W_i\, F_\alpha\, (c_i)_\alpha \tag{39}$$

where F is the gravitational force, and W_i is the weight of lattice defined in eq. (9). The fourth method, the composite model, is a combination of the previous two, in which the velocity expression in the equilibrium distribution function is altered, and an additional term is added to the collision operator.

The third method of introducing body forces is applied in the adapted unstructured lattice Boltzmann model by Fan et al. [35]. This method is preferred when the nonlinear term of the Navier-Stokes equation vanishes, due to its simplicity over the other methods. However, when the nonlinear term is present, it is found that the composite model gives a better estimate of the nonlinear term of the Navier-Stokes equation, compared to the second and the third method [34].

2.2.2.3 Boundary conditions in lattice Boltzmann models

Wall boundary conditions

Ubertini et al. [36] suggested three methods of imposing static and moving boundary conditions in 2D unstructured lattice Boltzmann models, which are the equilibrium method, the mirror method, and the covolume method. Among the three, the equilibrium method is the easiest to implement, but has the lowest physical accuracy. In this method, the particle distribution functions at every boundary point are set to the equilibrium particle distributions, which are evaluated at the boundary velocity.

The mirror method involves introducing ghost nodes at the boundary, which mirror the respective internal nodes next to the boundary nodes. The particle distribution functions at the mirror nodes are calculated based on a second-order interpolation from the boundary nodes and the corresponding internal nodes.

$$f(Mirror) = 2\,f(Boundary) - f(Internal) \tag{40}$$

After the particle distribution functions are defined at the mirror nodes, the boundary nodes can be treated the same as normal internal nodes in the streaming process. The mirror method supports boundary gradients but not generic boundaries.

The covolume method supports both boundary gradients and generic boundaries. Explicit evaluation of the edge fluxes are carried out via interpolation at the boundary edges. The edge flux at each boundary edge is set to the average of the particle distribution functions of two neighbouring nodes on the boundary edge. This method gives the highest physical accuracy but requires more difficult implementation.

Open boundary conditions

For the inlet boundary, Ladd [37] suggested a modification of the simple bounce-back boundary condition, in which a velocity profile is imposed at the inlet by adding a correction term to the particle distribution function. However, using the same treatment at the outlet will cause unbounded increase of total mass in the system, due to unbalanced mass fluxes in and out of the domain. To solve this problem, Nash et al. [38] constructed phantom sites beyond the boundary at the outlet, and imposed mixed Dirichlet-Neumann boundary conditions, including a target pressure, zero resolved velocity along the outlet boundary, and zero velocity gradient along the outlet normal. The particle distribution functions of the boundary nodes after streaming are deduced from the phantom sites. However, problems of this boundary treatment arise from the extrapolation of macroscopic velocity at the phantom sites. Finite difference approximations of the velocity gradient are used in the model [38], the complexity of which increases if higher-order differences are used.

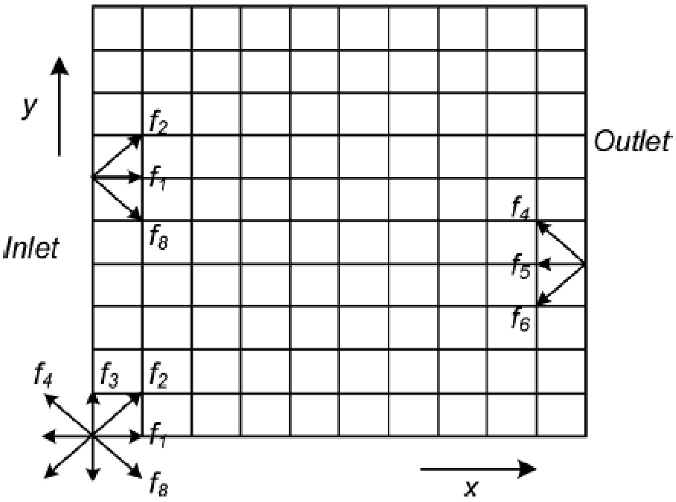

Figure 4. Schematics of lattice nodes at inlet and outlet regions [39]

For inlet and outlet sections where there is a constant discharge, a treatment is proposed by Liu et al. [39]. As shown in Figure 4, for the inlet boundary, the particle distribution functions along directions 1, 2, and 8 are undefined after the streaming process. A constant discharge is assumed at the inlet boundary, and zero-gradient macroscopic velocity and density are assigned to the inlet nodes. A compensation term is added to the expression of local flux at the inlet.

$$c\,(f_1 + f_2 + f_8) - c\,(f_4 + f_5 + f_6)\ = \rho u + \frac{Q_{in} - Q_c}{b} \tag{41}$$

where Q_{in} is the defined discharge at inlet, Q_c is the discharge obtained from the assigned macroscopic velocity and density ρ at the inlet nodes, u is the assigned inlet velocity along the x-axis, and b is the width of the inlet. Based on mass and momentum conservation, the following two equations can be obtained.

$$\sum_{i=0}^{8} f_i = \rho \tag{42}$$

$$c\,(f_2 + f_4) - c\,(f_6 + f_8\,) + c\,f_3 - c\,f_7 = \rho v \tag{43}$$

where v is the assigned inlet velocity along the y-axis. The missing particle distribution functions f_1, f_2, and f_8 after streaming can be obtained by solving eq. (41)-(43).

The corner node in Figure 4 requires a special treatment, as the particle distribution functions along five directions are unknown. Zou and He [40] suggested the use of the bounce-back rule for the non-equilibrium part of the distribution function normal to the inlet, eliminating two unknowns. The velocity condition at the wall is also taken into account, along with mass and momentum conservation, to solve for the missing particle distribution functions. As shown in Figure 5, by comparing the resulted discharge at the inlet and outlet, modelled with specified macroscopic velocity at the boundary corresponding to the constant discharge (termed 'general treatment'), and with the treatment proposed by Liu et al., it is found that the proposed treatment gives a more accurate and stable estimation of the flow features at the boundaries.

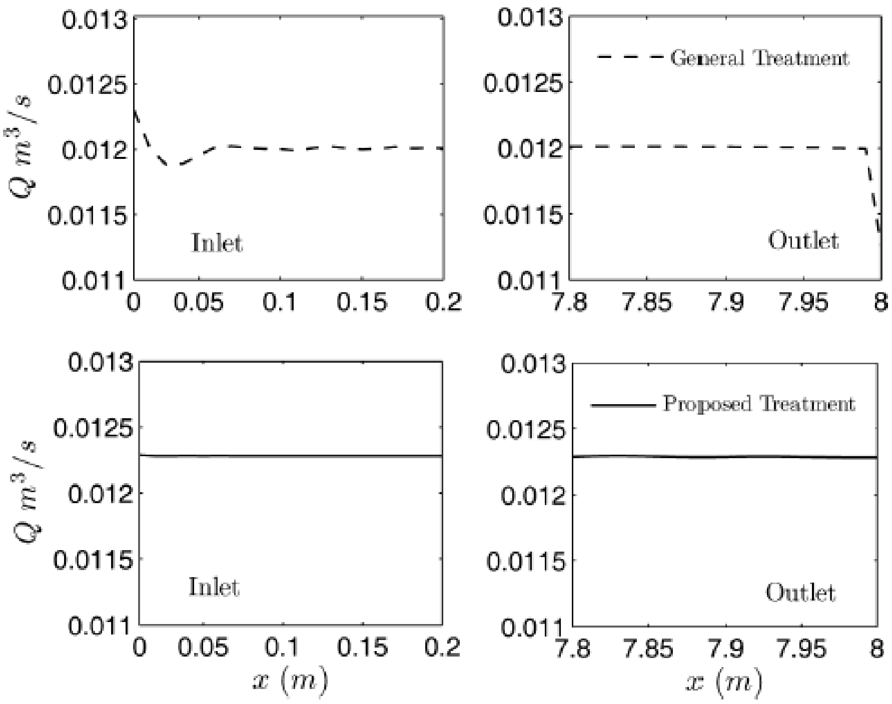

Figure 5. Comparison of discharge Q at the inlet and outlet of a straight channel [39]

2.2.2.4 Lattice Boltzmann models for unstructured grids

Lattice Boltzmann models are often implemented on regular grids, which allows coupling of the domain discretisation and the velocity discretisation, as the characteristic velocity directions are aligned with the spatial grid. However, the coupled discretisation is less useful when modelling fluid flows with complex boundary geometries.

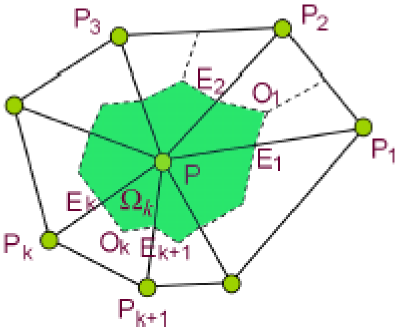

Figure 6. Schematic showing the 1-ring neighbourhood of points P_k around a grid point P. The green regions represent the finite volumes defined around point P [35]

Finite volume schemes have been developed by Ubertini et al. [36,41] and Rossi et al. [42]. In the unstructured scheme by Ubertini et al. [36], a finite volume is defined for each vertex, as shown in Figure 6. At each grid point, the collision and streaming operators are altered to represent the streaming and collisional fluxes of particle distribution functions coming from the corresponding finite volume at that grid point. The Unstructured Lattice Boltzmann Equation (ULBE) is expressed as

$$\begin{aligned} f_i(P, t+dt) = \ & f_i(P,t) + dt \sum_{k=0}^{K} S_{ik}\, f_i\,(P_k, t) \\ & - \frac{dt}{\tau} \sum_{k=0}^{K} C_{ik}\, [f_i(P_k, t) - f_i^{eq}\,(P_k, t)] \end{aligned} \tag{44}$$

where the index $k = 0$ represent the grid point P, and $k > 0$ represents the neighbouring grid points. The streaming matrix S_{ik} is defined as

$$S_{i0} = 0, S_{ik} = c_i \cdot \frac{N_k}{V_P}, k = 1, 2, \dots, K \tag{45}$$

The collision matrix $C_{ik} = C_k\ \delta_{ik}$, where δ_{ik} is the Kronecker delta function, is obtained by

$$C_0 = \frac{1}{3}, C_k\ = \frac{V_{k-1} + V_k}{3V_p}, k = 1, 2, \dots, K \tag{46}$$

where V_k is the area of Ω_k, and V_P is the area of $\Omega = \cup_k\ \Omega_k \cdot N_k$. N_k is a vector defined by

$$N_k = [\frac{5}{12}\,(A_{k-1}^{+} + A_k^{-})\ + \frac{2}{12}\,(A_{k-1}^{-}\ + A_k^{+}\ )], k = 1, 2, \dots, K \tag{47}$$

where $A_k^{\mp}$ are the vectors perpendicular to the lines $E_k O_k$ and $O_k E_{k+1}$, each with a magnitude equal to the length of the corresponding line.

The standard ULBE scheme has a stability constraint of $\Delta t < 2\tau$, where τ is the single relaxation time in the BGK operator [41]. Li and Luo [43] proposed a finite volume multiple-relaxation-time lattice Boltzmann model, in which the collision term is treated implicitly, to enhance the stability and efficiency of the model. Ubertini et al. [44] suggested the ULBE with memory scheme (ULBEM) to lift the stability constraint, in which a second-order strategy for the time finite differencing is used. The second order differential form of the semi-discrete Boltzmann equation in its implicit form is used, where the BGK collision operator is determined from the particle distribution functions from the current time step and the following time step. The new lattice Boltzmann equation can be assimilated to a continuous lattice Boltzmann equation with an additional second order derivative term, called the memory term. It is found that the ULBEM scheme is more stable and allows larger time-steps, compared to the standard ULBE scheme. Despite the higher computational cost per time-step which arises from extra memory and gradient calculation, the total simulation time of ULBEM is significantly reduced, due to the larger possible time-steps [44].

Fan et al. [35] adopted the 2D unstructured lattice Boltzmann model by Ubertini et al. to model flows in 3D curved surface meshes, and demonstrated its advantages over previous complex flow models due to the simple implementation, and easy incorporation of features such as boundary conditions, body forces and multiphase fluid interactions. However, Misztal et al. [45] suggested that although the unstructured lattice Boltzmann model can accurately model flows in complex domains using fewer elements than the regular grid based approaches, the latter remain competitive since they are more readily and massively parallelisable than the unstructured models.

2.2.3. Comparing Traditional Navier-Stokes Solvers with the Lattice Boltzmann Method

Tölke et al. mentioned that traditional Navier-Stokes solvers are not a priori superior to the lattice Boltzmann equation in modelling complex fluid flow problems [29]. Firstly, due to the explicit scheme and local computations, parallel computing can be easily implemented in the lattice Boltzmann model. Secondly, the lattice Boltzmann model also allows more straightforward application of complex boundary conditions, by using elementary mechanical rules like bounce-back and reflection to describe the interactions between particles and boundary walls. Thirdly, the streaming process of the lattice Boltzmann model is completely linear, whereas the Navier-Stokes equations contain nonlinear convective terms. Furthermore, the pressure field of incompressible flows is solved with an equation of state in the lattice Boltzmann model [25], instead of a Poisson equation in conventional Navier-Stokes solvers, which is more computationally expensive. For incompressible fluid flow simulations in a parallel implementation, it is shown that the lattice Boltzmann model can provide accurate solutions of the Navier-Stokes equations, and is of higher efficiency than the incompressible spectral solver [46]. However, features such as body-fitted coordinates and adaptive time-stepping are less amenable in the standard lattice Boltzmann model [47].

2.3. Modelling of Solidification

2.3.1. Phase Field Method

The phase field method is an efficient way of modelling microstructure evolution without tracking individual interfaces. An order parameter ϕ is used to indicate the phases present at each point in the system. For example, in a two-phase system, $\phi = 1$ and $\phi = 0$ represent the two pure phases, and the order parameter satisfies $0 < \phi < 1$ and changes continuously at the interface, as shown in Figure 7.

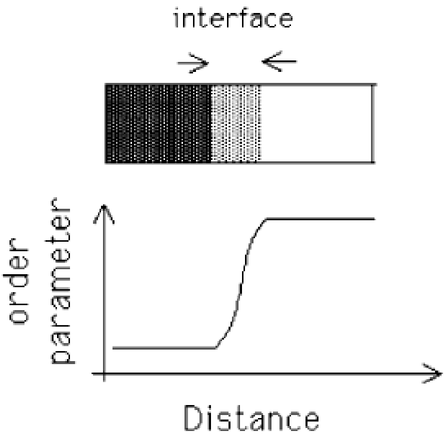

Figure 7. The change in order parameter at a diffuse interface [48]

The Ginzburg-Landau type free energy (F) consists of the free energy of formation of the individual phases as well as a contribution from the interface [48], which can be written as

$$F = \int d\boldsymbol{r}\,[f(\phi) + \frac{1}{2} W^2 \,|\nabla\phi|^2] \tag{48}$$

where f is the bulk free energy function which depends on the phase field parameter ϕ, and W is the diffuse thickness parameter. To obtain the equation of motion, it is required that

$$\frac{dF}{dt} = \int \frac{\delta F}{\delta\phi(r)} \frac{\partial\phi(r)}{\partial t}\, dr \leq 0 \tag{49}$$

A guess for the solution can be expressed as

$$\frac{\partial\phi(r)}{\partial t} = -M_\phi \frac{\delta F}{\delta\phi(r)} \tag{50}$$

where the mobility M_ϕ is a positive constant.

By substituting eq. (48) into eq. (50), the equation of motion for the phase field can be expressed as

$$\frac{\partial\phi(r)}{\partial t} = -M_{\phi}\left[\frac{\partial f(r)}{\partial\phi} - W^{2}\,\nabla^{2}\phi\right] \tag{51}$$

Phase field model for alloy solidification

In phase field models for alloy systems, solute diffusion is described by the Cahn-Hilliard equation.

$$\frac{\partial c}{\partial t} = \boldsymbol{\nabla}\cdot[M_{c}\,\boldsymbol{\nabla}(\frac{\partial g}{\partial c} - W^{2}\nabla^{2}c)] \tag{52}$$

where c is the solute concentration, W is the diffuse thickness parameter, g is the bulk free energy function, and M_c is the mobility constant.

The bulk free energy function g is described as

$$g\,(c) = \frac{1}{2}\,\mathrm{\alpha}^{2}\mathrm{c}^{2}(1-c)^{2} \tag{53}$$

where $c = 0$ and $c = 1$ represents compositions of the stable phases, and $\mathrm{\alpha}$ measures the barrier height in free energy between the two stable phases.

Assuming the mobility M_c and the diffuse thickness parameter W are independent of position, the Cahn-Hilliard equation can be written as

$$\frac{\partial c}{\partial t} = \mathrm{D}[M_{c}\,\boldsymbol{\nabla}(\nabla^{2}h - \lambda^{2}\nabla^{4}c)] \tag{54}$$

where D is the diffusion coefficient defined as $\mathrm{D} = M_{c}\mathrm{\alpha}^{2}$, λ is the interface thickness defined as $\lambda = W/\alpha$, and h is defined as

$$h = c(1-c)(1-2c) \tag{55}$$

With a known initial composition, the development of solute concentration with time can be obtained by solving eq. (54).

2.3.2. Modelling Dendritic Growth

Kobayashi proposed a phase field model for dendritic crystal growth [49], in which anisotropy is introduced into the interfacial energy term in the Ginzburg-Landau type free energy, expressed in eq. (48). The bulk free energy f is a double-well potential which can be defined as

$$f = \frac{1}{4}\,\phi^4 - \left(\frac{1}{2} - \frac{m}{3}\right)\phi^3 + \left(\frac{1}{4} - \frac{m}{2}\right)\phi^2 \tag{56}$$

where the parameter m satisfies $|m| < \frac{1}{2}$.

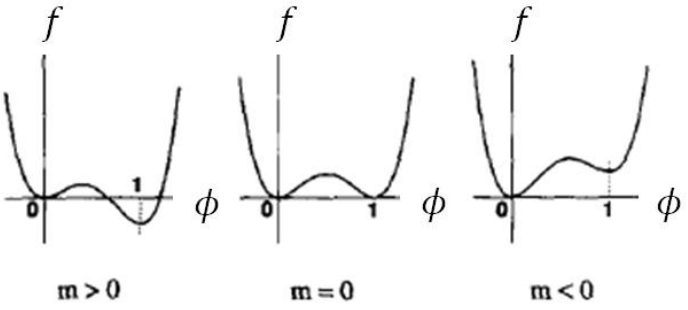

Figure 8. Double well potential $\boldsymbol{f}$ controlled by parameter $\boldsymbol{m}$ [49]

As shown in Figure 8, f has local minimums at $\phi = 0$ and 1, and the parameter m affects difference between the two local minimums, indicating the difference in chemical potential between the two phases. The parameter m is assumed to be a function of temperature T.

$$m(T) = \frac{\alpha}{\pi}\tan^{-1}[\gamma(T_e - T)] \tag{57}$$

where α satisfies $0 < \alpha < 1$, γ is a positive constant, and T_e is the equilibrium temperature.

Anisotropy is introduced by assuming dependence of interface thickness W on the direction of the outer normal vector at the interface ($-\boldsymbol{\nabla}\phi$). W is defined as

$$W = \bar{W}\,\sigma(\theta) \tag{58}$$

where $\bar{W}$ is a mean value of W, and anisotropy $\sigma(\theta)$ is specified as

$$\sigma(\theta) = 1 + \delta\cos[j(\psi - \theta)] \tag{59}$$

where δ is the strength of anisotropy, j is a mode number of anisotropy denoting crystal symmetry, θ is the grain orientation angle, and ψ is the inclination angle of the interface with respect to the x-axis, given by $\psi = \tan^{-1} \phi_y/\phi_x$.

Based on eq. (50), the evolution of phase field parameter with time is expressed as:

$$\tau\frac{\partial\phi}{\partial t} = -\nabla\cdot\left(|\nabla\phi|^2 \mathrm{W}\frac{\partial \mathrm{W}}{\partial \mathbf{v}}\right) + \nabla\cdot(W^2\nabla\phi) + \phi(1-\phi)(\phi - \frac{1}{2} + \mathrm{m}) \tag{60}$$

where $\boldsymbol{v} = -\nabla\phi$, and τ is the relaxation time. In two dimensional space, eq. (60) can be simplified as

$$\tau\frac{\partial\phi}{\partial t} = -\frac{\partial}{\partial \mathrm{x}}\left(WW'\frac{\partial\phi}{\partial \mathrm{y}}\right) + \frac{\partial}{\partial \mathrm{y}}\left(WW'\frac{\partial\phi}{\partial \mathrm{x}}\right) + \nabla\cdot(W^2\nabla\phi) + \phi(1-\phi)(\phi - \frac{1}{2} + \mathrm{m}) \tag{61}$$

where $W' = dW/d\theta$.

The evolution of temperature is expressed as

$$\frac{\partial T}{\partial t} = \nabla^2 T + K\frac{\partial\phi}{\partial t} \tag{62}$$

where T is non-dimensionalised so that the characteristic cooling temperature is 0, and the equilibrium temperature is 1, and K is the dimensionless latent heat.

Dendritic branching is induced by adding small noises on the interface. An additional term $a\chi$ is added to the function $m(T)$ at the interface, in which a is the noise amplitude, and χ is a random number sequence that follows a uniform distribution on the interval [-0.5, 0.5].

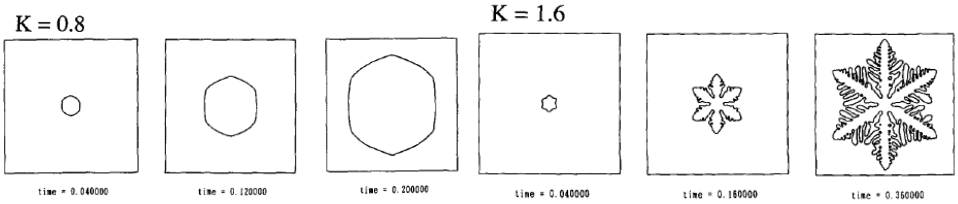

Figure 9. Crystal growth with different latent heat values [49]

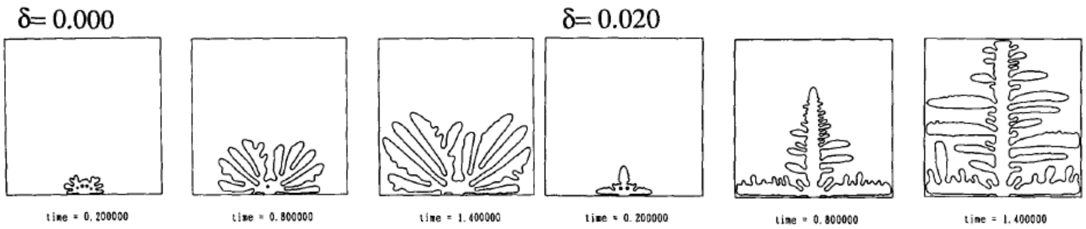

Figure 10. Crystal growth with different strengths of anisotropy [49]

This model can be used to model the growth of dendritic crystals without convection, under the effects of latent heat and anisotropy. As shown in Figure 9, as latent heat increases, the branching pattern becomes thinner. Figure 10 shows that the strength of anisotropy controls the branch structure, and the velocity of the principal branches increase with the strength of anisotropy.

2.3.3. Modelling Polycrystalline Solidification and Grain Rotation in the Presence of Melt Convection

The phase field model by Yamaguchi and Beckermann [50] combines the advective Cahn-Hilliard equation with the dendritic growth model by Kobayashi, to simulate the dendritic solidification of a single crystal in the presence of melt convection and solid deformation. The phase field evolution equation in two dimensions is given by

$$\begin{aligned}\tau_\phi(\theta)\left(\frac{\partial\phi}{\partial t}+\boldsymbol{v}\cdot\boldsymbol{\nabla}\phi\right) &= \boldsymbol{\nabla}\cdot\left(W^2(\theta)\boldsymbol{\nabla}\phi\right)-\frac{\partial f(\phi,T)}{\partial\phi}+\frac{\partial}{\partial \mathrm{x}}\left(|\nabla\phi|^2W(\theta)\frac{\partial W(\theta)}{\partial\phi_x}\right) \\ &+\frac{\partial}{\partial \mathrm{y}}\left(|\nabla\phi|^2W(\theta)\frac{\partial W(\theta)}{\partial\phi_y}\right)\end{aligned} \tag{63}$$

where relaxation time and diffuse interface thickness, $\tau_\phi(\theta)$ and $W^2(\theta)$, are functions of the grain orientation angle θ. The evolution of orientation angle due to advection and rotation is expressed as

$$\frac{\partial\theta}{\partial t}+\boldsymbol{v}\cdot\boldsymbol{\nabla}\theta=\boldsymbol{\nabla}\times\boldsymbol{v} \tag{64}$$

For an undeformed crystal where $\nabla\theta = 0$, the change in orientation angle due to rigid body rotation is obtained from the curl of the velocity field. As the orientation angle is only defined in solid phase, an extension scheme by Gibou et al. [51] is used to assign arbitrary orientation angles to the liquid, which are determined by the orientation of the closest solid. As shown in Figure 11, solving the phase field equation without considering evolution of orientation angle in the flow field results in an unrealistic swirling dendrite, in which the original orientation angle is constant at each location, whereas by accounting for the change of orientation angle in the flow field, the shape of the resulted dendrite can be kept after rotation.

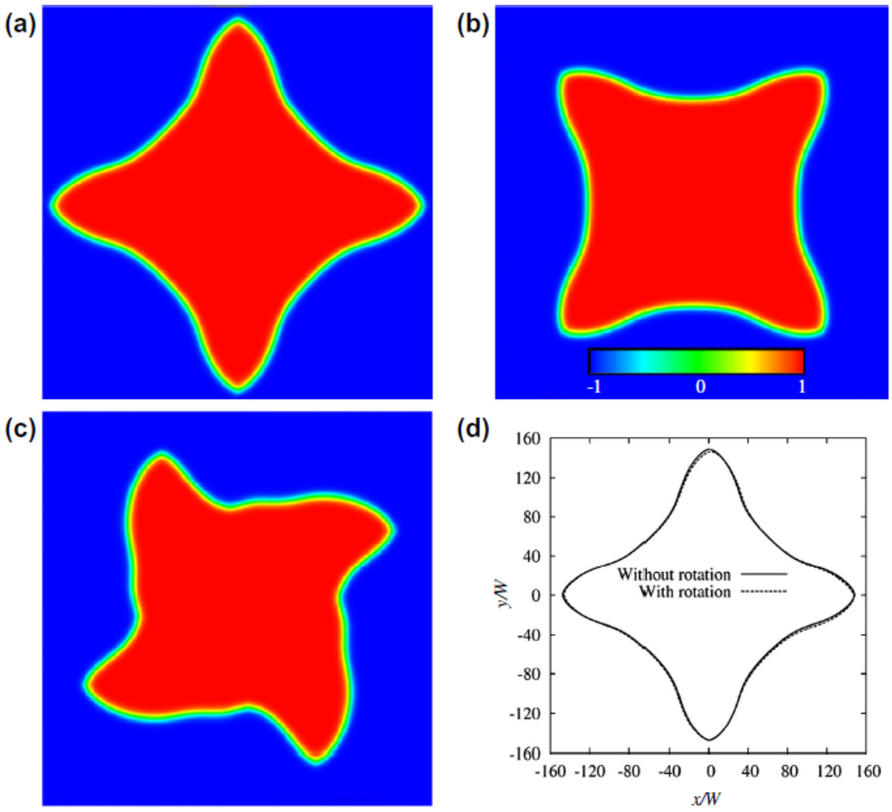

Figure 11. Modelled phase field (a) without rotation, (b) after a 45^{o} rotation, (c) without considering change of orientation angle after rotation; (d) superimposed solid-liquid boundaries corresponding to grains in (a) and (b) [50]

As the effect of grain boundary misorientation angle on the free energy density is not considered in eq. (60) and eq. (63), the models by Kobayashi and Yamaguchi et al. cannot be applied to model the formation of grain boundaries. Warren et al. suggested a phase field model for solidification of polycrystalline materials [52], in which the energy contribution of grain boundary misorientation angle is considered. Two additional terms involving orientation angle gradient are added to the free energy density expression.

$$F = \int dV\ [f(\phi,m)\ +\ \frac{1}{2}\ W^2\ |\nabla\phi|^2 + sg(\phi)|\nabla\theta| + \frac{e^2}{2}h(\phi)|\nabla\theta|^2] \tag{65}$$

where s and e represent the strength of coupling between ϕ and $\nabla\theta$, and $g(\phi)$ and $h(\phi)$ are monotonically increasing functions of ϕ, which fall to zero when ϕ becomes zero, and eliminate the effect of crystal orientation in the liquid phase. By modifying the free energy density, eq. (63) can be updated to model polycrystalline phase field evolution.

$$\begin{aligned} \tau_\phi(\theta)\left(\frac{\partial\phi}{\partial t} + \boldsymbol{v}\cdot\boldsymbol{\nabla}\phi\right) \\ &= \boldsymbol{\nabla}\cdot(W^2(\theta)\boldsymbol{\nabla}\phi) - \frac{\partial f(\phi,T)}{\partial\phi}\ +\ \frac{\partial}{\partial \mathrm{x}}\left(|\nabla\phi|^2 W(\theta)\frac{\partial W(\theta)}{\partial\phi_x}\right) \\ &+\ \frac{\partial}{\partial \mathrm{y}}\left(|\nabla\phi|^2 W(\theta)\frac{\partial W(\theta)}{\partial\phi_y}\right) -\ \frac{\partial g(\phi)}{\partial\phi}s|\nabla\theta| -\ \frac{\partial h(\phi)}{\partial\phi}\frac{e^2}{2}|\nabla\theta|^2 \end{aligned} \tag{66}$$

In the model by Warren et al. [52], the evolution of orientation angle without convection is assumed to be proportional to the rate of change of free energy density with respect to orientation angle.

$$P(\phi,\boldsymbol{\nabla}\theta)\tau_\theta\phi^2\frac{\partial\theta}{\partial t} = \ -\frac{\delta F}{\delta\theta} = \boldsymbol{\nabla}\cdot[\mathrm{h}(\phi)\ \mathrm{e}^2\boldsymbol{\nabla}\theta + g(\phi)s\frac{\boldsymbol{\nabla}\theta}{|\nabla\theta|}] \tag{67}$$

By combining eq. (64) and eq. (67), Yamaguchi et al. [53] proposed a modified evolution equation of the orientation angle, in order to model changes in grain orientation in the presence of convection and grain boundary, which is given by

$$P(\phi,\boldsymbol{\nabla}\theta)\tau_\theta\phi^2\ \left(\frac{\partial\theta}{\partial t} + \boldsymbol{v}\cdot\boldsymbol{\nabla}\theta\ -\ \boldsymbol{\nabla}\times\boldsymbol{v}\right) =\ \boldsymbol{\nabla}\cdot[\mathrm{h}(\phi)\ \mathrm{e}^2\boldsymbol{\nabla}\theta + g(\phi)s\frac{\boldsymbol{\nabla}\theta}{|\nabla\theta|}] \tag{68}$$

In the model by Yamaguchi et al. [53], the evolution of temperature field under convection is obtained from

$$\frac{\partial T}{\partial t} + \boldsymbol{v}\cdot\boldsymbol{\nabla}T\ =\ D\boldsymbol{\nabla}^2T + \frac{1}{2}\left(\frac{\partial\phi}{\partial t} +\ \boldsymbol{v}\cdot\boldsymbol{\nabla}\phi\right) \tag{69}$$

where D is the thermal diffusivity.

2.3.3.1. Problems with the Grain Orientation Evolution Model

In the phase field model proposed by Warren et al. [52], the gradient of grain orientation ($\nabla\theta$) is assumed to change gradually across the grain boundary, as shown in Figure 12, and the misorientation angle at grain boundary ($\Delta\theta$) is obtained by integrating $\nabla\theta$ across the grain boundary.

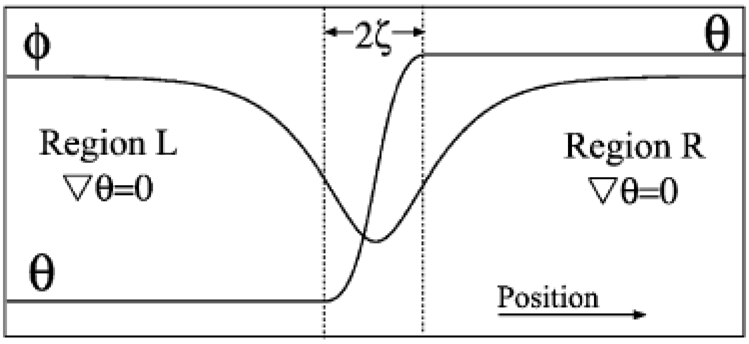

Figure 12. Schematic of phase field ($\boldsymbol{\phi}$) and angle ($\boldsymbol{\theta}$) profiles across a bicrystal, according to the phase field model by Warren et al. [52]

There are a few problems with modelling grain orientation as a phase field parameter. Firstly, the grain boundary is not a diffused interface. Therefore, there is not an established method of measuring the gradient of orientation. Subedi et al. showed that the orientation angle gradients measured at the grain boundaries of highly misoriented grains are resolution dependent [54], as shown in Figure 13. Figure 14 shows that the average misorientation angle measured perpendicular to grain boundaries is larger than that measured parallel to grain boundaries. It is also shown that the misorientation angles perpendicular to grain boundaries gradually decrease away from grain boundaries, whereas this pattern diminishes when misorientation angles are measured parallel to grain boundaries, which implies that the orientation gradients measured across the same set of grain boundaries will change in relation to the directions of the chosen coordinate axes of the system.

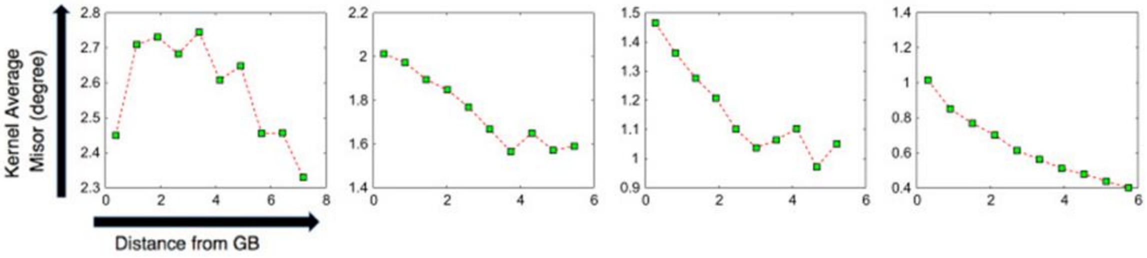

$2.5\ \mu m$ $1\ \mu m$ $0.5\ \mu m$ $0.2\ \mu m$

Figure 13. KAM (kernel average misorientation) vs. distance from grain boundary obtained from scans with spatial resolutions of 2.5, 1, 0.5, and 0.2 $\boldsymbol{\mu m}$ [54]

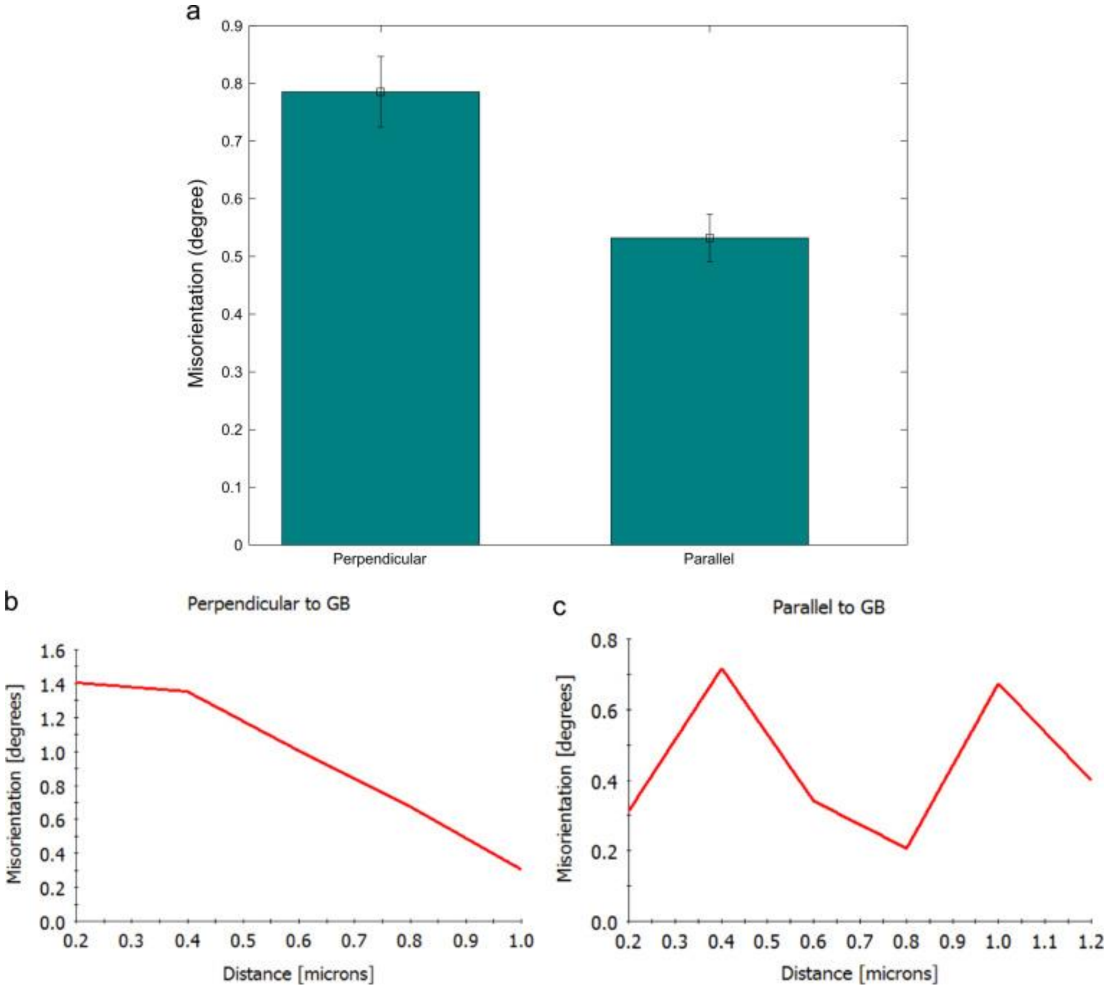

Figure 14. (a) Bar chart of the misorientation angles perpendicular and parallel to grain boundaries; (b)-(c) perpendicular and parallel plots of misorientation vs. distance to grain boundary [54]

Secondly, the gradient of orientation does not have a physical meaning, because grain orientation does not change continuously across the grain boundary in real microstructures. Thirdly, according to the free energy density in eq. (66), energy within the interface increases as the gradient of orientation increases. This means that when the system reaches minimum energy, the orientation gradient will tend to the minimum value, and there will be a continuous change in orientation within a diffused grain boundary, which is not physically true.

2.3.4. Approaches to Solving the Phase Field Equation

The phase field equation can be solved numerically via different space discretisation and time integration schemes. In the model proposed by Huang et al. [55], the phase field equation is solved via the finite volume scheme, and explicit 4th order Runge-Kutta method is employed for time stepping, which enhances the stability property. Finite difference and finite element methods have also been applied to discretise the phase field equation [56,57,57,58,58,59]. Ceniceros et al. [60] employed adaptive mesh refinement and a semi-implicit time discretisation to model the phase field evolution in 3D incompressible multi-phase flows. Adaptive mesh refinement is a space discretisation approach in which regions where greater accuracy is desired is locally refined. In the interface regions, a hierarchy of increasingly finer grids consisting of subdomains of smaller and smaller sizes are introduced, as shown in Figure 15. The grid is adapted dynamically based on the undivided phase field gradient. Cells with a phase field gradient greater than a critical value are tagged and grouped into rectangular patches, which are further refined into grids at the next level. This process is repeated until a maximum number of grid levels are established. A nonlinear full approximation storage (FAS) multigrid method is then used to solve the discrete system, in which the solution obtained from the coarse grid is compared to that obtained from the finer grid and a corrected approximation for the coarser grid is obtained and smoothed [61].

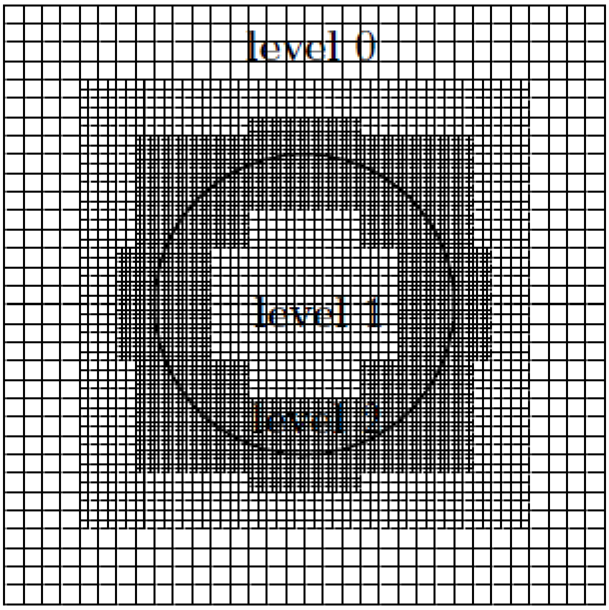

Figure 15. Schematics showing three levels of grid refinement, with increasingly finer grids at the interface region [61]

Adaptive time-stepping can also be applied as a time integration scheme [61,62][61,62](merged)[61], in which the solution after one large time step ($m\Delta t$) is calculated initially, and compared to the solution obtained after m smaller time steps, each of size Δt. The relative solution change is evaluated and compared to the prescribed error tolerance, in order to obtain the optimal step size Δt for the next time step. This time stepping scheme can improve the robustness and overall efficiency of the model. However, the computation cost per time step increases, due to the large number of steps required to obtain the reference solution at small time steps, and the slow convergence at large time steps.

2.3.4.1. Spectral Method

In addition to the finite element method and the finite difference method, the spectral method has also been used to solve the Cahn-Hilliard equation [63-67]. Zhu and Chen [68] developed a semi-implicit Fourier spectral method to obtain a solution for the Cahn-Hilliard equation with a variable mobility, which is concentration-dependent. According to Langer et al. [69] and Kitahara and Imada [70], the scaled Cahn-Hilliard equation with a variable mobility is expressed as

$$\frac{\partial C(r,t)}{\partial t} = \nabla \cdot (1 - aC^2)\, \nabla\, [-C + C^3 \; - \; \kappa\, \nabla^2 C] + \eta(r,t) \tag{70}$$

where $\eta(x,t)$ is the noise term given by a Gaussian random variable, $[-C + C^3 \; - \; \kappa\, \nabla^2 C]$ is the chemical potential, κ is a constant related to the interface thickness, $(1 - aC^2)$ is the scaled mobility, and a is a positive constant between 0 and 1. When $a = 0$, mobility is constant, which corresponds to bulk-diffusion-controlled dynamics. Meanwhile $a = 1$ describes an interface-diffusion-controlled dynamics. The value of a depends on the temperature of the system [68].

By transforming eq. (70) into the Fourier space, the following equation is obtained.

$$\frac{\partial \tilde{C}(k,t)}{\partial t} = ik \cdot \left\{ (1 - aC^2) \left[ik' \left(\{-C + C^3\}_{k'} + \kappa\, k'^2\, \tilde{C}(k',t) \right) \right]_r \right\}_k \tag{71}$$

where $[\,]_r$ represents inverse Fourier transform from the Fourier space to real space. The explicit Euler Fourier spectral solver poses a severe constraint on the time step. Therefore a semi-implicit treatment is used, in which the variable mobility is split into two terms, A and $(1 - aC^2) - A$. Additional terms $A\Delta t\, \kappa\, k^4\, \tilde{C}^{n+1}(k,t)$ and $A\Delta t\, \kappa\, k^4\, \tilde{C}^{n}(k,t)$ are added to the left-hand side and right-hand side of eq. (71) respectively to obtain the following equation.

$$\begin{aligned} &(1 + A\Delta t\, \kappa\, k^4)\, \tilde{C}^{n+1}(k,t) \\ &\qquad = (1 + A\Delta t\, \kappa\, k^4)\, \tilde{C}^{n}(k,t) + \Delta t\, ik \\ &\qquad \cdot \left\{ (1 - aC^2) \left[ik' \left(\{-C + C^3\}^n_{k'} + \kappa\, k'^2\, \tilde{C}^n(k',t) \right) \right]_r \right\}_k \end{aligned} \tag{72}$$

The time step constraint in the implicit solver can be lifted by choosing the constant A as $\frac{1}{2}[\max(1 - aC^2) + \min(1 - aC^2)]$. It is found that the semi-implicit scheme allows larger time steps to be used without compromising stability and accuracy.

2.3.4.2. Lattice Boltzmann Method

Zheng et al. [71] proposed a scheme of solving the advective Cahn-Hilliard equation via the lattice Boltzmann method. In the model, a D2Q5 lattice is used to save memory in the simulations, and a set of particle distribution functions for the order parameter are adopted. In this model, mobility is assumed to be constant among different phases.

$$g_i(x + c_i\delta t, t + \delta t) - g_i(x,t) \\ = (1-q)[g_i(x + c_i\delta t, t) - g_i(x,t)] - \frac{g_i(x,t) - g_i^{eq}(x,t)}{\tau} \tag{73}$$

where τ is the single relaxation time, and q is a constant. The above equation becomes the conventional lattice Boltzmann equation when q is 1. The equilibrium distribution function is given by

$$g_i^{eq} = A_i + B_i + C_i\,\phi\,c_{i\alpha}\,u_\alpha \tag{74}$$

where u is the macroscopic velocity, ϕ is the order parameter. The coefficients in eq. (74) are chosen as $A_0 = -3\Gamma\mu_\phi$, $A_i = \frac{1}{2}\Gamma\mu_\phi\ (i \neq 0)$, $B_0 = 1$, $B_i = 0\ (i \neq 0)$, and $C_i = \frac{1}{2q}$, where μ_ϕ is the chemical potential, and Γ controls the mobility. The order parameter is calculated from the first moment of the particle distribution functions.

$$\phi = \sum_i g_i \tag{75}$$

To apply the lattice Boltzmann method for systems with variable mobilities, Lee et al. [72] proposed a modified lattice Boltzmann model, in which the lattice Boltzmann equation corresponds to the following macroscopic equation.

$$\frac{\partial\phi}{\partial t} + \nabla\cdot(u\phi) = 0 \tag{76}$$

A source term is added to the right hand side of the lattice Boltzmann equation, which would solve for the derivative $\nabla\cdot(M\,\nabla\,\mu)$ in the macroscopic equation using values of M and μ obtained from the previous time step. The spatial derivative can be approximated via the finite difference method. The added source term can take the form of

$$S_i = W_i\,\delta t\,S \tag{77}$$

where $S = \nabla\cdot(M\,\nabla\,\mu)$.

In order to remove the assumption that the changes in M and μ are negligible in the chosen time step in the model by Lee et al. [72], Zheng et al. [73]proposed a treatment for the equilibrium distribution function, which enables the lattice Boltzmann equation to be recovered to the advective Cahn-Hilliard equation via Chapman-Enskog analysis. The modified equilibrium distribution function is expressed as

$$g_i^{eq} = W_i \left(H_i + \phi \left\{ \frac{c_i \cdot u}{RT} + \frac{1}{2} \left[\left(\frac{c_i \cdot u}{RT} \right)^2 - \frac{u^2}{RT} \right] \right\} \right) \tag{78}$$

where the coefficient H_i is given as

$$H_i = \begin{cases} \left[\phi - (1 - W_0) \left(\frac{\Gamma \mu}{RT} + \phi \right) \right] / W_0, & i = 0 \\ \frac{\Gamma \mu}{RT} + \phi, & i > 0 \end{cases} \tag{79}$$

The parameter Γ is related to the mobility M according to the following equation.

$$M = \delta t \, \Gamma \, \tau \tag{80}$$

2.3.5. Comparing Different Solvers of the Phase Field Equation

Compared to finite element methods, the advantages of a Fourier spectral method include easier pre-processing, which is achieved by allowing the direct input of voxelised data with no further meshing required, exponential convergence [67,74], which means that a significantly smaller number of grid points is required to achieve a prescribed accuracy of the solution, and faster computation [74], since the spectral method avoids the difficulty due to meshing, and is less computationally intensive than FEM. However, by applying the spectral method, the domain is subjected to periodic boundary conditions. Buffer zones [75] can be used to break the imposed periodicity assumption, but complexity arises when the spectral method is applied to irregular geometries. Meanwhile, the lattice Boltzmann model can be applied to unstructured grids according to the schemes proposed by Ubertini et al. [35].

In the lattice Boltzmann model, the space discretisation and time stepping schemes are less flexible, and adaptive mesh refinement and time stepping schemes with better stability properties, such as high-order Runge-Kutta schemes and semi-implicit schemes, cannot be applied. However, the limit on time step imposed by stability in an explicit scheme can be overcome by the reduction in computation costs due to parallelisation, which is easier to implement in the lattice Boltzmann model due to its explicit and local characteristics.

When phase-dependent mobility is introduced, two different treatments of the lattice Boltzmann equation have been suggested by Lee et al. [72] and Zheng et al. [73]. The model by Lee et al. is easier to implement, but introduces error by approximating $\nabla \cdot (M \, \nabla \, \mu)|_{(x + c_i \, \delta t, t + \delta t)}$ with the value of $\nabla \cdot (M \, \nabla \, \mu)|_{(x + c_i \, \delta t, t)}$. Meanwhile, the model by

Zheng et al. avoids this error by adjusting the equilibrium distribution function. However, in order to adopt the lattice Boltzmann method to solve the phase field equation for polycrystalline solidification, the lattice Boltzmann equation needs to be modified so that the corresponding macroscopic equation reflect contributions of anisotropic grain growth and grain boundary misorientation angle, as shown in eq. (66). The method by Zheng et al. involves investigating how each term in the equilibrium distribution function corresponds to terms in the macroscopic equation after the Chapman-Enskog analysis, and how the parameters relate to macroscopic properties, which are done through trial and error, as opposed to the approach by Lee et al., of adding a source term to the lattice Boltzmann equation that can be derived directly from terms in the macroscopic equation, which is more straightforward. Furthermore, another problem arises by introducing the grain orientation-dependent relaxation parameter in eq. (66), as the parameter Γ in eq. (80) and the relaxation parameter in the lattice Boltzmann equation need to be adjusted in every time step. Furthermore, boundary conditions of the order parameter and the chemical potential are more difficult to implement accurately in the lattice Boltzmann model, and require deduction of particle distribution functions from macroscopic properties by reversing the Chapman-Enskog analysis.

2.4. Coupling Fluid Flow with Phase Field Modelling

2.4.1. Free Energy Model

In the free energy model improved by Zheng et al. [71], the 2D Navier-Stokes equations and the advective Cahn-Hilliard equation are solved via two lattice Boltzmann equations. The first moments of the two sets of particle distribution functions used correspond to the density and the order parameter respectively. In the lattice Boltzmann equation for fluid flow modelling, a BGK collision operator is used. According to the model by Langaas and Yeomans [76], the difference in viscosity between the phases is represented by modifying the single relaxation parameter in the BGK collision operator to be a function of the order parameter in the phase field model, and the kinematic viscosities of the fluids. The following lattice Boltzmann equation is used for fluid flow modelling.

$$f_i(x + c_i\delta t, t + \delta t) - f_i(x,t) = -\frac{f_i - f_i^{eq}}{\tau_\rho} + S_i \tag{81}$$

where S_i is a source term which represents the body force in the Navier-Stokes equation, and the relaxation time τ_ρ is expressed as

$$\tau_\rho = \left(\nu_1^{\frac{\rho+\phi}{2\rho}} \nu_2^{\frac{\rho-\phi}{2\rho}} / c_s^2 \right) \delta t + 0.5 \tag{82}$$

Eq. (81) is solved in a D2Q9 lattice to update the particle distribution functions for the density (f_i), while the Cahn-Hilliard equation is solved in a D2Q5 lattice via the lattice Boltzmann method, to update the particle distribution functions for the order parameter (g_i), following eq. (78). In each time step, the macroscopic velocity field can be obtained from f_i and is used to calculate the equilibrium distribution function for g_i, subsequently the order parameter obtained from g_i is used to control the relaxation time of f_i in the next time step.

One advantage of the model by Zheng et al. [71] in the fluid flow aspect is the use of a single set of particle distribution functions to simulate multiphase fluid flow with different viscosities, compared to two sets of distribution functions of different colour particles with different relaxation parameters used in Rothman-Keller-type models, as shown in eq. (16). Furthermore, solving the lattice Boltzmann equation in the free energy model requires only the collision and streaming steps, whereas additional two-phase collision and recolouring steps are involved in the colour gradient model.

Huang et al. [77] compared the free energy model and the Rothman-Keller model in simulating multiphase flows in porous media without phase change. It is found that the free energy model satisfies the Galilean invariance principle, and has good mass conservation property. Furthermore, it is able to model multiphase flows with large viscosity ratio with accuracy comparable to that of the Rothman-Keller model. The number of time steps required for convergence and the computation time are also similar for the free energy model and the Rothman-Keller model.

2.4.2. Hybrid Lattice Boltzmann Finite Volume Method

Huang et al. [55] proposed a phase field-based hybrid lattice Boltzmann finite volume method to model droplet motion under electrowetting control. The lattice Boltzmann method is used to simulate the hydrodynamics of the fluid flow, while the interface dynamics is modelled by the Cahn-Hilliard equation via a finite volume method. Two different meshes are generated from the domain for fluid flow and phase field modelling, as shown in Figure 16. The boundary lattice Boltzmann nodes are half-lattice away from the wall, and the boundary of the finite volume mesh overlaps with the wall, which provides an easier way of implementing the bounce-back-by-link boundary condition in the lattice Boltzmann model, and the boundary conditions for phase field parameter and chemical potential in the phase field model.

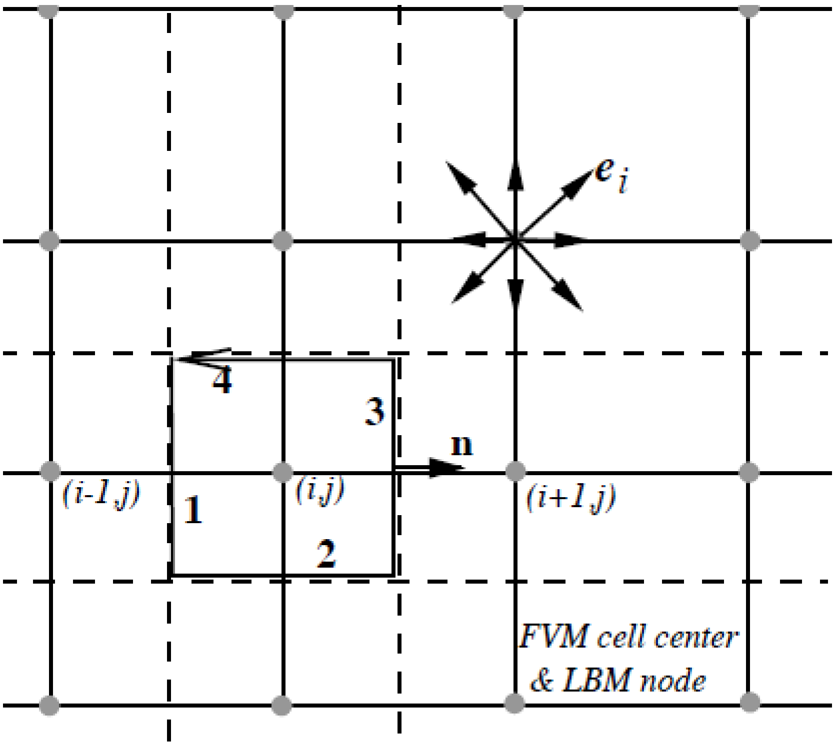

Figure 16. Mesh for coupling the lattice Boltzmann model (solid line) and the finite volume model (dashed line) [55]

In the finite volume mesh, local profiles of velocity, chemical potential, and phase field parameter along the centre line are reconstructed from local and neighbouring cell average values with 2nd order accuracy. For example, the local profile of phase field parameter is calculated from

$$\phi(x) = ax^2 + bx + c \tag{83}$$

where $a = \frac{1}{2}(\bar{\phi}_{i,j+1} + \bar{\phi}_{i,j-1} - 2\bar{\phi}_{i,j})$, $b = \frac{1}{2}(\bar{\phi}_{i,j+1} - \bar{\phi}_{i,j-1})$, and $c = \bar{\phi}_{i,j}$.

For time stepping, an explicit 4th order Runge-Kutta method is employed, in which velocity in the advective phase field equation is frozen as time marches from t_n to $t_n + \delta t$. The evolution of phase field can be obtained from

$$\bar{\phi}_{n+1} = \bar{\phi}_n + \frac{1}{6}(a_n + 2b_n + 2c_n + d_n) \tag{84}$$

where $a_n = \delta t \frac{d\bar{\phi}}{dt}(t_n, \bar{\phi}_n)$, $b_n = \delta t \frac{d\bar{\phi}}{dt}(t_n + \frac{1}{2}\delta t, \bar{\phi}_n + \frac{1}{2}a_n)$, $c_n = \delta t \frac{d\bar{\phi}}{dt}(t_n + \frac{1}{2}\delta t, \bar{\phi}_n + \frac{1}{2}b_n)$, and $d_n = \delta t \frac{d\bar{\phi}}{dt}(t_n + \delta t, \bar{\phi}_n + c_n)$.

Both the cell averaged phase field parameter and the chemical potential are updated in every step of the Runge-Kutta method, which makes the hybrid model more complex than the pure lattice Boltzmann model by Zheng et al. [71]. However, since solving the phase field equation consumes a relatively small portion of the overall computation effort, the efficiency of the model is not significantly affected by the increase in complexity, when compared with the pure lattice Boltzmann formulation [55]. Meanwhile, the hybrid model retains the advantage of computation speed for using the lattice Boltzmann method for the Navier-Stokes equations, compared to the pure finite volume formulation. Furthermore, a variable mobility is easier to implement in the finite volume model, and the boundary conditions for the phase field parameter and the chemical potential are easier to impose accurately, compared to the lattice Boltzmann model. The finite volume scheme also allows more flexible time stepping scheme for the phase field model.

2.4.3. Phase Field-Lattice Boltzmann Method for Modelling Dendritic Growth with Melt Convection

To model the motion and growth of a dendrite during solidification with melt convection, Rojas et al. [78] developed a phase field-lattice Boltzmann model in a uniform grid. In each time step, the phase field equation without convection is first solved using the finite difference method to model phase transformation, and the fluid flow of the liquid phase is modelled using the lattice Boltzmann method. In order to track the translational and rotational motion of the solid phase, an external forcing term is added to the lattice Boltzmann equation to describe the drag force at the liquid-solid interface.

$$f_i(x + c_i\delta t) = f_i(x,t) - \frac{f_i - f_i^{eq}}{\tau} + G_i(x,t)\,\delta t \tag{85}$$

The discrete forcing term G_i is given by

$$G_i = \rho\, W_i \left[3\,\frac{c_i - u}{c^2} + 9\,\frac{(c_i \cdot u)\, c_i}{c^4}\right] \cdot G \tag{86}$$

where G is the external force used to impose no-slip condition at the liquid-solid interface, which is modelled as a dissipative drag force.

$$G = \frac{2\,\rho \upsilon g}{W_0^2}\,\phi^2\,(u_s - u) \tag{87}$$

where υ is the kinematic viscosity, and u_s is the solid velocity, given by

$$u_s = u_T + \omega_s \times (x - X_s) \tag{88}$$

where u_T is the translational velocity of the solid, ω_s is the angular velocity, and X_s is the centre of mass of the solid.

The motion of the solid phase is described by the following equations.

$$M_s \frac{d\,u_T}{dt} = G_s \tag{89}$$

$$I_s \frac{d\,\omega_s}{dt} = T_s \tag{90}$$

where M_s is the mass of the solid, I_s is the moment of inertia, and G_s and T_s are the total force and torque acting on the solid, which are given as

$$G_s = -\sum_{x \in \Omega} G(x,t)\,\Delta V \tag{91}$$

$$T_s = -\sum_{x \in \Omega} (x - X_s) \times G(x,t)\,\Delta V \tag{92}$$

where ΔV is the cell volume, and Ω is the domain in the interface regions.

After the solid velocity is obtained, the location of the phase field is updated using the advection equation. In this model, the effects of gravity and other external forces are assumed to be negligible, but the forcing term in eq. (85) can be adjusted easily to include other external forces. Rojas et al. validated this model by simulating the growth and rotation of a single dendrite in melt flow. When multiple dendrites are involved, additional schemes are required to match the centre of mass of each dendrite before and after each fluid flow modelling step.

2.5. Previous models of rheological behaviour of semisolid metal slurries

Semisolid metal (SSM) slurries are formed during solidification, and consist of interacting solid particles suspended in liquid. Shearing of the slurries results in the formation of agglomerates. Under viscous forces, agglomerates can collide to form agglomerates of larger sizes, or break up into agglomerates of smaller sizes. A structural parameter is used to define the state of agglomeration, which can be influenced by flow properties such as shear rate, and affects the rheological properties of the slurry. Joly and Mehrabian describes the rheological behaviour of SSM slurries as showing shear rate dependency of steady state viscosity, time dependency of transient state viscosity, and viscosity evolution during continuous cooling [79].

SSM slurries exhibit time-dependent, thixotropic properties. In the thixotropic model proposed by Moore [80], the shear stress is a function of shear rate, and is related to a time-dependent structural parameter, which determines the structural influence on flow behaviour such as agglomeration. Shear stress is assumed to increase exponentially with the solid fraction. Viscosity η is calculated as

$$\eta = \frac{\tau}{\dot{\gamma}} = \left(\frac{\tau_0(f_s)}{\dot{\gamma}} + k^*(f_s)\dot{\gamma}^{m(f_s)-1}\right)\kappa \tag{93}$$

where $\dot{\gamma}$ is the shear rate, τ is the shear stress, and the yield stress τ_0, the consistency factor k^* and the exponent m are all dependent on the solid fraction f_s.

Changes in the structural parameter is dependent on the deformation history of the slurry. As shown in the modelled and experimental data in Figure 17, a sharp increase in viscosity is observed immediately after step increases of shear rates. Over time, the structural parameter approaches an equilibrium value according to the shear rate, and the steady state viscosity decreases as shear rate increases.

The time-dependency of the structural parameter can be described by the following kinetic differential equation [81].

$$\frac{D\kappa}{Dt} = c(\dot{\gamma})(\kappa_e(\dot{\gamma}) - \kappa) \tag{94}$$

where κ_e is the equilibrium structural parameter, and $c(\dot{\gamma})$ is the rate constant of approaching equilibrium, which has a negative correlation to the shear rate and is modelled as:

$$c(\dot{\gamma}) = a \cdot \exp\ (-b\,\dot{\gamma}) \tag{95}$$

Viscosity of the SSM slurry η is directly related to the viscosity of the liquid matrix η_0 and the effective solid volume fraction Φ_{eff}, as described in

$$\eta = \eta_0\left(1 - \Phi_{eff}\right)^{-5/2} \tag{96}$$

which is applicable for Φ_{eff} values where solid particles don't form a 3D network.

The equation above indicates that viscosity of the SSM slurry is not affected by shear rate, as shown in the modelled and experimental results in Figure 18. The SSM slurries exhibit Newtonian properties when the effective volume fraction is considered.

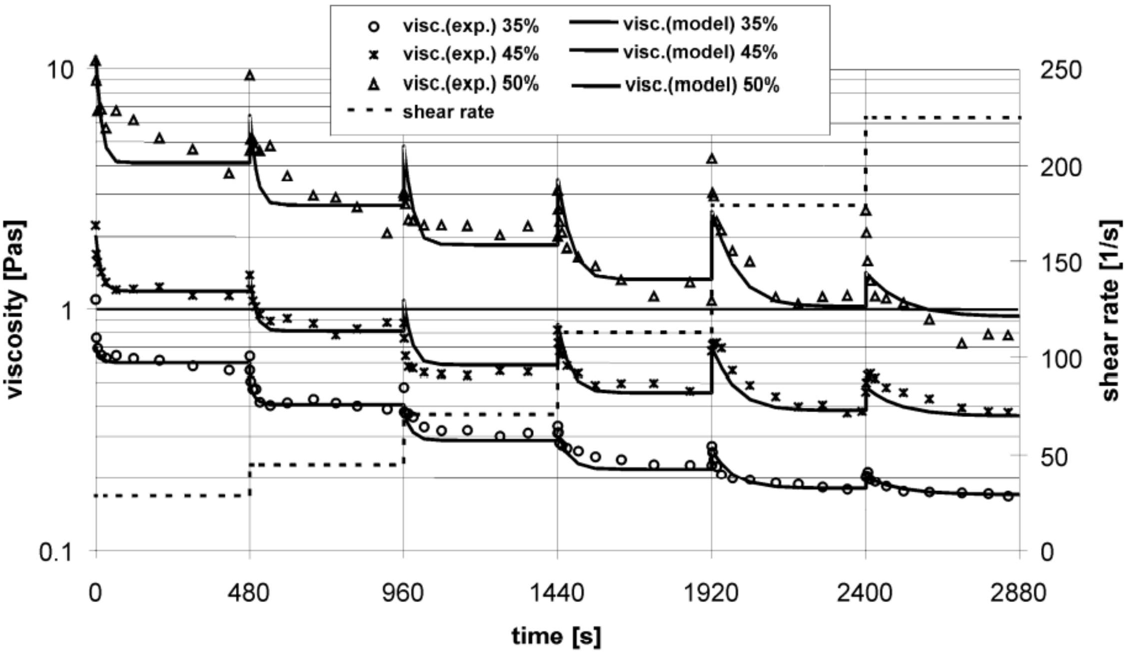

Figure 17. Viscosity vs time graph while step changing the shear rate under isothermal conditions, from Modigell et al. [81]

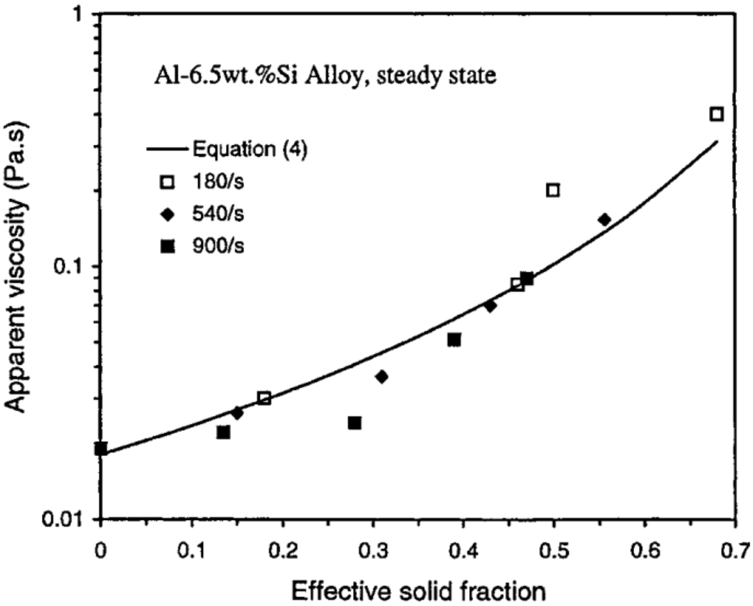

Figure 18. Apparent viscosity of Al-6.5 wt.% Si alloy calculated as a function of effective solid fraction, compared with experimental data at various shear rates [82]

3. Multiscale model

3.1. Multiscale model outline

The proposed multiscale model consists of a macroscale thermal-mechanical model, and a microscale model which combines a phase field model with fluid flow simulation. Casting parameters, such as melt temperature, roll temperature and casting speed, and material properties of the casted alloy are used as inputs for the macroscale model, which models the temperature profile of the metal strip and stress development during the process. The temperature distribution is used as thermal boundary conditions for the microscale model, which consists of a phase field model coupled with a fluid flow model, to study the effects of fluid flow on microstructure evolution during solidification. The as-cast microstructures generated from the microscale model can be used to provide feedback and aid the selection of casting conditions to obtain the desired microstructures and improve production efficiency.

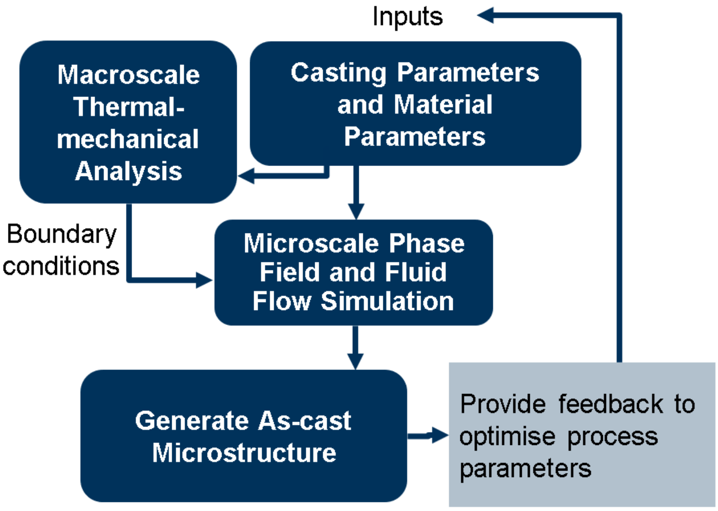

Figure 19. Framework of the multiscale model for TRC

3.2. Reasons for using a multiscale model

In order to correctly model heat transfer in TRC, the temperature distribution of the entire roll needs to be modelled, as well as the temperature of the strip after exiting the rolls. However, when focused on the solidification process, resolution in the microscale model domain must be high enough, so that the cell size is equal or smaller than the interface thickness in the phase field model. The macroscale model has a larger domain size and lower resolution, and it is not necessary for the cell size to be smaller than the grain size. The cell size used in ABAQUS is 2 orders of magnitude larger than that in the microscale model. Meanwhile, the microscale model models at an atomic lengthscale, even though it models solidification within the entire TRC zone between inlet and exit, making the coupled model a multiscale model.

4. Macroscale model

The macroscale model is primarily intended to provide input data, namely temperature field during steady state solidification, for the microscale model. It is also to provide quantitative correlations between the key process parameters, such as the strip thickness and the roll diameter on one side, and the maximum casting speed on the other side. This has been pursued through FEM numerical simulation, which considers plasticity, as well as a simple analytical model for solidification of pure metals, as described as follows.

4.1. FEM model description

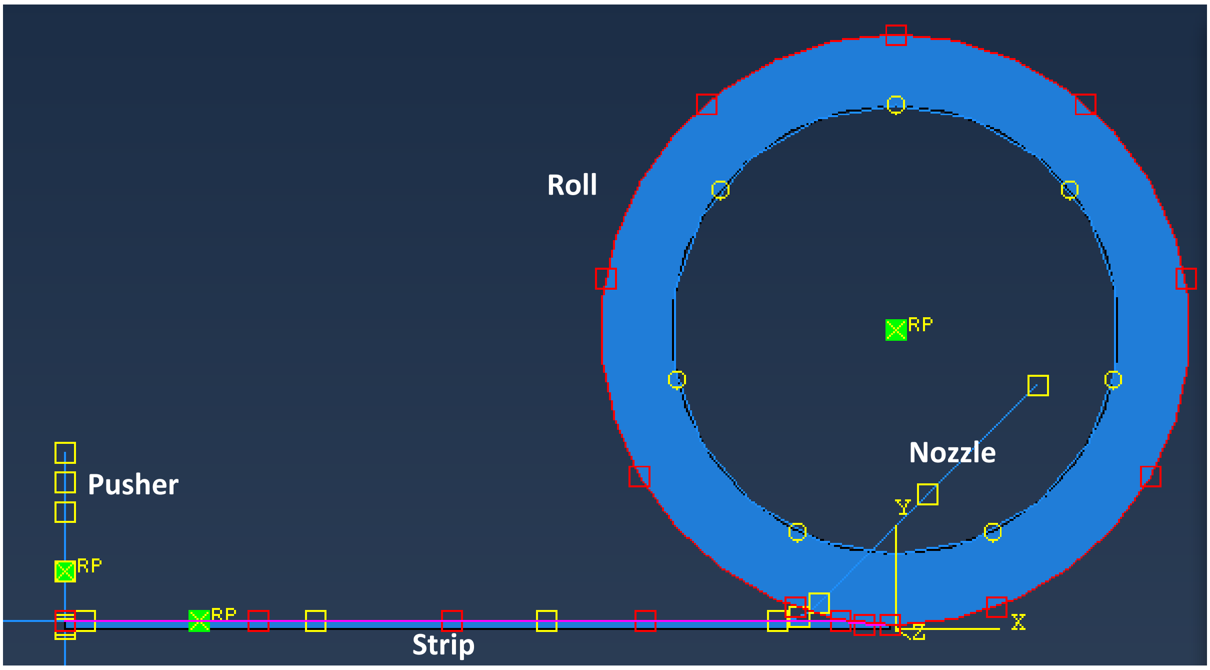

Figure 20. Set up of the macroscale TRC model in ABAQUS

The macroscale thermal-mechanical model is a Lagrangian model built in ABAQUS, consisting of a stainless-steel roll, a rigid surface representing the nozzle, a metal strip, and a pusher that applies pressure on the strip, which is determined by the height of liquid metal in the tundish during TRC. The roll rotates in anticlockwise direction with an angular velocity which is determined by the casting speed. Symmetric boundary conditions are applied at the centreline of the strip, and the effect of gravity is ignored. It is assumed that the melt temperature at the inlet is constant, and the liquid pressure at the inlet, represented by the pressure on the pusher in the model, is constant. The roll has a uniform initial temperature. The temperature of the inner roll surface, representing the cooling channels in the TRC machine, is set at a constant value throughout the process.

4.2. Model parameters

For better comparisons between the modelled results and the experimental data, the dimensions of the TRC model is based on the dimensions of an existing TRC machine used to obtain temperature data during Mg TRC. The diameter of the stainless-steel roll is set at 100 mm, and the nozzle has a setback distance of 20 mm.

The strip thickness is set at 1.6 mm, therefore the distance between the roll surface and the centreline at the exit is 0.8 mm. The strip has a mesh size of 0.3 mm. The roll has a mesh size of 0.3 mm on the outer surface, and the mesh size increases to 10 mm on the inner surface, in order to improve efficiency of the model while keeping accuracy of the temperature at the roll-strip interface.

4.3. Material parameters

The macroscale model can be applied to TRC of different alloys by changing the input thermal and mechanical properties of the strip material, including density, solidus and liquidus temperatures, latent heat, specific heat capacity, thermal conductivity, thermal expansion coefficient, Young’s modulus, and stress-strain data.

The material properties of Al, Mg and AZ31 are obtained from literature, as shown in the table below. The thermal conductivity, thermal expansion coefficient, Young’s modulus, and stress-strain data are dependent on temperature. The material properties used to define the alloy strip material in the ABAQUS model are listed in Table **1** and Appendix 1.

Table 1. Material properties of Al, Mg and AZ31 [1-3]

	Al	**Mg**	**AZ31**
Density (kg/m^3)	2700	1738	1780
Solidus temperature (°C)	659	645	424
Liquidus temperature (°C)	660	650	635
Latent heat (J/kg)	397000	368192	340000
Specific heat capacity (J/(kg·K))	See Appendix 1.2	1020	See Appendix 1.3

The roll material used is tool steel AISI H13. Material properties of the roll are shown below.

Table 2. Material properties of tool steel AISI H13 [1]

Density (kg/m^3)	7800
Young's modulus (Pa)	2.1x10^{11}
Poisson ratio	0.3
Specific heat capacity (J/(kg·K))	1110

Table 3. Thermal conductivity of tool steel AISI H13 as a function of temperature

Thermal conductivity (S/m)	**Temperature (°C)**
25	20
29	400
30	1110

4.4. Parameter studies

To improve accuracy and efficiency of the macroscale model, the model is run with various mesh size and simulation time. The temperature profiles of the strip are compared, in order to determine the minimum simulation time to reach steady state in the modelled temperature, and the maximum mesh size allowed to achieve sufficient accuracy in the modelled temperature profiles.

As shown in Figure 21, the temperature profiles along the centreline of the strip are obtained at different times during a simulation. The beginning of the plot indicates temperature of the melt, and the end of the plot represents the end of the strip that has left the exit. The temperature profile of the solidification zone is shown to reach steady state after a simulation time of 1 s. It is also shown that there is reheating in the strip after leaving the exit, which is due to the low casting speed causing high amount of deformation of the strip, resulting in a release of elastic energy after the strip has left the exit.

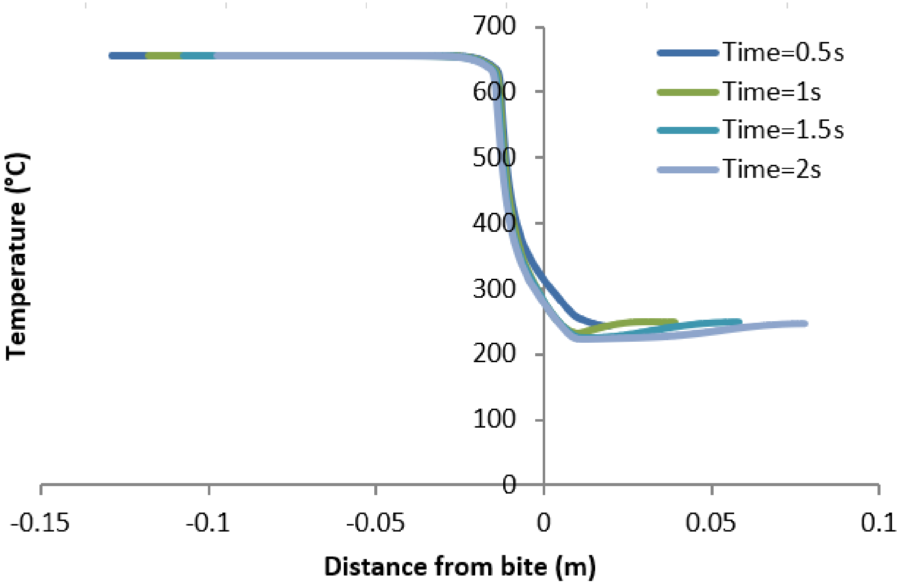

Figure 21. The temperature measured along the centreline of the strip, taken at different simulation times. The model is of pure Al TRC, with a casting speed of 2 m/min and without melt superheating.

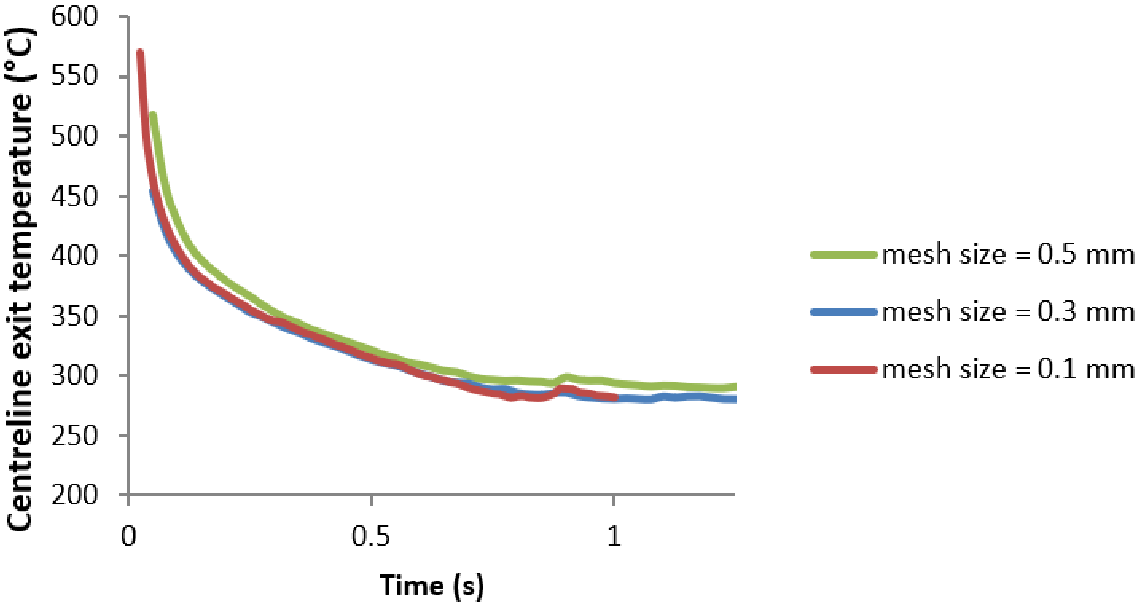

Figure 22. The centreline exit temperature measured as a function of time, for models with different mesh sizes in the strip. The model is of pure Al TRC, with a casting speed of 2 m/min and without melt superheating.

The macroscale model was ran with various mesh sizes applied in the strip. In each case, the mesh size of the outer surface of the roll is the same as the mesh size of the strip. The case where the mesh size is 0.1 mm only ran for 1 s, because the process was too slow, and the time of 1 s is enough for reaching the steady state, according to the simulation time study above. As shown in Figure 22, as the mesh size decreases from 0.5 mm to 0.3 mm, a significant difference in the centreline exit temperature at steady state is observed, meanwhile as the mesh size drops below 0.3 mm, the changes in centreline exit temperature are sufficiently small. Therefore, to reduce simulation time, a mesh size of 0.3 mm is applied to the strip in the macroscale model.

5. Microscale model

The microscale model consists of a phase field-Potts model, and a fluid flow model.

5.1. Fluid flow model

5.1.1. Modelling motion of solid grains in fluid flow in a continuous domain

Difficulties in modelling Bingham fluid, which exhibits non-Newtonian properties and behaves as a rigid body at low stress and a viscous fluid at high stress, arise due to the lack of analytical solutions for complex flow fields. Numerical schemes were developed based on traditional FE or FD discretization of appropriate PDEs. More efficient numerical methods are required for modelling complex rheology properties and geometries.

There has been an increasing interest in using the lattice Boltzmann method (LBM) to solve complex fluid flow problems. With easy implementation of parallel computing due to the explicit scheme and local computations, a linear streaming process, and more straightforward applications of complex boundary conditions, LBM is less computationally expensive than traditional Navier-Stokes solvers [1], and is of higher efficiency than the incompressible spectral solver [2].

Several lattice Boltzmann models for Bingham plastics have been proposed. Tang et al. [3] employed the He-Luo incompressible LBM [4], with a modified local relaxation time which is dependent on the apparent viscosity calculated based on the Papanastasiou exponential modification approach [5]. However, the proposed method causes the local relaxation time to approach infinity at high viscosities, resulting in negligible collisions between particles. Wang and Ho [6] incorporated the effect of local shear rate into the equilibrium distribution function, but inconsistencies were found between the correct momentum equation and the one derived from the suggested equilibrium distribution. In this paper, the equilibrium distribution function from the He-Luo model is updated to reflect the effects of local shear rate, to model Bingham fluid behaviour.

5.1.2. Bingham fluid model

The Papanastasiou exponential modification approach [6] is employed to avoid discontinuity in the viscosity expression for Bingham fluid. Shear stress and shear rate varies with

$$\tau_{\alpha\beta} = \mu\dot{\gamma}_{\alpha\beta} + \tau_y\left[1 - \exp\left(-m\left|\dot{\gamma}_{\alpha\beta}\right|\right)\right] \tag{97}$$

Wang and Ho [7] proposed the following momentum equation for Bingham plastics, substituting the Newtonian viscosity in eq. (15), the momentum equation obtained via Chapman-Enskog expansion of the discrete lattice Boltzmann equation, with the apparent viscosity for Bingham fluid derived from eq. (97).

$$\frac{\partial \rho u_\alpha}{\partial t} + \frac{\partial(\rho u_\alpha u_\beta)}{\partial x_\beta} = -\frac{\partial P}{\partial x_\alpha} + \frac{\partial}{\partial x_\beta}\left\{\mu + \frac{\tau_y}{\left|\dot{\gamma}_{\alpha\beta}\right|}\left[1 - \exp\left(-m\left|\dot{\gamma}_{\alpha\beta}\right|\right)\right]\right\}A_{\alpha\beta} \tag{98}$$

where $A_{\alpha\beta} = \frac{\partial u_\alpha}{\partial x_\beta} + \frac{\partial u_\beta}{\partial x_\alpha}$, and $\left|\dot{\gamma}_{\alpha\beta}\right| = \sqrt{\frac{1}{2}trA_{\alpha\beta}^2}$.

5.1.3. A modified incompressible lattice Boltzmann model for Bingham fluid

If the plastic viscosity μ is taken as $\mu = \frac{2\tau-1}{6}\rho$, and a parameter κ is defined as $\kappa = \frac{\tau_y}{\left|\dot{\gamma}_{\alpha\beta}\right|}\left[1 - \exp\left(-m\left|\dot{\gamma}_{\alpha\beta}\right|\right)\right]$, then eq. (98) can be seen as eq. (15) with an additional term $\frac{\partial}{\partial x_\beta}(\kappa A_{\alpha\beta})$ on the right hand side. Therefore, a new term could be added to the equilibrium particle distribution function to achieve eq. (98).

$$f_i^{eq,new} = \rho w_i\left[1 + 3e_i \cdot u + \frac{9}{2}(e_i \cdot u)^2 - \frac{3}{2}u^2\right] + G_i \tag{99}$$

As the first two moments of the equilibrium distribution function must remain the same as the macroscopic density ρ and momentum density ρu, the added G_i term must meet the following conditions.

$$\sum_i G_i = 0 \tag{100}$$

$$\sum_i e_i G_i = 0 \tag{101}$$

During the derivation of eq. (15), the following mass and momentum equations are obtained using Chapman-Enskog expansion of the lattice Boltzmann equation.

$$\frac{\partial \rho u}{\partial t_{(0)}} + \frac{\partial}{\partial x_\beta} \Pi^{(0)}_{\alpha\beta} = 0 \tag{102}$$

$$\frac{\partial \rho}{\partial t} + \frac{\partial (\rho u_\alpha)}{\partial x_\alpha} = 0 \tag{103}$$

$$\frac{\partial \rho u}{\partial t} + \frac{\partial}{\partial x_\beta} \Pi_{\alpha\beta} = 0 \tag{104}$$

The momentum flux tensor $\Pi_{\alpha\beta}$ is defined as

$$\Pi_{\alpha\beta} = \Pi^{(0)}_{\alpha\beta} + \frac{2\tau - 1}{2\tau} \Pi^{(1)}_{\alpha\beta} = \sum_i e_{i\alpha} e_{i\beta} (f_i^{eq} + \frac{2\tau - 1}{2\tau} f_i^{(1)}) \tag{105}$$

where $f_i^{(1)} = -\tau\big(\partial_{t(0)} + e_{i\alpha}\partial_\alpha\big) f_i^{eq}$.

With the updated equilibrium distribution function, the momentum equation becomes

$$\begin{aligned} \frac{\partial \rho u}{\partial t} + \frac{\partial}{\partial x_\beta} \Pi^{new}_{\alpha\beta} &= \frac{\partial \rho u}{\partial t} + \frac{\partial}{\partial x_\beta} \sum_i e_{i\alpha} e_{i\beta} (f_i^{eq,new} + \frac{2\tau - 1}{2\tau} f_i^{(1),new}) \\ &= B + \frac{\partial}{\partial x_\beta} \sum_i e_{i\alpha} e_{i\beta} (G_i + \frac{1 - 2\tau}{2} \big(\partial_{t(0)} + e_{i\gamma}\partial_\gamma\big) G_i) = 0 \end{aligned} \tag{106}$$

where B is $\frac{\partial \rho u}{\partial t} + \frac{\partial}{\partial x_\alpha} \Pi_{\alpha\beta}$ calculated using the old equilibrium distribution function, eq. (8).

$$B = \rho \left(\frac{\partial u_\alpha}{\partial t} + \frac{\partial (u_\alpha u_\beta)}{\partial x_\beta} \right) + \frac{\partial P}{\partial x_\alpha} - \nu \frac{\partial}{\partial x_\beta} (\frac{\partial \rho u_\alpha}{\partial x_\beta} + \frac{\partial \rho u_\beta}{\partial x_\alpha}) \tag{107}$$

To obtain eq. (98) from the new equilibrium distribution function, the following condition must be met.

$$\frac{\partial}{\partial x_\beta} \sum_i e_{i\alpha} e_{i\beta} (G_i + \frac{1 - 2\tau}{2} \big(\partial_{t(0)} + e_{i\gamma}\partial_\gamma\big) G_i) = -\frac{\partial}{\partial x_\beta} (\kappa A_{\alpha\beta}) \tag{108}$$

As κ is independent of τ, eq. (108) can be separated into the following two equations.

$$\sum_i e_{i\alpha} e_{i\beta} G_i = -(\kappa A_{\alpha\beta}) \tag{109}$$

$$\partial_\beta \partial_{t(0)} \sum_i e_{i\alpha} e_{i\beta} G_i + \partial_\beta \partial_\gamma \sum_i e_{i\alpha} e_{i\beta} e_{i\gamma} G_i = 0 \tag{110}$$

From eq. (109),

$$\partial_\beta \partial_{t(0)} \sum_i e_{i\alpha} e_{i\beta} G_i = -\partial_\beta \partial_{t(0)} (\kappa A_{\alpha\beta}) \tag{111}$$

Using eq. (102) and assuming κ and ρ are constant, $-\partial_\beta \partial_{t(0)} (\kappa A_{\alpha\beta})$ can be expressed as

$$\begin{aligned} -\partial_\beta \partial_{t(0)} (\kappa A_{\alpha\beta}) &= -\kappa \partial_\beta \left(\partial_\beta \partial_{t(0)} u_\alpha + \partial_\alpha \partial_{t(0)} u_\beta \right) \\ &= \frac{\kappa}{\rho} \partial_\beta \left[\partial_\beta \partial_\gamma \left(\delta_{\alpha\gamma} P + \rho u_\alpha u_\gamma - \kappa A_{\alpha\gamma} \right) + \partial_\alpha \partial_\gamma (\delta_{\beta\gamma} P + \rho u_\beta u_\gamma \right. \\ &\left. - \kappa A_{\beta\gamma}) \right] \end{aligned} \tag{112}$$

Assuming the third order or higher space derivatives of velocity and pressure are negligible, $-\partial_\beta \partial_{t(0)} (\kappa A_{\alpha\beta}) = 0$. Therefore, to satisfy eq. (110) the following must be true.

$$\sum_i e_{i\alpha} e_{i\beta} e_{i\gamma} G_i = 0 \tag{113}$$

The added G_i term in the equilibrium distribution function, which satisfies eq (100), eq. (101), eq. (109), and eq. (113), can be calculated as follows.

$$G_i = \begin{cases} \dfrac{\kappa}{2} A_{yy}, & i = 1, 3 \\ \dfrac{\kappa}{2} A_{xx}, & i = 2, 4 \\ -\dfrac{\kappa}{4} A_{xx} - \dfrac{\kappa}{4} A_{yy} - \dfrac{\kappa}{2} A_{xy}, & i = 5, 7 \\ -\dfrac{\kappa}{4} A_{xx} - \dfrac{\kappa}{4} A_{yy} + \dfrac{\kappa}{2} A_{xy}, & i = 6, 8 \\ 0, & i = 0 \end{cases} \tag{114}$$

where $A_{\alpha\beta} = \frac{\partial u_\alpha}{\partial x_\beta} + \frac{\partial u_\beta}{\partial x_\alpha}$.

5.2. Phase field-Potts model

Modelling of microstructure evolution during solidification is based on a combination of the phase field model and a Potts model for calculating grain orientation.

The solidification process is modelled via the phase field model by Yamaguchi et al. [53]. The phase field evolution is described by eq. (63). The evolution of temperature field under convection is calculated according to eq. (69). Evolution in solute concentration is modelled via the Cahn-Hilliard equation, as described in eq. (54).

The orientation evolution is modelled via a probabilistic Potts model. In the phase field-Potts model by Assadi et al. [91], the free energy function F is related to the mismatch energy of each cell, calculated from its orientation and the orientations of neighbouring cells, as shown in the following equation.

$$F = \int [f\left(\phi, x_B^L, x_B^\alpha, x_B^\beta, T\right) + \frac{1}{2}\,\varepsilon^2\,|\nabla\phi|^2 + \mathrm{g}]\mathrm{dV} \tag{115}$$

where f is the local volumetric free energy density, g is the mismatch energy between the given cell and its neighbours, x_B^L is the liquid composition, x_B^α, x_B^β are the compositions of different phases, and ε is the solid-liquid interface thickness parameter.

The mismatch energy g is calculated from

$$\mathrm{g} = \frac{1}{2}\varepsilon_0^2 \sum_i a_i\,\phi\,\phi_i\,E_i(\theta, \theta_i) \tag{116}$$

where ε_0 is the grain boundary thickness parameter, θ is the orientation of the given cell, θ_i is the orientation of its ith neighbour, a_i is a coefficient that equals 1 and $\frac{\sqrt{2}}{2}$ for the nearest and the second-nearest neighbour in a 2D domain, and E_i is a scaling function calculated from the interfacial energy between the given cell and its neighbours, described as

$$\mathrm{E}_i = |\sin\,[2(\theta - \theta_i)]| \tag{117}$$

A Monte Carlo algorithm is used to determine changes in grain orientation θ. In each time step, a random orientation is generated for each cell. The probability of change in orientation is related to the difference in mismatch energies between the original and the randomly generated new orientation, given by

$$\mathrm{p}(\theta_j) = 1 - \exp\,[k\frac{g_{new} - g_{old}}{RT}] \tag{118}$$

where $\mathrm{p}(\theta_j)$ is the probability of changing to the new cell orientation, R is the molar gas constant, T is the temperature in Kelvin, g_{new} is the mismatch energy calculated from the new orientation, and k is a tuning coefficient related to the orientational ordering.

If the change in orientation reduces the mismatch energy of a cell, the change is accepted. Otherwise, a random number r is generated between 0 and 1, and the new orientation is accepted if $r < \mathrm{p}(\theta_j)$.

Compared to the model by Yamaguchi and Beckermann [50] which involves calculating the gradient of orientation, the Potts model for orientation evolution attributes the crystallographic mismatch energy to grain boundaries rather than to cells, and allows the grain boundaries to have finite thickness in phase field and keeps sharp grain boundaries in the orientation field. Thus the formation of physically unrealistic diffused interfaces at the grain boundaries, and ambiguities in the calculation of orientation gradient, which are problems with the previous model as discussed in Chapter 2.3.3.1, can be avoided.

6. Coupling Models and Different Length Scales

6.1. Implementation of the LB model and coupling to phase field-Potts model

The LB model is implemented in the following steps.

Step 1 – Obtain velocities and distribution functions

At t=0, velocities and distribution functions are initialised. The equilibrium distribution functions are calculated for all regions including boundaries, and used as the initial distribution functions.

For modelling with TRC dimensions, the method of fitting initial velocity distribution according to TRC geometry and casting speed is explained in Chapter 6.2.3.

For t>0, the velocities and distribution functions are read from the previous time step.

Step 2 – Apply boundary conditions to modify the distribution function for all boundaries (rigid, top or bottom symmetry, inlet, outlet)

For modelling with TRC geometries (as described in Chapter 6.2.2), rigid boundary conditions are applied on the top edge of the model domain and the roll surface, and symmetry is applied at the centreline, which are both described in eq. (40), using the mirror method.

Inlet and outlet boundary conditions are described by the open boundary conditions described in eq. (41) by Liu et al. [39], modified by the bounce-back rule from Zou and He [40], assuming constant discharge at the inlet and outlet boundaries.

Phase field distributions obtained in the phase field-Potts model are used as an input for the LB model, and rigid boundary conditions are applied at the solid-liquid interface. Solid phases attached to the roll surface is then pinned to the surface.

Step 3 – Calculate macroscopic properties

Macroscopic velocity and density are calculated for each node from the modified distribution functions, according to eq. (13) and eq. (14).

Step 4 - Calculate equilibrium distribution functions

The equilibrium distribution functions are calculated from the macroscopic velocity and density, shear rate distribution, and additional viscosity for Bingham plastics, according to eq. (99) in the proposed modified lattice Boltzmann model for Bingham fluid. The shear rate, as defined in eq. (97), is calculated from velocity derivatives, which are calculated across the domain via isotropic formulation.

Step 5 – Collision

The collision step is calculated for the entire domain excluding bounce-back rigid boundaries according to eq. (11).

Step 6 – Streaming

The streaming step is calculated in the entire domain according to eq. (12).

Step 7 – Feed the new velocities and distribution functions back to Step 1

The steps are repeated until the total number of iterations are reached.

Coupling to the phase field-Potts model

After each iteration of the LB model, the curl of the velocity field is calculated using isotropic formulation, and used as an input for the orientation calculation in the phase field-Potts model. The macroscopic velocity field is used as an input in the phase field calculations.

After each iteration of the phase field-Potts model, the new phase field distribution is used as an input, to help determine rigid boundaries in the in the next iteration of the LB model.

6.2. Coupling FEM and microlevel models

6.2.1 Thermal boundary conditions

The strip temperature distribution from the macroscale model is fitted to a proposed temperature function, given as

$$T(x,y) = T_{inf} + (T_{inf} - T_{roll}) \cdot \frac{\left(x^2 - x_{inf}^2\right)}{(y - y_0)^2 - R^2 + x_{inf}^2} \tag{119}$$

where T_{inf} is the melt temperature, T_{roll} is the roll surface temperature, x_{inf} is the x-coordinate of a location within the melt where the temperature is constant over the cross section, R is the thermal roll radius, and y_0 is the y-coordinate of the centre of the roll, which is defined as

$$y_0 = R + \delta \tag{120}$$

where δ is the half thickness of the strip.

The temperature profile of the strip from the macroscale model, containing the temperature and x, y-coordinates of each node between the nozzle and the exit, is fitted to eq. (119) using least squares fitting. A set of five coupling parameters, including T_{inf}, T_{roll}, x_{inf}, R, and δ, are used as model parameters for the microscale model, to create the thermal boundary conditions in the microscale model.

Example of implementation

The modelled temperature profile of TRC of AZ31 alloy at a casting speed of 20 m/min, with no melt superheating, is used to obtain a set of coupling parameters. First, the lower bound and upper bound of the coupling parameters are chosen to help the curve fitting process. The fitted parameters are shown in Table 4. A comparison between the temperature profile from the macroscale model and the temperature profile from the coupling model, to be used in the thermal boundary conditions in the microscale model, is shown in Figure 23 and Figure 24.

Table 4. Lower and upper bounds of the coupling parameters, and the fitted parameters

	T_{inf} (K)	T_{roll} (K)	x_{inf} (m)	R (m)	δ (m)
Lower bound	635	0	-0.04	0	0.0008
Upper bound	900	700	0	0.05	0.1
Fitted parameters	670.6743	467.4909	-0.0155	0.0500	0.0008

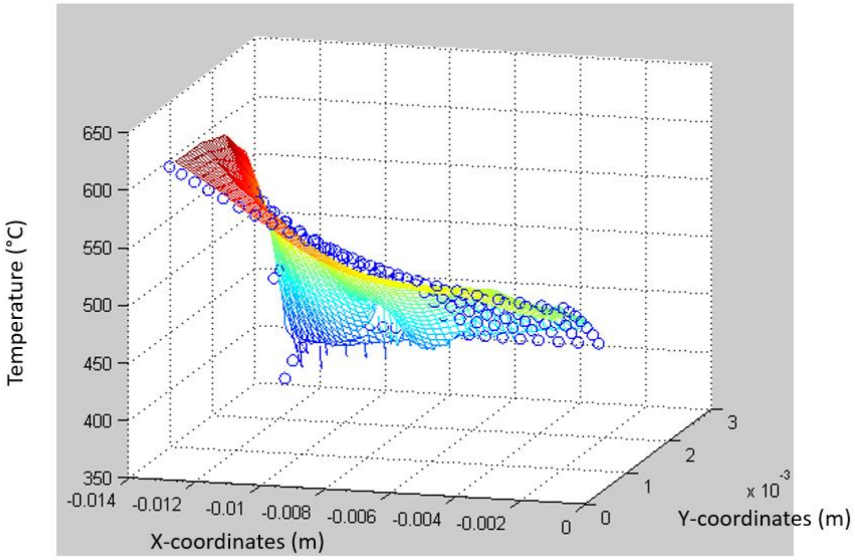

Figure 23. Plot of the temperature profile from the macroscale model (mesh), and the temperature profile generated from the fitted parameters (dots)

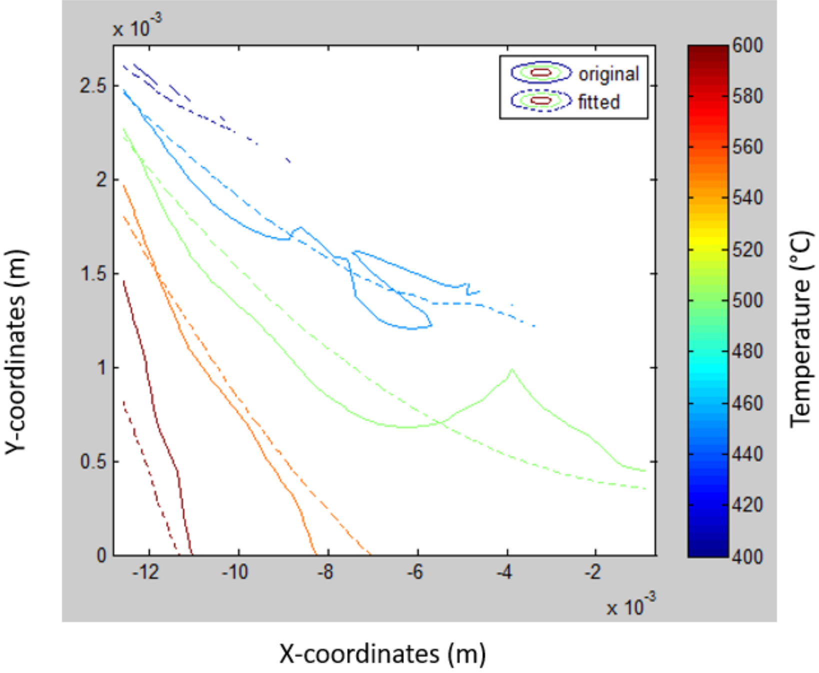

Figure 24. Contour plot of the temperature profiles from the macroscale model and from the fitted model

6.2.2 TRC geometry

TRC geometries such as the strip thickness and roll radius are applied to the microscale model. The roll surface is represented by a rigid surface in the microscale TRC model, where wall boundary conditions, same as at the top boundary, are applied. As symmetry conditions are applied in the centreline in the microscale model, the width of exit is set as half of the casted strip thickness, same as in the macroscale model.

6.2.3 Velocity boundary conditions

Velocity boundary conditions at the inlet and outlet are determined by the inlet velocity and casting speed from the macroscale model. Each node at the inlet and outlet has a macroscopic horizontal velocity equal to the inlet velocity or the casting speed, and zero vertical velocity.

Velocity boundary conditions are applied to the roll surface, which ensures that the macroscopic velocity along the roll surface has a magnitude equal to the TRC casting speed, and a velocity direction along the tangent of the roll surface. For each node at the roll surface, the macroscopic velocities are calculated as

$$\mathrm{u(lby, lbx, 0)} = u_{outlet}\ (y_{roll\ centre} - lby)/R \tag{121}$$

$$\mathrm{u(lby, lbx, 1)} = u_{outlet}\ (x_{roll\ centre} - lbx)/R \tag{122}$$

where lbx and lby are the x- and y-coordinates of the node, $\mathrm{u(lby, lbx, 0)}$ and $\mathrm{u(lby, lbx, 1)}$ are the horizontal and vertical components of the macroscopic velocities at the node, $x_{roll\ centre}$ and $y_{roll\ centre}$ are the x- and y-coordinates of the centre of the roll, u_{outlet} is the TRC casting speed, and R is the roll radius.

At the initialisation stage, a ramping uniform macroscopic velocity profile is fitted to the domain, taking into account the TRC geometry and velocity boundary conditions. Each node has zero initial vertical velocity. The horizontal velocity at each node is calculated by

$$\mathrm{u(lby, lbx, 0)} = \frac{[u_{inlet}\ (x_{roll\ centre} - lbx) + u_{outlet}\ (lbx - x_{inlet})]}{x_{roll\ centre} - x_{inlet}} \tag{123}$$

where x_{inlet} is the x-coordinate of the inlet boundary, $x_{roll\ centre}$ is the x-coordinate of the outlet boundary, which coincides with the roll centre, and u_{inlet} and u_{outlet} are the inlet and outlet velocities.

7. Macroscale model results and discussion

The macroscale temperature distribution of the casted strip is modelled in 2D via ABAQUS. In this section, the sensitivity of a modelling parameter is investigated, the effects of different process parameters on strip solidification are analysed, and a quasi-1D solidification model for TRC is used to gain more insights into the macroscale model observations, and to calculate the theoretical upper bound casting speed for different alloys.

7.1. Calibration of thermal conductance at roll-strip interface

When defining contact properties of the roll-strip interface, one of the model parameters is thermal conductance of the interface gap as a function of distance. The interface gap corresponds to the air gap which exists between the roll and the strip due to their surface roughness, and it cannot be measured experimentally. Table 5 shows an example of the thermal gap conductance as a function of distance, indicating a high conductance when strip and roll are in contact (distance = 0), and zero heat transfer once the strip leaves the roll (distance = 1 mm).

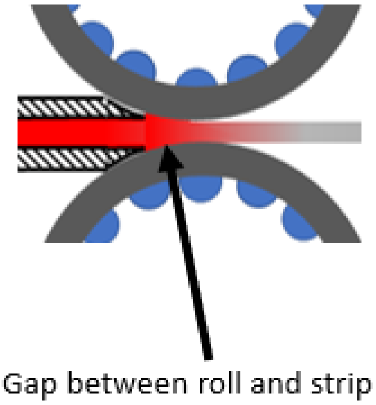

Figure 25. Air gap between the roll and the strip due to imperfect contact affects heat transfer between strip and roll

Table 5. An example of thermal gap conductance as a function of distance

Conductance (W/ (m·K))	Distance (m)
600000	0
0	0.001

As there is uncertainty in the thermal conductance when roll and strip are in contact, the macroscale model is run with different gap conductance values to determine the range that temperature results are sensitive to. Pure Al TRC is modelled with casting speed of 2 m/min, roll diameter of 100 mm, strip thickness of 1.6 mm, and melt temperature of 660 °C. Several nodes along the centreline of the strip with different initial distances from bite are tracked. Figure 26 shows the temperatures of the nodes as they reach the exit. The centreline exit temperature reaches a constant value after 3 cm of strip is produced, and the system reaches steady state. As the gap conductance increases from 10000 (W/ (m·K)) to 30000 (W/ (m·K)), there is a slight decrease in the centreline exit temperature, due to more efficient heat transfer at the roll-strip interface.

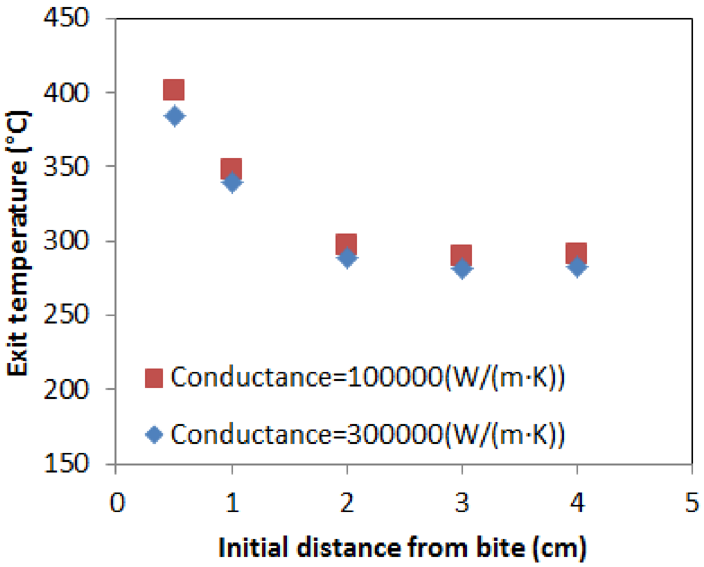

Figure 26. Effect of gap conductance on the centreline exit temperature of the strip in pure Al TRC

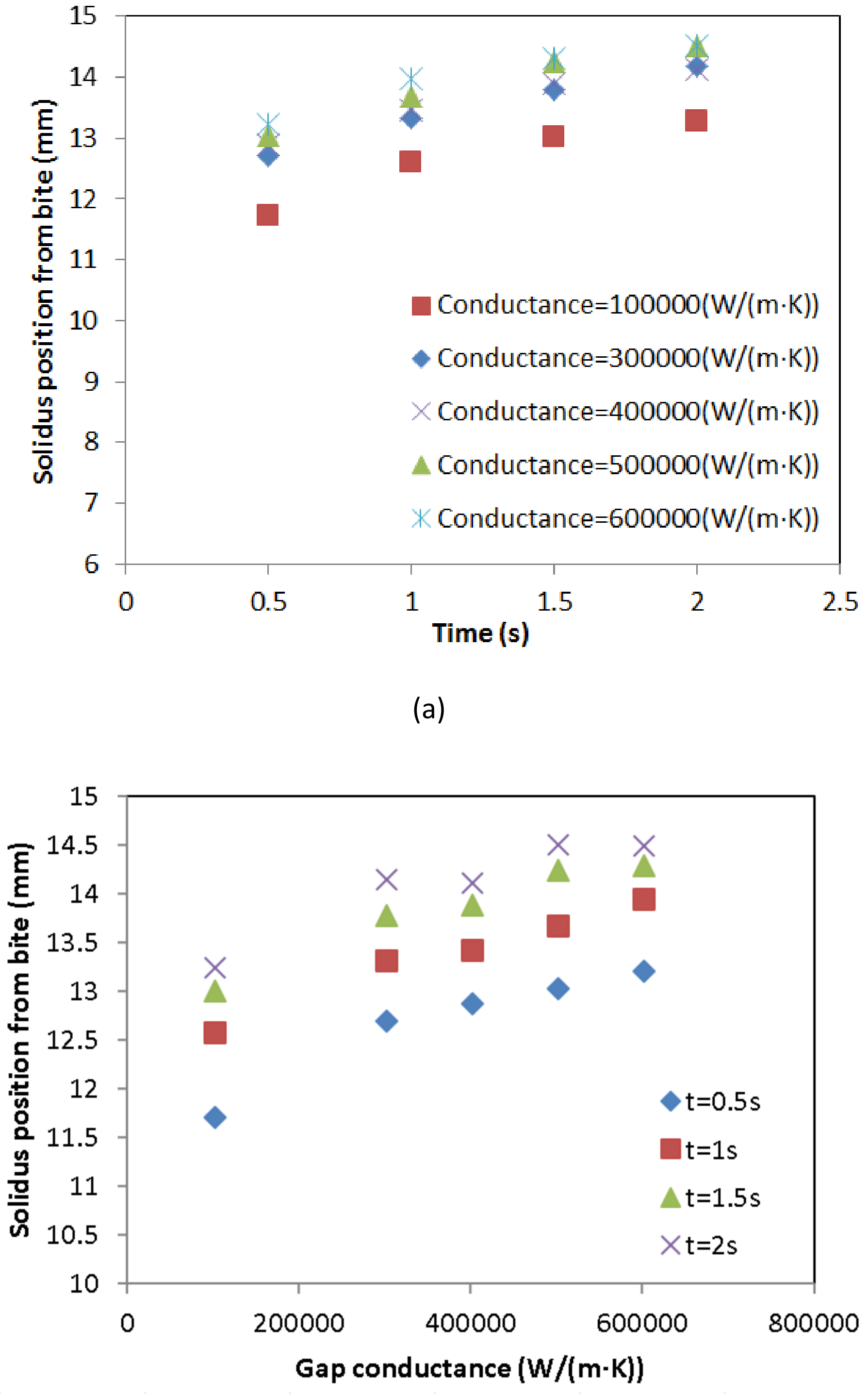

(a)

(b)

Figure 27. Effect of gap conductance on solidus position in pure Al TRC

Figure 27 shows that as gap conductance increases, the modelled temperature profile becomes less sensitive to gap conductance. There is negligible change in the solidus position from bite at steady state when the gap conductance is increased further than 50000 (W/(m·K)). However, the thermal conductance at the roll-strip interface is dependent on the casted alloy and the roll material, and the same value cannot be applied to the TRC model of a different alloy. The gap conductance value can be calibrated by comparing the modelled temperature profiles and temperature measurements from experiments using the same material parameters and casting conditions.

7.2. Effects of casting speed

TRC of Al is modelled with roll diameter of 100 mm, strip thickness of 1.6 mm, melt temperature of 660 °C, using different rolling speeds.

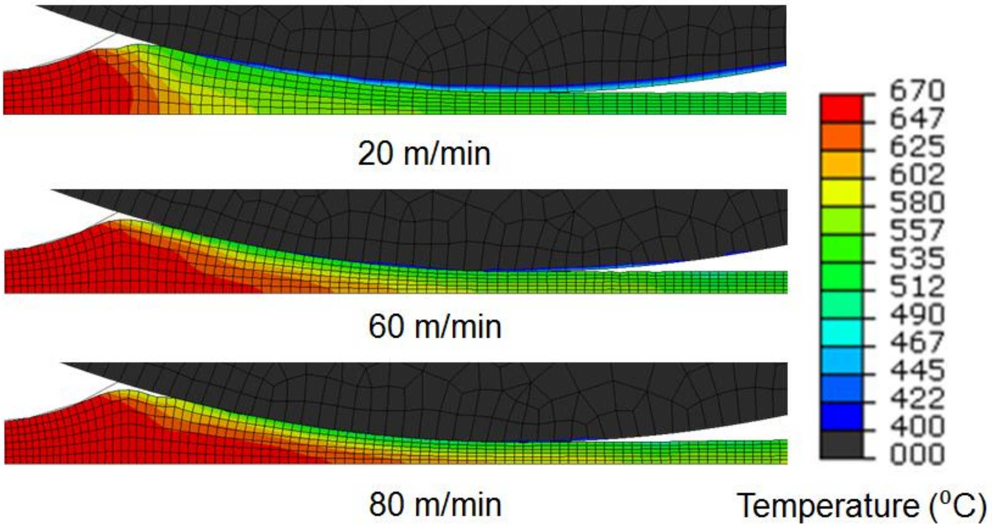

Figure 28. Strip temperature distributions of Al TRC at different casting speeds

Figure 28 shows that as casting speed increases, the depth of the melt sump increases, and strip temperature at the exit increases.

In Figure 29, it is shown that as casting speed increases, the rate of increase in exit temperature on strip surface decreases, while the centreline exit temperature changes with the casting speed at a near constant rate. The temperature difference between centreline and surface exit temperature becomes more significant at a higher casting speed.

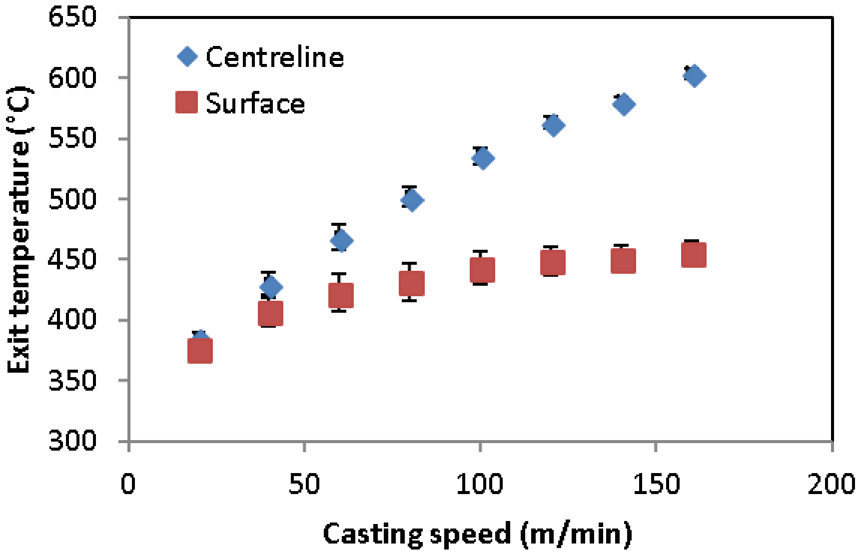

Figure 29. Centreline and surface temperatures obtained at the exit vs casting speed

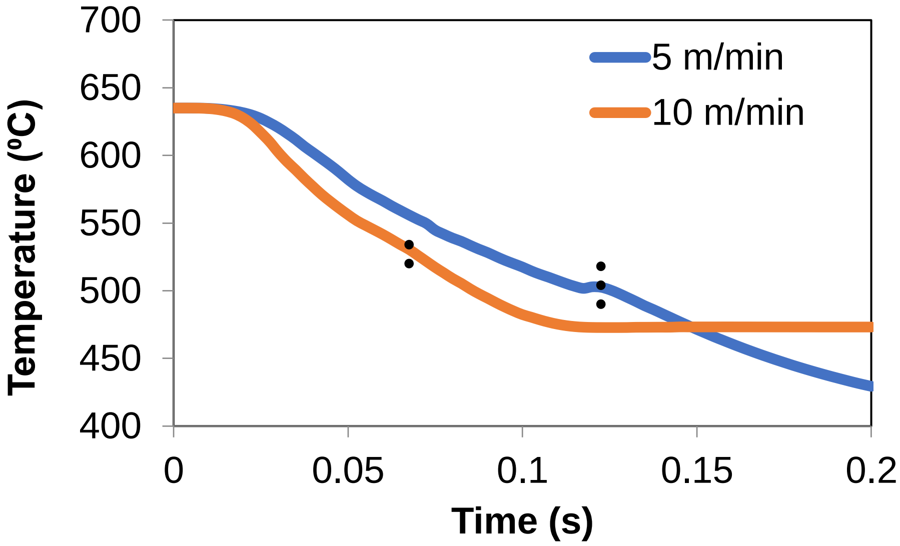

Figure 30. Temperature of a fixed point at the centreline of strip produced at different rolling speeds. Dashed lines indicate the time when the chosen point leaves the rolls.

A fixed node at the centreline of the strip is marked, and the change in temperature of the node with time is plotted in Figure 30. As casting speed increases, the rate of change in temperature of the selected node with time increases, signifying a greater rate of heat transfer. It is also shown that the strip centreline temperature continues to decrease after the node reaches the exit, which is due to heat transfer via conduction from centreline towards surface of the strip. However, the centreline temperature eventually reaches a constant value, as heat loss due to convection of air is not considered in the model.

7.3. Effects of roll temperature

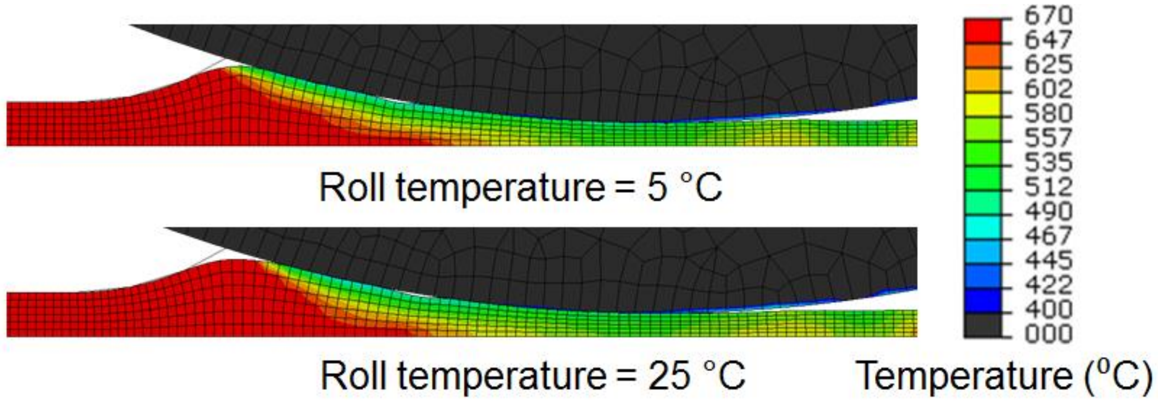

Figure 31. Strip temperature distribution of Al at different roll temperatures, with a casting speed of 60 m/min

TRC of Al with melt temperature of 660 °C, roll diameter of 100 mm, and strip thickness of 1.6 mm is modelled with roll temperature of 5 °C and 25 °C. As shown in Figure 31, reducing the roll temperature from 25 °C to 5 °C has little effect on the temperature profile of the strip, which is contrary to the belief that by improving cooling of the rolls, there is more efficient heat transfer between strip and roll, and a higher casting speed can be achieved.

It is also shown that there is reheating in the strip after the exit, especially along the centreline. This is also shown in Figure 21, and is likely caused by the release of elastic energy from stress developed during the rolling process. In order to reduce the deformation zone during TRC, a higher casting speed can be used to move the solidification front closer to the exit, with the aid of the following quasi-1D solidification model.

7.4. Quasi-1D solidification model for pure systems

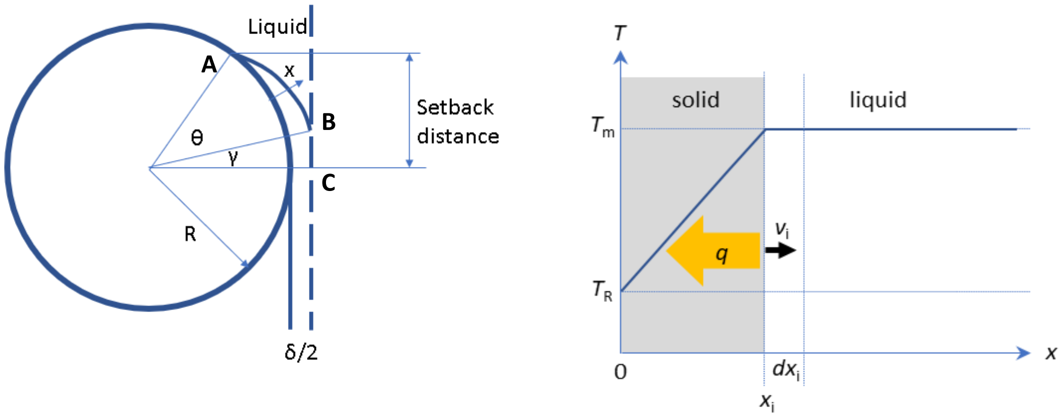

(1) (2)

Figure 32. (a) Schematics for the quasi-1D solidification model for TRC. Only one roll and half the metal strip are shown as the system is symmetrical about the centreline of the strip; (b) Assumed relation between temperature (T) and distance from roll surface (x) for Stefan condition. $\boldsymbol{T_m}$ = melt temperature, and $\boldsymbol{T_R}$ = roll surface temperature.

To understand the effect of roll temperature, a quasi-1D solidification model for TRC is proposed. As shown in Figure 32, symmetry is applied at the centreline of the strip. The TRC system has a roll radius of R and strip thickness of δ. Point A represents first point of contact between the melt and the roll surface, where solidification starts. Point B is the solidus position on the centreline. Point C is the bite position.

The quasi-1D solidification model applies when $R \gg \delta$. It is assumed that: (1) the melt is not superheated ($T_0 = T_m$) and has a uniform temperature (no effect from fluid flow); (2) the temperature profile in the solid phase is predominantly linear; (3) there is perfect thermal contact between metal and roll; (4) the roll surface temperature remains constant.

For solidification of pure metals or eutectic alloys, Stefan condition is used, which gives

$$v_\mathrm{i} = \frac{k}{\rho L} \frac{\partial T}{\partial x}\bigg|_{x_i} \approx \frac{k}{\rho L} \frac{T_\mathrm{m} - T_\mathrm{R}}{x_i} \tag{124}$$

where x_i is the position of the solidification front, ρ, k, L and T_{m} are the material properties (density, thermal conductivity, latent heat of fusion and melting point), T_{R} is the roll surface temperature, and $v_{\mathrm{i}} = \frac{dx_i}{dt}$.

Integration of eq. (124) gives

$$x_{\mathrm{i}}^2 = \frac{2k(T_{\mathrm{m}} - T_{\mathrm{R}})}{\rho L} t \tag{125}$$

where t is the time it takes for solidification to reach the centreline (point B). According to Figure 32, t is related to the casting speed v_R via

$$t = \frac{R\,\theta}{v_R} \tag{126}$$

From geometry, x_i can be calculated as

$$x_i = \frac{R + \delta/2}{\cos{(\gamma)}} - R \tag{127}$$

Combining eq. (125)-(127) gives

$$\cos(\gamma) = f(T_R, v_R) = \frac{R + \delta/2}{R + \left(\frac{2k(T_{\mathrm{m}} - T_{\mathrm{R}})R\,\theta}{\rho L v_R}\right)^{\frac{1}{2}}} \tag{128}$$

The distance between solidus position and bite (d) is obtained by finding the length of segment BC in Figure 32.

$$d = f(\gamma) = (R + \delta/2)\tan{(\gamma)} \tag{129}$$

Combining eq. (128)-(129) gives the solidus position from bite as a function of roll temperature T_R and casting speed v_R. Figure 33 shows how the theoretical solidus position from bite changes with roll temperature at different casting speeds, for TRC of pure Mg with roll radius of 5 cm and strip thickness of 1.6 mm. As shown in Figure 34, the movement in solidus position is negligible as the roll temperature changes significantly, which explains the results observed in Figure 28.

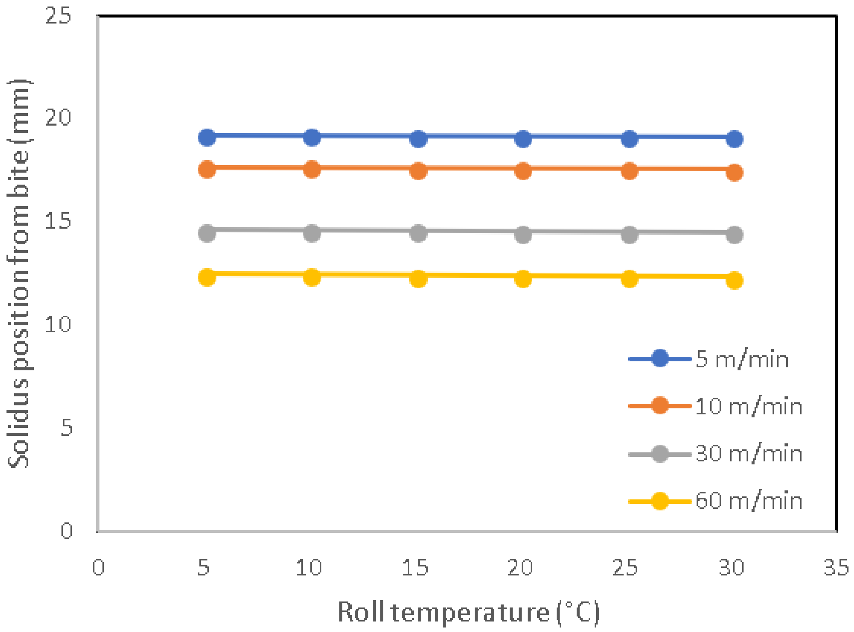

Figure 33. Theoretical solidus position vs roll temperature at different casting speeds

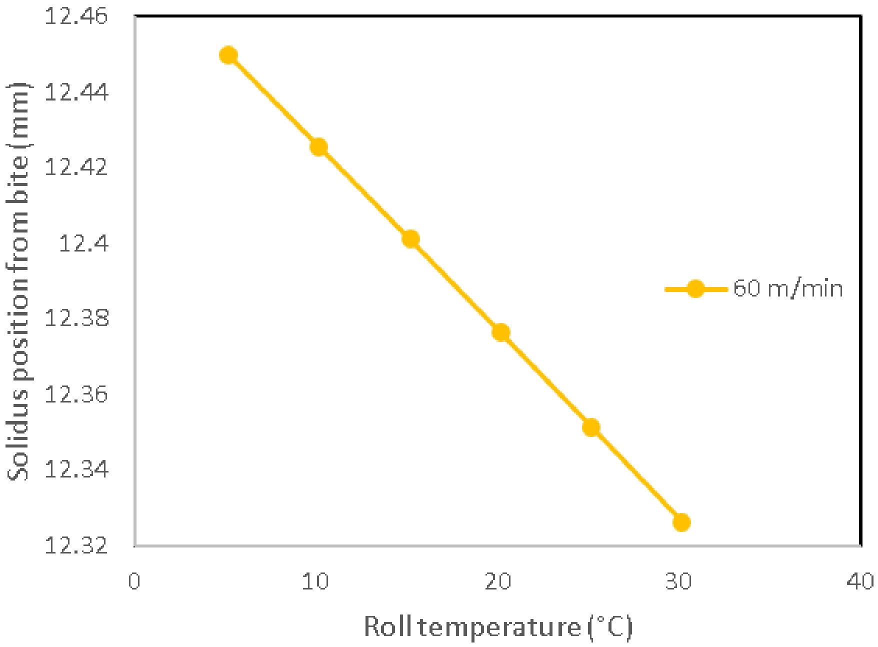

Figure 34. Enlarged graph of theoretical solidus position vs roll temperature, showing only slight decrease in solidus position from bite as roll temperature changes significantly

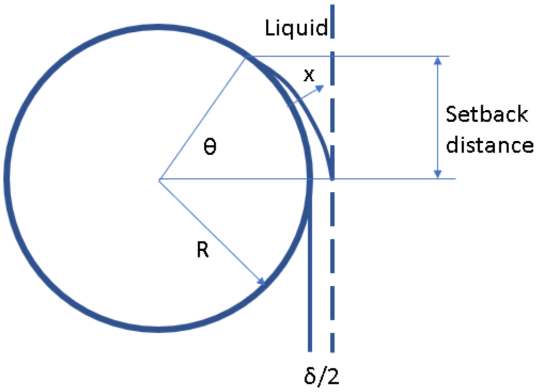

Figure 35. Schematics for calculating the theoretical upper bound casting speed

The theoretical upper bound casting speed is the highest casting speed which ensures solidification finishes before the exit. The quasi-1D model is modified so that the solidification front on the centreline is exactly at the roll bite, as shown in Figure 35. Position of the solidification front x_i reaches half strip thickness $\frac{\delta}{2}$, in the time it takes the roll to rotate an angle of θ. Therefore eq. (125) becomes

$$\left(\frac{\delta}{2}\right)^2 = \frac{2k(T_\mathrm{m} - T_\mathrm{R})}{\rho L} \frac{R\ \theta}{v_{max}} \tag{130}$$

Rearranging eq. (130) gives the upper bound casting speed v_{max} as

$$v_{max} = \frac{8k(T_\mathrm{m} - T_\mathrm{R})}{\rho L} \frac{R\ \theta}{\delta^2} \tag{131}$$

The modified model showed that the theoretical upper bound casting speed is inversely proportional to strip thickness squared (δ^2). Figure 36 shows the calculated theoretical upper bound casting speed as a function of strip thickness for Al and Mg TRC.

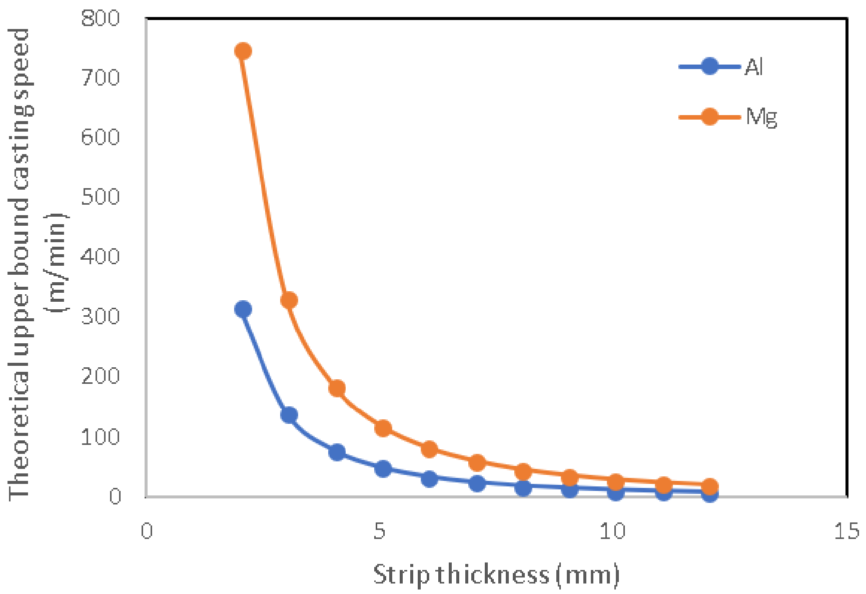

Figure 36. Theoretical upper bound casting speed vs strip thickness, for pure Al and Mg

7.5. Effects of air cooling

As mentioned in Figure 30, the macroscale model does not consider air cooling after the strip exits the rolls, which is not representative of real life situations. In TRC experiments, heat transfer from strip to air due to convection causes further decrease in strip temperature, which can result in a further decrease of strip temperature within the solidification region, due to heat conduction along the casting direction. The amount of heat transferred is proportional to the surface area perpendicular to the direction of heat flux. In the 2D model, conduction within the strip along the casting direction is through an area equivalent to the strip thickness. Therefore as strip thickness increases, the effects of air cooling on the temperature profile of the solidification region become more significant.

To study the effects of air cooling on the strip temperature profile, a rigid surface is placed at 0.2 mm above the strip surface after the strip exits the rolls, with a constant temperature of 10 °C, to represent air convection. Heat transfer by convection is realised by defining the thermal conductance at the interface between the strip and 'air'. An example of the thermal conductance at air-strip interface is given in Table 6. This can be changed to represent different rates of heat transfer from strip surface to air.

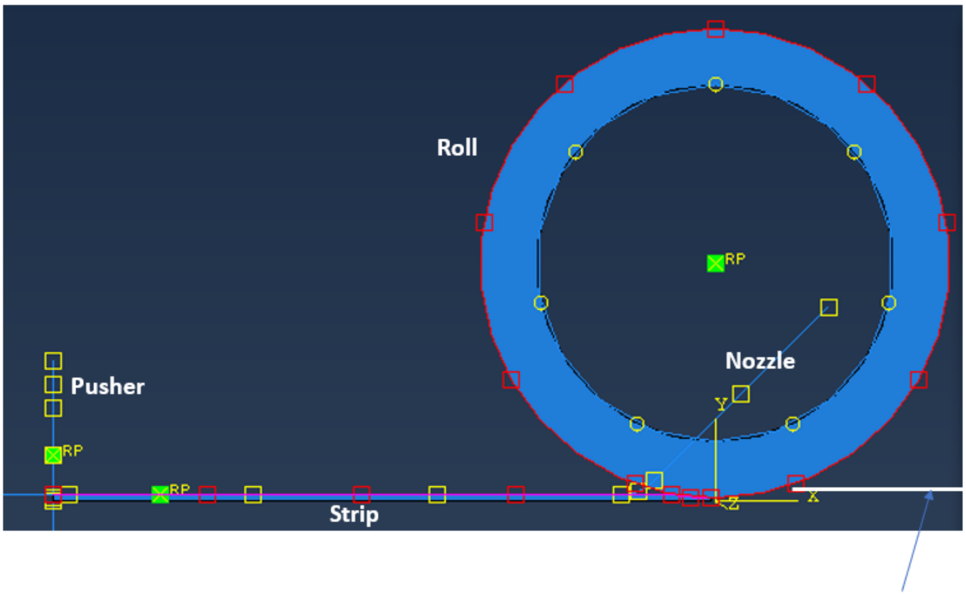

Rigid surface representing air

Figure 37. Set up of the modified macroscale model, with an additional horizontal segment placed just above the strip, representing the effects of air cooling after the strip exits the rolls

Table 6. An example of thermal gap conductance at the air-strip interface

Conductance (W/ (m·K))	Distance (m)
120000	0
0	0.001

TRC of AZ31 is modelled with roll diameter of 100 mm, strip thickness of 1.6 mm, and different values of superheat, casting speed, and interface thermal conductance. Surface and centreline temperatures at the exit are recorded when the model is in steady state. Table 7 shows that with air cooling incorporated into the macroscale model, an increase in casting speed from 20 m/min to 100 m/min results in an increase in centreline exit temperature, and a decrease in surface exit temperature, when thermal conductance values at the air-strip interface and the roll-strip interface remain constant.

As shown in Table 8, at a casting speed of 20 m/min, increasing the thermal conductance values at both roll-strip interface and air-strip interface causes a decrease in both centreline and surface temperatures at the exit. This is due to an increased rate of heat loss from the strip to the surroundings.

Table 7. Strip exit temperatures for AZ31 TRC with a superheat of 5 °C, at different casting speeds

Casting speed (m/min)	Conductance at air-strip interface (W/(m·K))	Conductance at roll-strip interface (W/(m·K))	Exit temperature at centreline (°C)	Exit temperature on surface (°C)
20	1.20E+05	1.20E+06	469.5906	445.3493
100	1.20E+05	1.20E+06	548.6762	397.9059

Table 8. Strip exit temperatures for AZ31 TRC with a superheat of 5 °C, at a casting speed of 20 m/min

Casting speed (m/min)	Conductance at air-strip interface (W/(m·K))	Conductance at roll-strip interface (W/(m·K))	Exit temperature at centreline (°C)	Exit temperature on surface (°C)
20	3.00E+04	3.00E+05	489.0532	475.0579
20	1.20E+05	1.20E+06	469.5906	445.3493

Table 9. Strip exit temperatures for AZ31 TRC with a superheat of 5 °C, at a casting speed of 100 m/min

Casting speed (m/min)	**Conductance at air-strip interface (W/(m·K))**	**Conductance at roll-strip interface (W/(m·K))**	**Exit temperature at centreline (°C)**	**Exit temperature on surface (°C)**
100	1.20E+05	1.20E+06	548.6762	397.9059
100	3.00E+04	1.20E+06	556.0257	410.2285
100	3.00E+04	3.00E+05	575.542	404.2997

Table 9 shows that at a casting speed of 100 m/min, an independent increase of thermal conductance at the air-strip interface results in a decrease in centreline exit temperature, and a greater decrease in surface exit temperature. This corresponds to a greater rate of heat transfer due to convection. Meanwhile, an independent increase of thermal conductance at the roll-strip interface is shown to result in a decreased centreline exit temperature, and a slightly increased surface exit temperature. When the rate of heat transfer at the roll-strip interface increases, the slight increase in exit surface temperature is unexpected. For the heat transfer between roll and strip surface, the gap thickness is affected by the pressure between roll and strip, therefore the temperature field is also affected by the stress being applied by the rolls. This shows the limitations of modelling heat transfer coefficients at interfaces as a function of distance.

Table 10. Strip exit temperatures for AZ31 TRC with different superheat and different casting speeds

Superheat (°C)	**Casting speed (m/min)**	**Conductance at air-strip interface (W/(m·K))**	**Conductance at roll-strip interface (W/(m·K))**	**Exit temperature at centreline (°C)**	**Exit temperature on surface (°C)**
0	10	1.20E+05	1.20E+06	430.2677	412.0342
0	20	1.20E+05	1.20E+06	462.0061	466.0361
5	20	1.20E+05	1.20E+06	469.5906	445.3493

As shown in Table 10, a 5 °C increase in melt temperature results in a slight increase in exit centreline temperature, and a significant decrease in exit surface temperature, which is unexpected. Meanwhile, with a constant melt temperature, both centreline and surface temperatures at exit increases as casting speed increases from 10 m/min to 20 m/min, which is different to observations in Table 7, as casting speed increases from 20 m/min to 100 m/min.

The abnormality in the results in Table 10 could be due to the spring-back effect and the method of implementing air cooling in the model. As air cooling is modelled by defining the heat transfer coefficient as a function of distance between the strip surface and the fixed 'air' surface, expansions of the strip after the exit causes an increase in heat transfer between 'air' and strip surface. Therefore the results of a dynamic analysis of air convection at the strip surface may not be reliable.

As discussed above, there are several cases where the independent changes of casting speed, melt temperature and thermal conductance at the roll-strip interface results in opposite effects of the centreline and surface temperatures at exit, indicating that heat transfer is more significant at the roll-strip and air-strip interfaces, compared to within the strip itself, which does not represent the reality. Therefore, when applying the modified macroscale model to manufacturing processes where the as-cast strip surface is rapidly cooled, the thermal conductance function of the air-strip interface should be calibrated using experimental temperature data measured on the strip surface at different distances to the exit.

8. Microscale model results and discussion

Some test cases are modelled with the two components of the microscale model, the Bingham LB model and the phase field-Potts model, to conduct parameter studies and understand the limitations of the models.

8.1. Bingham LB model

A 2D channel flow of Bingham fluid with a uniform inlet velocity is modelled in a domain of 102 × 602 uniform D2Q9 lattices, with a cell size of 1.5 µm. As shown in Figure 38, the rate of change of normalised viscosity with shear rate is controlled by changing the Bingham number (B_n), defined as $B_n = \frac{D\,\tau_y}{\eta\bar{U}}$, and a dimensionless sensitivity parameter λ, defined as $\lambda = \frac{m\,\tau_y}{\eta}$, which is related to the sensitivity of viscosity to shear rate.

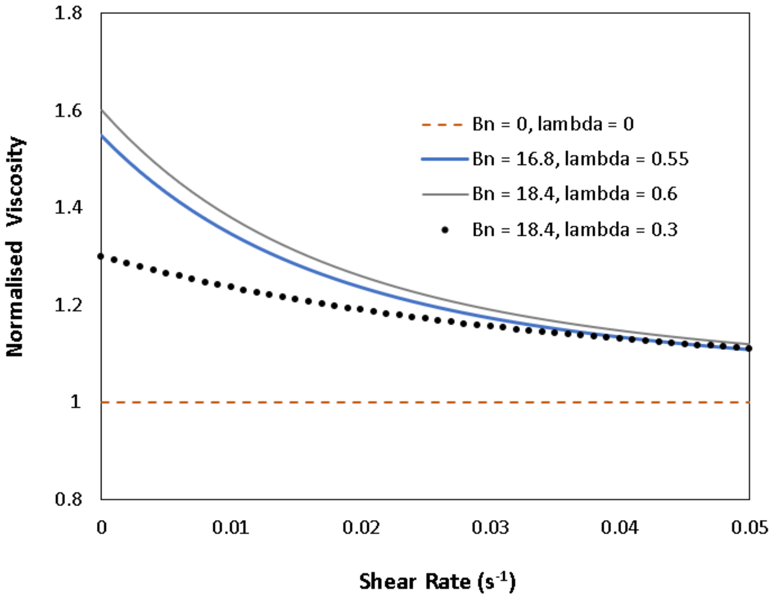

Figure 38 Normalised viscosity against shear rate for different values of Bn and λ

Effects of B_n and λ on velocity profiles

Figure 39 shows that for $B_n < 20$, the Bingham number has a negligible effect on the velocity profile, whereas as λ increases, the fluid viscosity increases more drastically near the centreline, where shear rate is higher, resulting in a bigger drop in streamwise velocity approaching the centreline (Figure 40). It is also observed in Figure 39 that changes in velocity are more significant along the diagonal directions, resulting in a criss-cross pattern in the velocity distribution. This effect is amplified as λ increases.

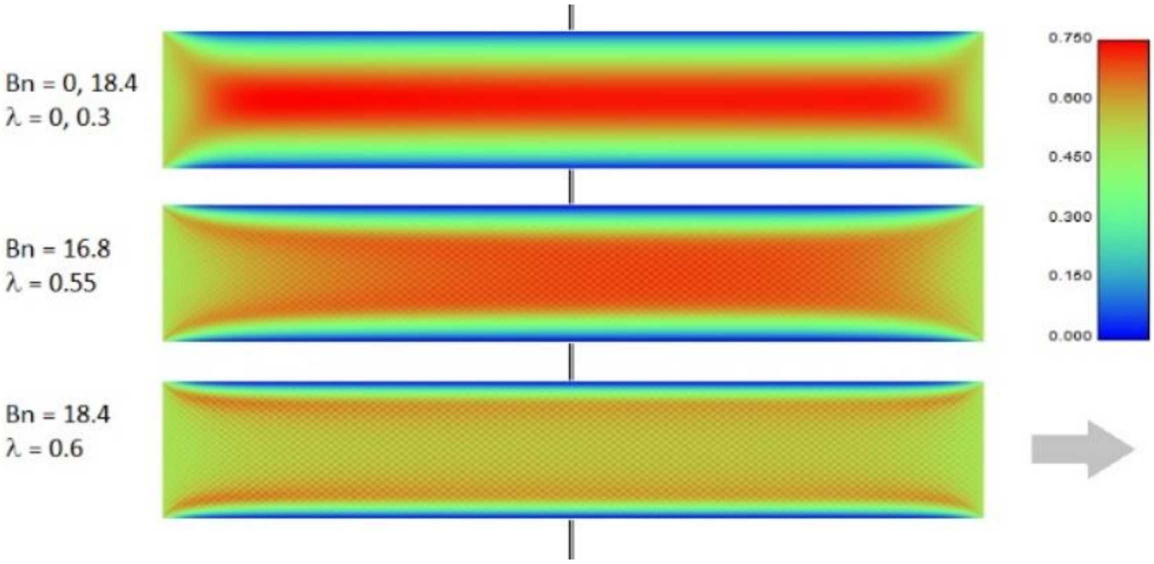

Figure 39 Streamwise velocity distributions of 2D channel flows with different values of Bn and λ. The vertical line indicates where velocity profiles are measured. Inlet velocity is 0.5 m/s.

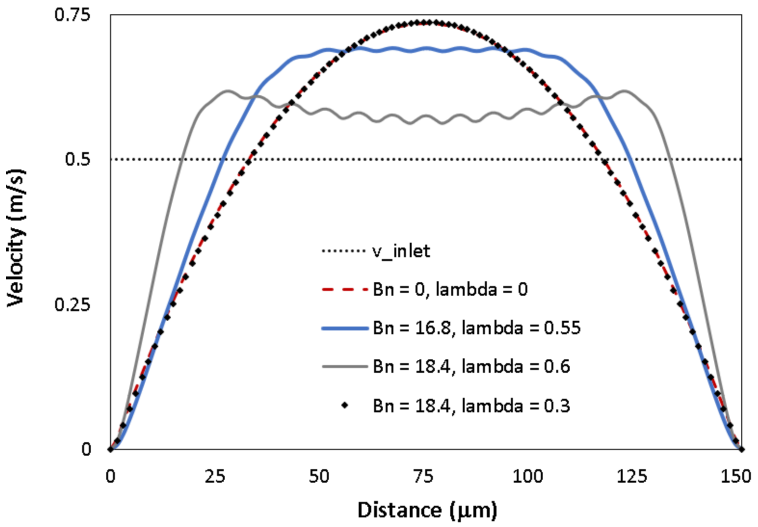

Figure 40. Velocity profiles measured in the middle of the 2D channel, when inlet velocity is 0.5 m/s

Increased fluctuations in the velocity profile are observed as λ and B_n increase, as shown in Figure 41 and Figure 42. These fluctuations are observed near the centre of the channel, where the Bingham fluid behaves like a rigid body under a high shear stress.

It is also shown in Figure 43 that for a small λ parameter (λ = 0.3), B_n has little effect on the velocity profiles which closely resemble that of a Newtonian fluid.

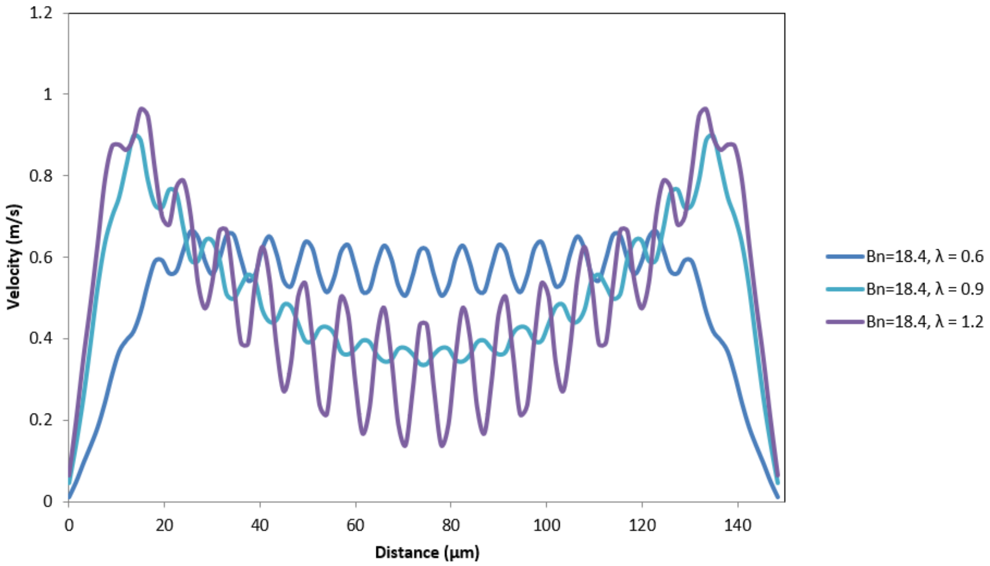

Figure 41 Streamwise velocity profiles of Bingham fluid with different λ values at Bn = 18.4, with inlet velocity of 0.5 m/s

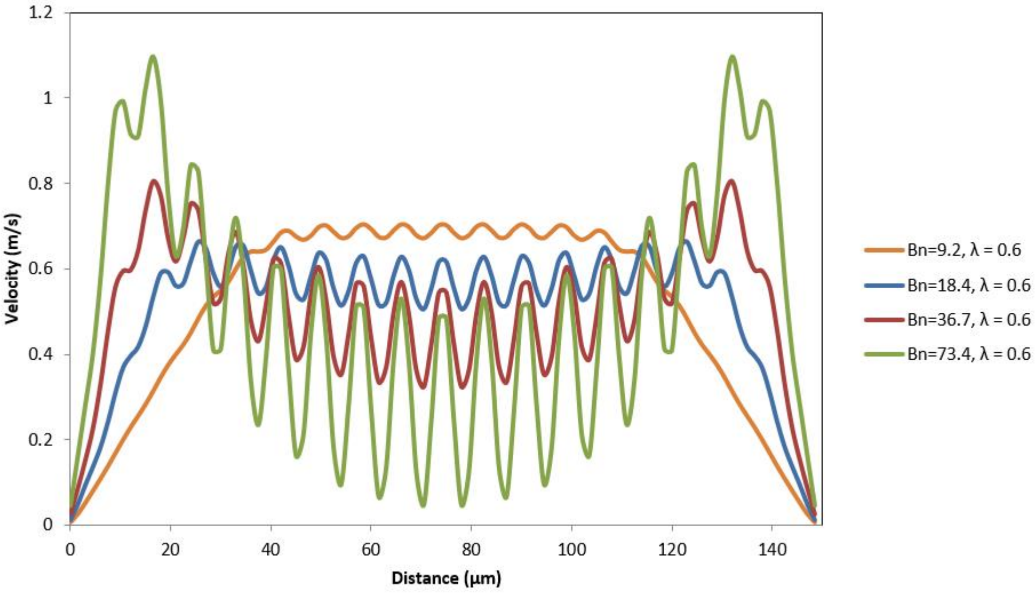

Figure 42 Streamwise velocity profiles of Bingham fluid with different Bn values at λ = 0.6, with inlet velocity of 0.5 m/s

Effects of domain size on the velocity fluctuations

The model is then extended onto a domain of 202 × 602 cells, doubling the original channel width. By comparing the cases in Figure 42 where $B_n = 36.7$ and 73.4, and $\lambda = 0.6$, and the cases in Figure 43 where $B_n = 36.4$ and 72.7, and $\lambda = 0.6$, it is shown that by increasing the cell count along the channel width, the fluctuation amplitudes of the velocity profiles are greatly reduced.

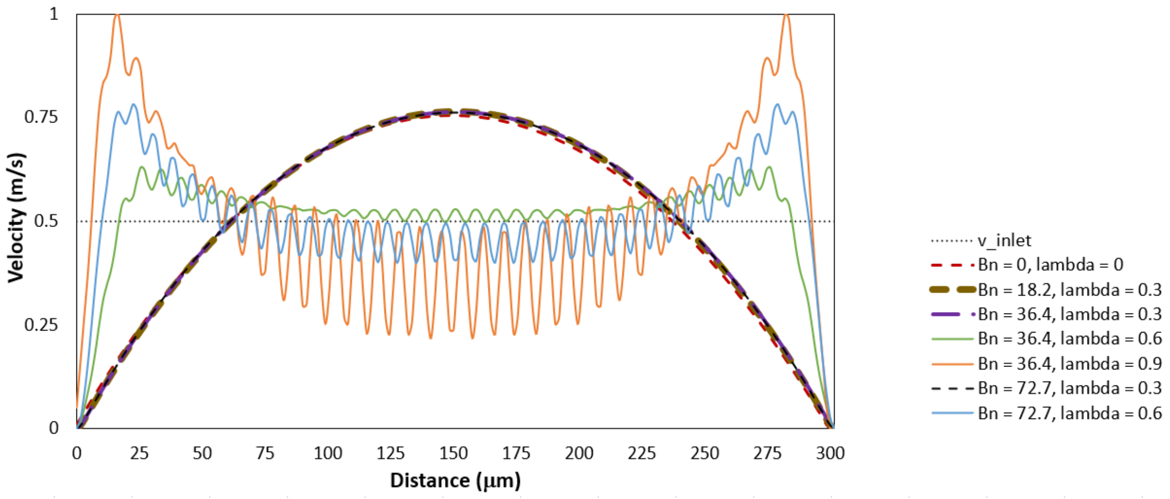

Figure 43 Velocity profiles for 2D channel flow with a doubled channel width (domain size is 202 × 602), with different values of Bn and λ, with inlet velocity of 0.5 m/s

Effects of inlet velocity on the velocity fluctuations

The model is run with a reduced inlet velocity (0.05 m/s). By comparing the velocity profiles in Figure 43 and Figure 44, it is found that at a reduced inlet velocity (0.05 m/s), fluctuations in the velocity profile is reduced even when high values of Bingham and sensitivity parameters are used. Whereas, when a high inlet velocity is used, fluctuations in the velocity profile near the middle of the channel tend to appear with a large enough λ parameter.

The effects of Bingham and sensitivity parameters on the velocity profile are also shown to depend on the inlet velocity. At a lower inlet velocity, the velocity profile shows a more significant dependence on the λ parameter, and appears less dependent on the Bingham parameter, as shown in Figure 44.

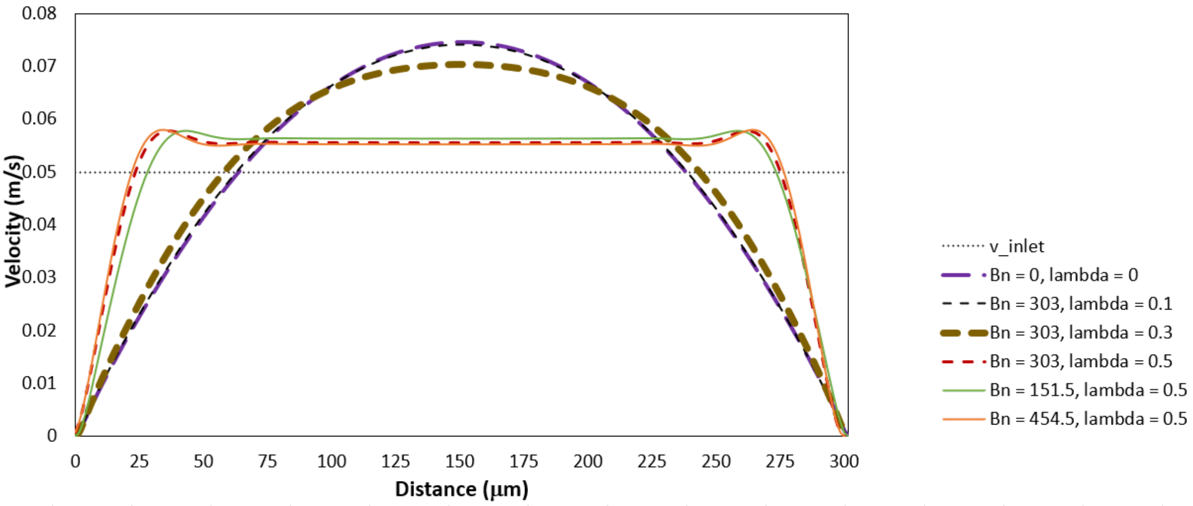

Figure 44. Velocity profiles measured in the middle of the 2D channel, with inlet velocity of 0.05 m/s

Implications for microscale model

In the Bingham LBM part of the microscale model, the choice of Bingham model parameters B_n and λ need to be high enough so that the Bingham fluid viscosity is sufficiently sensitive to shear rate to represent the flow of solid grains in liquid and reduce grain distortion. However, when higher Bingham and sensitivity parameters are used, there may be higher fluctuations in the velocity profile, especially in regions with higher shear rates, which can result in non-uniform macroscopic velocities in the solid phases.

It is shown that the velocity fluctuations can be reduced by increasing domain size, which will increase computation time, and reducing inlet velocity, which is not suitable for the purpose of the model. Therefore the combination of Bingham model parameters chosen needs to show sufficient shear rate dependency of the viscosity to be able distinguish between solid and liquid phases, and also reduce anomalous patterns in the velocity profile in regions with high shear rates.

8.2. Phase field-Potts model

8.2.1. Floating dendrite

The phase field-Potts model is applied to observe the growth of a single dendrite with different flow velocities, with the entire domain modelled as a Newtonian fluid in the fluid flow model. The domain has a resolution of 200 x 300, with a cell size of 1.50E-06 m. The timestep is 1.00E-07 s. The dendrite is grown from an initial nuclei with a radius of 5 cells. A normalised fluid velocity of 0.005 and 0.01 are used. The normalised fluid velocity u_n is defined as

$$u_n = U/(\frac{\Delta x}{\Delta t}) \tag{132}$$

where U is the fluid velocity, Δx is the cell size, and Δt is the timestep.

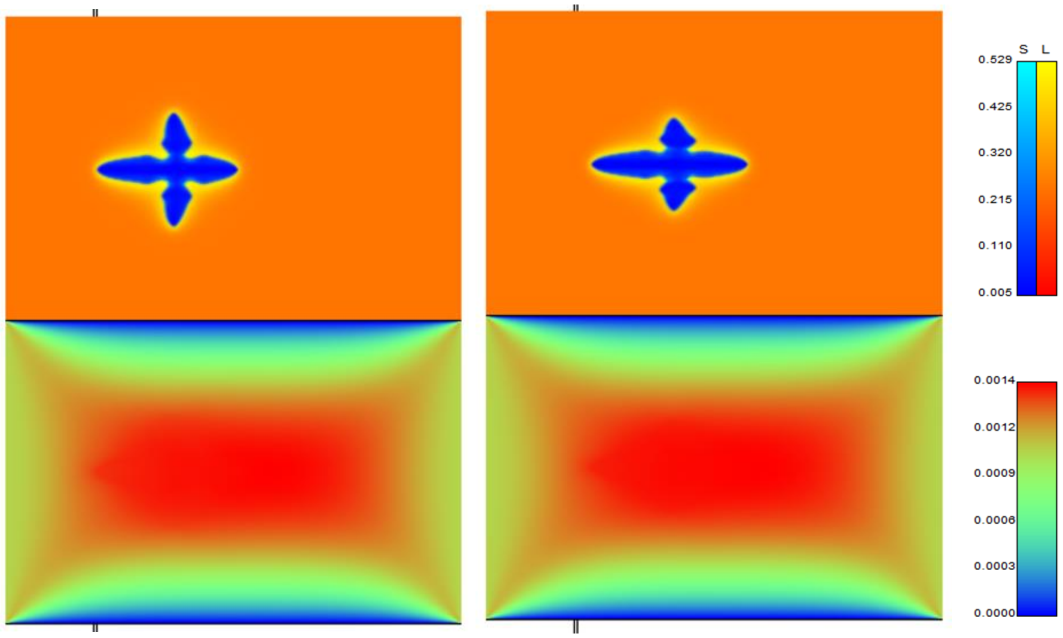

Figure 45. Concentration and velocity distributions of a floating dendrite in fluid flow from left to right of the domain, with a normalised fluid velocity of 0.005 (left) and 0.01 (right), captured after 10000 timesteps

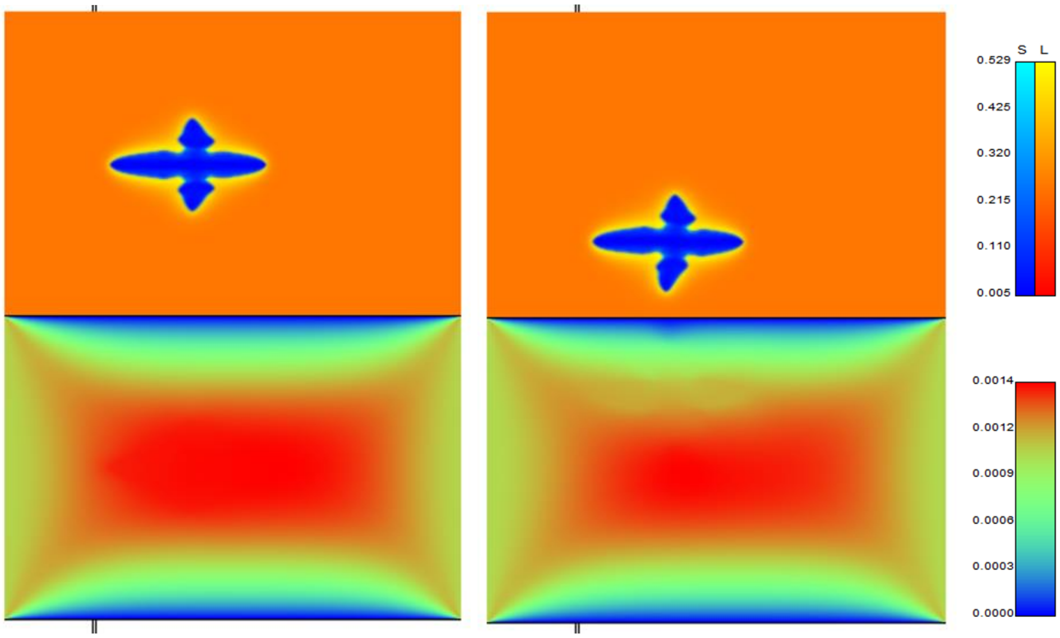

Figure 46. Concentration and velocity distributions of a floating dendrite in fluid flow from left to right of the domain, with a normalised fluid velocity of 0.01, with the nuclei starting in the middle of the channel (left) and near the wall (right), captured after 10000 timesteps

As shown in Figure 45, the modelled dendrite under fluid flow grows preferentially along the fluid flow direction. This effect becomes more significant as fluid velocity increases. Dendritic arms growing perpendicular to the flow direction are slightly distorted.

Figure 46 shows that if the initial nuclei is placed near the wall of the channel, a slight rotation of the dendrite can be observed, and more distortion of the dendrite arms is observed, compared to the case where the initial nuclei is in the middle of the channel. As the whole domain is modelled as a Newtonian fluid, there is no distinction between the velocity distributions in the solid phase and in the liquid phase, hence grain distortion is more severe near the wall of the channel, where the velocity gradient is higher.

It is shown that a continuous domain of Newtonian fluid is unsuitable for preserving the shape of the dendrite. The case is repeated with a velocity distribution dependent on the phase field, for a pinned dendrite.

8.2.2. Pinned dendrite

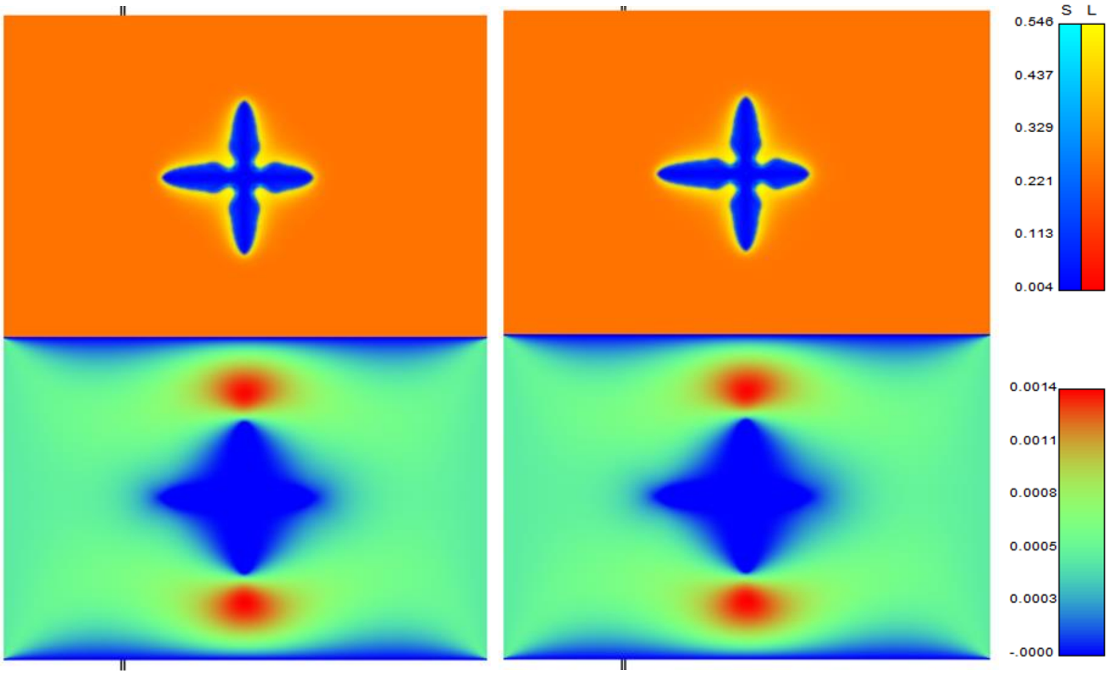

Figure 47. Concentration and velocity distributions of a pinned dendrite in fluid flow from left to right of the domain, with a normalised fluid velocity of 0.005 (left) and 0.01 (right), captured after 10000 timesteps

The growth of a pinned dendrite is modelled with the same model setup and input parameters as the floating dendrite example. To pin the dendrite, the macroscopic velocity of the solid phase is reset to zero during each iteration when calculating the equilibrium particle distribution in the LB model.

In the case of a pinned dendrite, there is less distortion and more growth in the dendritic arms perpendicular to the flow direction, compared to the floating dendrite. As shown in the velocity distributions in Figure 47, fluid near the dendritic arms perpendicular to flow direction has a higher relative velocity to the pinned dendrite, compared to the case with a floating dendrite, where there is no distinction between solid and liquid phase in the velocity distribution. The higher fluid velocity gradient aids the heat extraction from the solidification front, resulting in more growth in the dendritic arms within the same number of timesteps.

9. Multiscale model results and discussion

9.1. Multiscale model

The multiscale model is run for a case of AZ31 TRC, at a casting speed of 20 m/min, with no melt superheating.

9.1.1 Input from the macroscale model

The temperature distribution from the macroscale TRC model is used to generate thermal boundary conditions for the microscale model. The coupling between macroscale and microscale models is discussed in the example in chapter 6.2.1. The fitted coupling parameters can be found in Table **4**. The fitted temperature field found in Figure **23** is used as the initial temperature field.

TRC geometry based on the dimensions used in the macroscale model is applied to model the roll in the domain. The geometry parameters are listed in Table 11. An outlet velocity of 0.333 m/s is used, which is based on the casting speed used in the macroscale model (20 m/min). Velocity boundary conditions according to the casting speed are applied in the manners described in Chapter 6.

Table 11. Geometry parameters used to apply TRC dimensions

Outlet / inlet ratio	0.533
Roll radius / half-inlet ratio	33.333

9.1.2 Model set-up and material parameters

In the multiscale model, a domain size of 650 x 100 is used, with a cell size of 15 µm, and a timestep of 1 µs.

Nuclei are randomly generated at the inlet. The initial nuclei distribution is represented using a normal distribution for the particle radius. In this case, the size distribution has a mean and a standard deviation of 15 µm. The total volume fraction of the nuclei particles is 2%. The nuclei particles have randomised grain orientations.

A tertiary alloy system is used to represent AZ31 in the phase field-Potts model. The thermodynamic properties of the alloy components are listed in Table 12, with component A representing pure Mg, component B representing pure Al, and component C representing the remaining elements. The alloy concentrations of the liquid and the nuclei are given in Table 13, and the calculated thermodynamic properties are listed in Table 14. Interfacial and diffusion properties are listed in Table 15 - Table 17. LB fluid flow parameters are listed in Table 18.

Table 12. Thermodynamic properties of the tertiary alloy system

	Component A	Component B	Component C
Melting temperature (K)	923	933.47	1000
Latent heat (MJ/m^3)	622	1071	1000
Heat capacity (MJ/K/m^3)	1.77	2.44	2.5

Table 13. Alloy concentrations

	Component B (wt.%)	Component C (wt.%)
Liquid	2.7	0
Nuclei particles	1	0.03

Table 14. Calculated thermodynamic properties of the tertiary alloy system

Liquidus temperature (K)	903.9
Solidus temperature (K)	869.3
Gibbs-Thomson coefficient (K.m)	0.148E-2

Table 15. Interfacial properties

Interface thickness (delta/dx)	0.667
Cell size dx (µm)	15
Energy (nominal) (J/m^2)	0.05
Energy anisotropy	0.05

Mobility (m/s/K)	0.001
Mobility anisotropy	0
Grain boundary thickness (delta/dx)	0.667

Table 16. Diffusion properties

Heat diffusivity in liquid (mm^2/s)	90
Heat diffusivity in solid (mm^2/s)	90
Molecular volume (ml/mol)	14

Table 17. Solute diffusivities

	Diffusion prefactor D_0 (mm^2/s)	Activation energy (J/mol)
B-solute diffusivity in liquid	4E-3	0
B-solute diffusivity in solid	4E-6	0
C-solute mobility	5E-19	

Table 18. LB fluid flow parameters

Kinematic viscosity (m^2/s)	2.25E-4
Dynamic viscosity (Pa.s)	2.25E-4
Yield stress (Pa)	1.35
Strain rate coefficient (s)	1E-4
LB relaxation parameter	2.857E-1

9.2. Effects of Bingham LBM model parameters

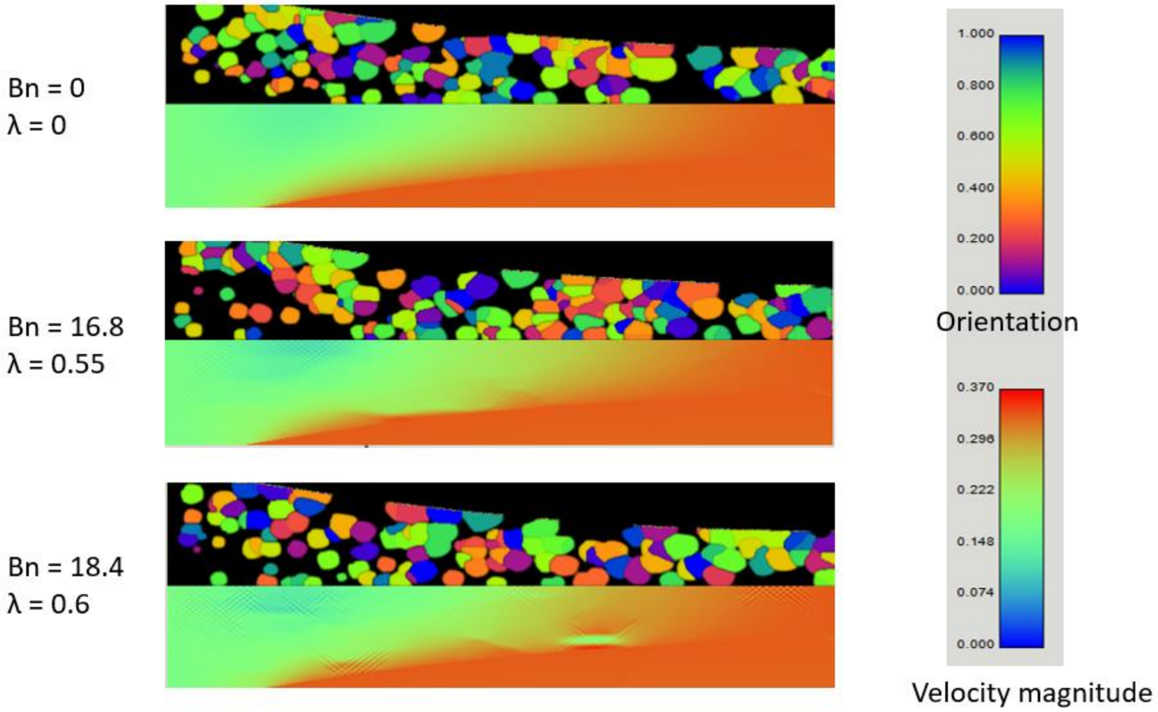

Figure 48. Orientation and velocity distributions using different Bingham LB model parameters, after 1000 timesteps. Velocity is measured in m/s.

By comparing the velocity distributions obtained via different model parameters in Figure **48**, it is shown that by modelling the melt as a Bingham fluid, the effects of solid movement in fluid flow on the velocity distribution can be represented. For example, regions near the roll surface have the same velocity as the roll, as grains are attached to the roll surface and move at the same speed as the roll. Meanwhile, grains near the inlet, which are suspended in the melt, can move freely and have the same velocity as the surrounding liquid.

As shown in the bottom graph in Figure **48**, there is a volume of liquid near the roll surface which has the same velocity as the liquid near the inlet, instead of moving at the same speed as the roll surface as shown in the example with Newtonian fluid LBM. This results from the volume being connected to the melt and suspended grains. If instead, the volume is trapped in a cluster of grains with formed grain boundaries and attached to the roll surface, as shown by the volume of liquid near the exit, the fluid moves at the same velocity as the surrounding grains.

Although the model shows more differentiation between solid and liquid velocity distribution by increasing the Bingham and sensitivity parameters, fluctuations in the velocity profile in regions with high shear will be amplified as Bingham and sensitivity parameters increase, as shown in the results in Chapter 8.1, which can lead to grain distortion due to non-uniform velocity distribution.

There needs to be a compromise between the Bingham fluid properties and the stability of the velocity profile. This can be achieved by calibration of the Bingham and sensitivity parameters via comparisons between modelled and experimental as-cast microstructure in future studies.

9.3. Effects of surface nucleation

The same model is run under the conditions where nucleation only occurs on the roll surface or in the melt. It is shown that an increased nuclei density distribution within the melt results in the formation of equiaxed grains and a uniform texture, leading to improved mechanical properties, while an emphasis on nucleation on roll surface leads to the formation of columnar grains and an increase in grain size, which results in undesirable mechanical properties of the as-cast microstructure.

In Figure 49, intergranular cracks can be observed in the columnar grains, starting from near the roll surface, and extended to the centreline region as the sheet reaches the exit. As the microscale model does not carry out stress analysis, the cracks could be an artefact due to the implementation method of velocity boundary conditions at the roll surface and the exit.

In experiments, nucleation at the roll surface cannot be avoided. Therefore, to reduce formation of columnar grains, nuclei density within the melt needs to be increased in order to compete with nucleation at the roll surface, via pre-processing procedures such as melt shearing or grain refiner additions.

Experimental data is required to calibrate the nuclei size distribution in the melt. The multiscale model can be used to determine the critical nuclei density required in the melt to achieve an equiaxed microstructure under the selected casting conditions.

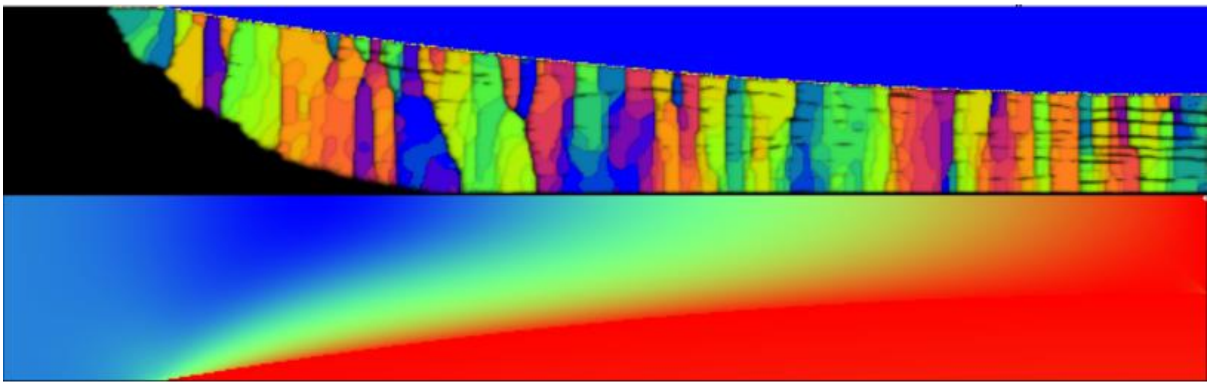

Figure 49. Orientation distribution with only roll surface nucleation

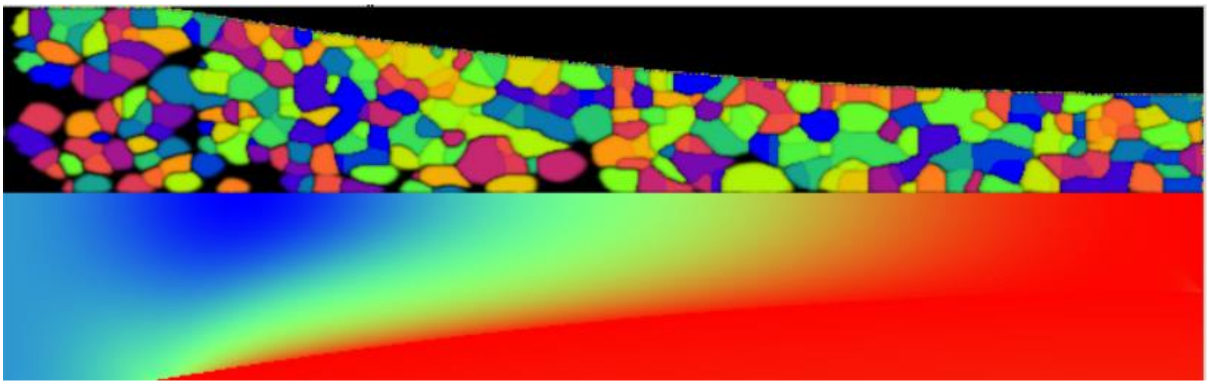

Figure 50. Orientation distribution with no roll surface nucleation

10. Experimental verification

In order to assess the accuracy and validity of the proposed model, experimental results of TRC of different alloys under a range of process conditions are analysed and compared with the modelled results obtained with the same set up.

10.1. Verification of macroscale model

As the macroscale model is used to provide the temperature profile of the strip as an input for the microscale model, the modelled temperature profile should be verified experimentally.

A database of experimental results of pure Al TRC were used to predict equations describing the casting capacity and solidus position from bite. The input parameters include target strip thickness, roll diameter, setback distance, roll speed, inlet temperature, and material properties including specific heat capacity, latent heat of solidification, liquidus temperature, and solidus temperature. Figure 51 shows the solidus position calculated at different casting speeds using the same roll diameter, strip thickness, setback distance and inlet temperature as the macroscale model. The solidus position from bite decreases linearly with casting speed. At a casting speed of 2 m/min, the predicted solidus position is 17 mm from the bite position.

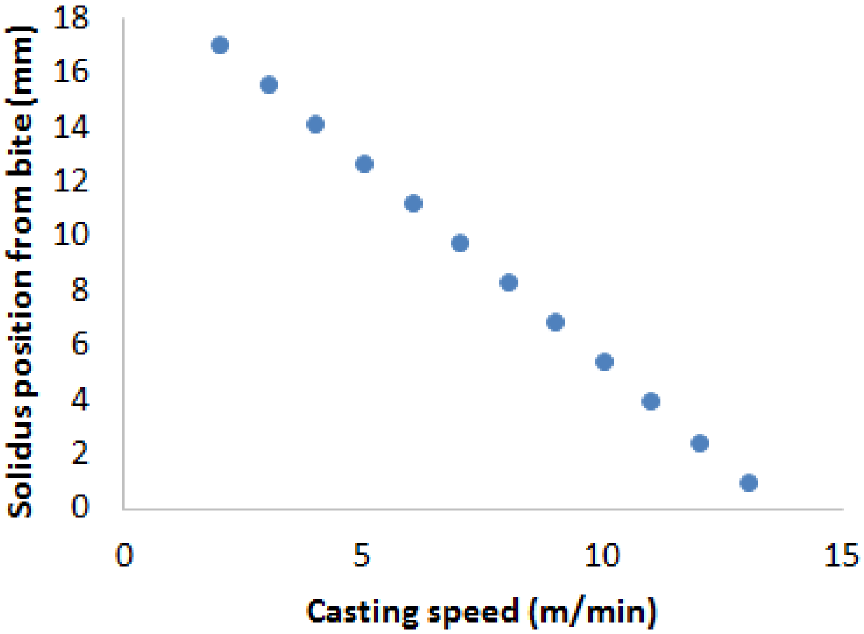

Figure 51. Experimental data of pure Al TRC, from P Thomas et al. [92]

With the same casting speed of 2 m/min, Figure 52 shows the changes in solidus position with time for pure Al TRC, modelled with different thermal conductance values at the roll-strip interface. As time increases, the change in solidus position slows down and steady state is reached at 2 s. As the roll-strip interface conductance increases, the solidus position moves away from bite, and the changes stagnate as the interface conductance reaches 600000 W/(m·K). As the model reaches steady state, the solidus position from bite is 14.5 mm, which is 15% smaller than the 17 mm predicted using experimental TRC data, indicating a slightly lower rate of heat transfer in the modelled Al TRC, compared to experiment.

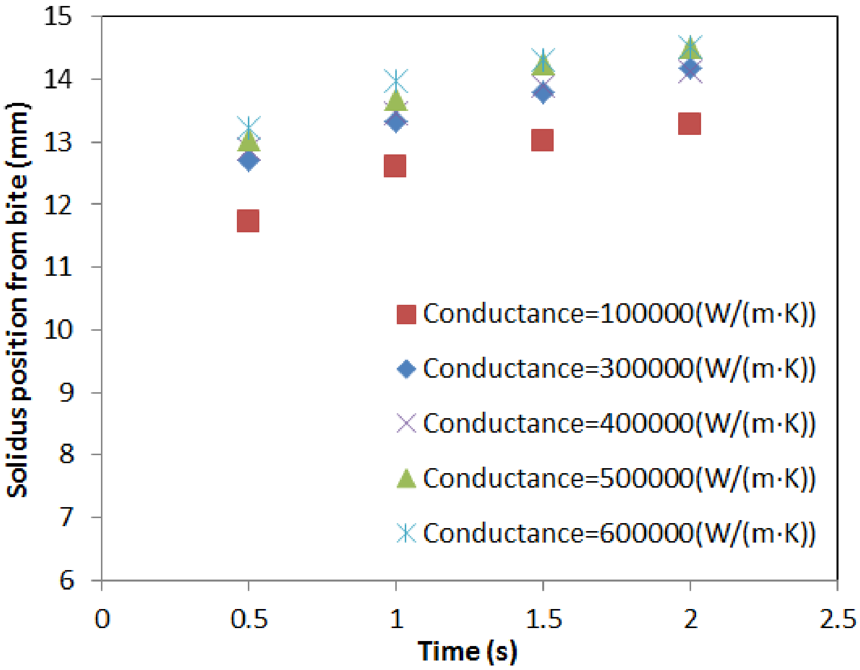

Figure 52. Modelled solidus position vs time for pure Al TRC with a casting speed of 2 m/min

A possible limitation of this verification method is that the ‘experimental data’ is calculated from an empirical model generated from Al TRC experiments under a range of conditions. The empirical model cannot consider all the details of an experiment, and it may not be able to accurately represent scenarios outside the process conditions used for the input data.

Therefore, additional TRC experiments with specified process conditions should be used to further assess the validity of the macroscale model.

TRC experiments of pure Mg were performed with strip thickness of 1.6 mm, roll diameter of 100 mm, and casting speed of 10 m/min. As shown in Figure 53, a contact thermometer was held on the strip surface and travelled on the moving strip, maintaining a fixed distance (150 mm) to the exit. The measured temperature is used to deduce the strip surface temperature at the exit considering heat transfer due to convection, assuming negligible effects of conduction along the strip. The surface temperature measured is 364.9 ± 4.5 ^{o}C, and the calculated surface temperature at exit is 367.3 ± 4.5 ^{o}C.

The macroscale model with the same material and process parameters gives an exit surface temperature of 355.9 ± 3.1 ^{o}C in steady state. As shown in Figure 54, the exit surface temperature obtained from experiment is 3% higher than the modelled value, signifying a similar rate of heat transfer in experiment and model.

A possible limitation of this verification method is the uncertainties in experiments. For example, during the experiments, liquid metal is continuously being poured into the tundish as the strip is rolled out, which may cause fluctuations in liquid pressure and melt temperature.

Another source of inaccuracy is errors in temperature measurement. An oxide layer is formed on the strip surface when Mg is exposed to air. MgO has a much lower thermal conductivity compared to pure Mg, which can cause the measured temperature to be lower than the actual surface temperature of a Mg strip without oxide. At a high casting speed, the strip exiting the rolls has a higher surface temperature, which can cause resistance in moving the contact thermometer and measuring errors, as it tends to stick to the strip surface.

Furthermore, edge effect might also affect the validity of experimental data. The macroscale model assumes negligible edge effect. The steel rolls used in the experiments have a length of 156 mm, which limits the width of strips being produced. Inconsistencies in liquid metal pouring result in varying strip width. As the strip width decreases, heat transfer in the transverse direction has a more significant effect on strip cooling, causing the measured temperature to be lower than the expected value.

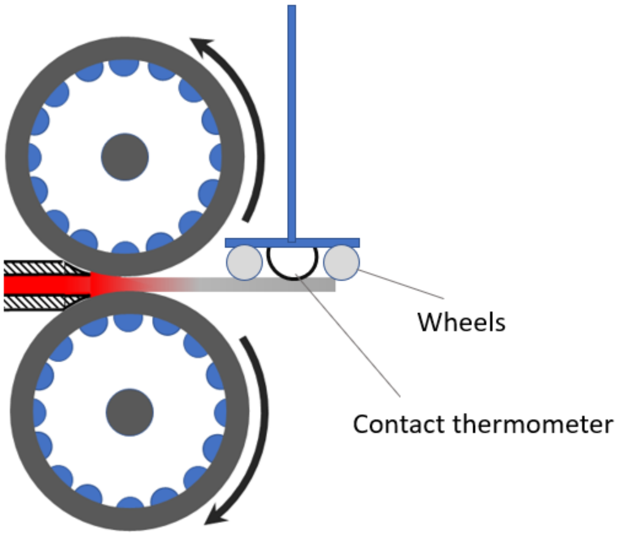

Figure 53. Experimental set up for Mg TRC

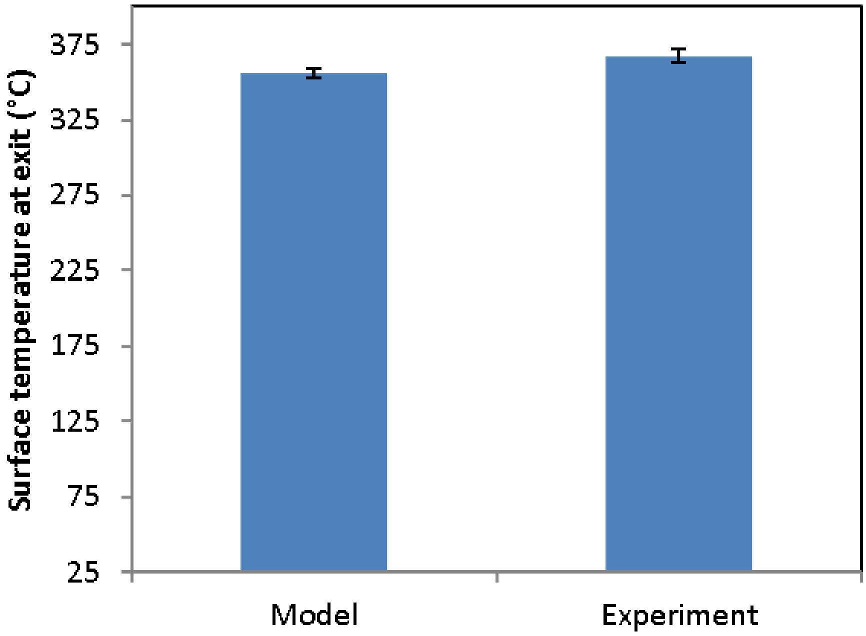

Figure 54. Comparison between modelled and experimentally obtained exit surface temperatures for pure Mg TRC

11. Impact on TRC manufacturing practices

The main function of the proposed multiscale model is to predict behaviour in high speed TRC processes, under the assumption that the process is mainly solidification, and deformation has minimal effects on the as-cast microstructure, with the ideal result being that the solidification zone along the centreline ends exactly at the exit, as depicted in Figure 35.

11.1 Macroscale model

The macroscale thermal-mechanical model can be used to analyse the temperature and stress distributions in the alloy strip for different casting and material parameters. The macroscale model findings show that further decrease of roll surface temperature below room temperature has negligible effect on the temperature profile of the alloy strip, which can be used to inform manufacturing decisions.

The proposed quasi-1D solidification model can be used to give a theoretical upperbound casting speed for selected TRC geometries and metal parameters, at which the solidification zone ends at the exit of the rolls. However, the calculated maximum casting speed cannot be achieved in reality, due to imperfect thermal contact between the metal and the roll causing reduced heat transfer, and inefficient cooling within the rolls causing the roll surface temperature to continue to increase above room temperature throughout the process.

The macroscale model can be used to determine a realistic upperbound casting speed for a chosen alloy composition and strip thickness.

11.2 Microscale model

The microscale model does not carry out stress calculations to analyse grain deformation, therefore it is unsuitable for modelling low speed TRC, in which the deformation process has a large impact on the ac-cast microstructure.

In order to reduce columnar grain formation, in the manufacturing process, grain refiners can be added to increase the number of nucleation sites in the melt and to overcome surface nucleation. Melt conditioning can also be used to disperse native oxides which can act as nucleation sites. The nuclei size distribution used in the microscale model can be varied to study the effects on columnar grain formation. The goal is to determine the critical nuclei density required in the melt to obtain an equiaxed microstructure under certain casting conditions.

Further calibrations of modelling parameters can be done by comparing the texture and grain size distribution of the as-cast microstructure from experiment, to those of the modelled as-cast microstructure obtained under the same casting conditions and using experimentally measured nuclei size distribution in the melt as an input.

When the multiscale model is fully developed, it can be used to determine the casting conditions and melt pre-processing conditions required to achieve the desired as-cast microstructure for specific alloys, which can help make the TRC process more energy efficient by reducing the need for subsequent machining and heat treatments of the strips to improve their mechanical properties.

12. Summary

A multiscale model of twin roll casting has been developed to study the effects of various casting conditions on the developments of temperature profile and microstructure during solidification. It consists of a macroscale thermal-mechanical model and a microscale solidification and fluid flow model, coupled through using the macroscale temperature profile of the strip as the thermal boundary condition for the microscale model.

The macroscale model shows that as casting speed increases, the solidification front is moved closer to the exit, and the exit centreline and surface temperatures increase at different rates with the casting speed. It is found that the roll temperature has a negligible effect on the strip temperature profile, which can be explained via a quasi-1D solidification model of TRC. The theoretical upper bound casting speed calculated to be inversely proportional to the square of strip thickness. To validate the model, experimental data from Al and Mg TRC is compared with results of the macroscale model under the same casting conditions.

The microscale model simulates the evolution of microstructure in solidification via a phase field-Potts model, and fluid flow is simulated via a Bingham LB model. The effect of solid motion in liquid is represented by increasing the sensitivity of viscosity to shear rate in the Bingham LB model. Simulations of 2D channel flows of Bingham fluid are carried out to study the effects of Bingham and sensitivity parameters on the velocity profiles.

Coupling of the microscale and macroscale models occurs via the application of thermal and velocity boundary conditions and the macroscale geometries. The multiscale model is run for a case of AZ31 TRC, and the effects of Bingham LB model parameters and surface nucleation on the as-cast microstructure are studied.

In summary, the proposed TRC model is developed to simulate the as-cast microstructures of high speed TRC, in order to reduce defect formation and improve the mechanical properties of the casted alloy sheets. The modelling results allows comparisons of grain growth and texture development during TRC with various casting conditions, which can help the selection of casting conditions, specifically to reduce columnar grain growth and macrosegregation for different alloy compositions.

13. Further developments

The proposed multiscale model aims to simulate the as-cast microstructure of high speed TRC, which minimises deformation in strip, in order to reduce casting defects. Stress analysis is not incorporated into the microscale solidification model. During low speed TRC, deformation of the strip causes flow of liquid in the mushy zone, and the movement of solutes out of interdendritic volume, leading to centreline segregation. A deformation model can be coupled to the microscale model to take into account the stress distribution resulted from the casting conditions.

The spring back effect, where the strip thickness changes after the strip has been released from the rolls, causing the casted thickness to be greater than the roll gap, is also observed in TRC experiments. Further investigations of the macroscale deformation model can be used to determine conditions which help reduce the spring back effect.

As a result of the spring back effect, a different method of including air convection at strip surface may need to be implemented. In the proposed air cooling model, the heat transfer coefficient between the strip surface and the artificial ‘air’ surface is assumed to be a function of distance. This model will become unreliable when the strip expands after exiting the rolls.

In addition, a post-processing module can be added to the microscale model, collecting the alloy concentration and grain orientation data of the single layer of cells at the bite position in each time step, as shown in Figure 55. The modelled as-cast microstructure can be generated by compiling the recorded alloy concentration and grain orientation data of the cells at the exit in order of time. More experimentally obtained as-cast microstructures and texture data are required to verify the multiscale model.

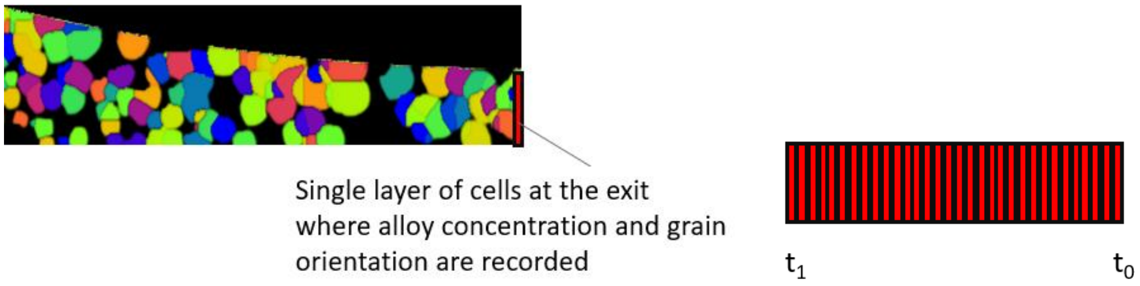

Figure 55. Schematics indicating cells used to generate the as-cast microstructure

Furthermore, to improve coupling of the macroscale and microscale models, the temperature distribution from the microscale model can be fitted back to the macroscale model. The macroscale model is run again with the new initial strip temperature profile. After steady state is reached, the strip temperature profile is used to give the thermal boundary conditions for the microscale model. This process can be repeated for several iterations, to reduce errors in fitting the macroscale strip temperature profile to the temperature function used as the thermal boundary condition of the microscale model, thus improve coupling of the models.

References

[1] SS Park, W- Park, CH Kim, BS You, NJ Kim. The twin-roll casting of magnesium alloys, JOM. 61 (2009) 14.

[2] GT Bae, JH Bae, DH Kang, H Lee, NJ Kim. Effect of Ca addition on microstructure of twin-roll cast AZ31 Mg alloy, Metals and Materials International. 15 (2009) 1-5.

[3] A Hadadzadeh, MA Wells. Inverse and centreline segregation formation in twin roll cast AZ31 magnesium alloy, Materials Science and Technology. 31 (2015) 1715-1726.

[4] S Das, NS Barekar, O El Fakir, L Wang, AK Prasada Rao, JB Patel, et al. Effect of melt conditioning on heat treatment and mechanical properties of AZ31 alloy strips produced by twin roll casting, Materials Science and Engineering: A. 620 (2015) 223-232.

[5] Y Huang, I Bayandorian, Z Fan. Microstructure control during twin roll casting of an AZ31 magnesium alloy, IOP Conference Series: Materials Science and Engineering. 27 (2012) 012065.

[6] S Chen, J Chen, J Yu, L Lv. Simulation of microstructures in solidification of aluminum twin-roll continuous casting, Procedia Engineering. 31 (2012) 509-514.

[7] C Shoudong, C Jingchao. Micromodel of Simulation on Twin-Roll Continuous Casting Thin Strip Solidification Structure, Rare Metal Materials and Engineering. 42 (2013) 14-18.

[8] M Rappaz, C- Gandin, Probabilistic modelling of microstructure formation in solidification processes, Acta Metallurgica et Materialia. 41 (1993) 345-360.

[9] J Zeng, R Koitzsch, H Pfeifer, B Friedrich. Numerical simulation of the twin-roll casting process of magnesium alloy strip, J.Mater.Process.Technol. 209 (2009) 2321-2328.

[10] H Zhao, P Li, L He. Coupled analysis of temperature and flow during twin-roll casting of magnesium alloy strip, J.Mater.Process.Technol. 211 (2011) 1197-1202.

[11] H Hu. Grain refinement of Mg-Al alloys by optimization of process parameters based on three-dimensional finite element modeling of roll casting, Transactions of Nonferrous Metals Society of China. 23 (2013) 773-780.

[12] Y He, A Javaid, E Essadiqi, M Shehata. Numerical Simulation and Experimental Study of the Solidification of a Wedge-Shaped Az31 mg Alloy Casting, Can.Metall.Q. 48 (2009) 145-155.

[13] A Hadadzadeh, M Wells, E Essadiqi. Mathematical Modeling of the Twin Roll Casting Process for Az31 Magnesium Alloy - Effect of Set-Back Distance, Magnesium Technology 2012. (2012) 141-144.

[14] T SAITOH, H HOJO, H YAGUCHI, C KANG. Two-Dimensional Model for Twin-Roll Continuous-Casting, Metallurgical Transactions B-Process Metallurgy. 20 (1989) 381-390.

[15] S HWANG, Y KANG. Analysis of Flow and Heat-Transfer in Twin-Roll Strip Casting by Finite-Element Method, Journal of Engineering for Industry-Transactions of the Asme. 117 (1995) 304-315.

[16] VE Badalassi, HD Ceniceros, S Banerjee, Computation of multiphase systems with phase field models, Journal of Computational Physics. 190 (2003) 371-397.

[17] C Liu, J Shen, A phase field model for the mixture of two incompressible fluids and its approximation by a Fourier-spectral method, Physica D: Nonlinear Phenomena. 179 (2003) 211-228.

[18] GE Karniadakis, M Israeli, SA Orszag, High-order splitting methods for the incompressible Navier-Stokes equations, Journal of Computational Physics. 97 (1991) 414-443.

[19] J Kim, J Lowengrub. Phase field modeling and simulation of three-phase flows, Interface Free Bound. 7 (2005) 435-466.

[20] FP Mariano, LQ Moreira, A Silveira-Neto, CB da Silva, JCF Pereira. A new incompressible Navier-Stokes solver combining Fourier pseudo-spectral and immersed boundary methods, CMES-Comp.Model.Eng.Sci. 59 (2010) 181-216.

[21] FJ Higuera, S Succi, R Benzi. Lattice Gas Dynamics with Enhanced Collisions, EPL (Europhysics Letters). 9 (1989) 345.

[22] S S., Y J.M. The Lattice Boltzmann Equation for Fluid Dynamics and Beyond, Phys Today. 55 (2002) 58-60.

[23] AJ Wagner, A Practical Introduction to the Lattice Boltzmann Method, Adt. notes for Statistical Mechanics 463/663 at NDSU, (2008).

[24] Q Li, KH Luo, QJ Kang, YL He, Q Chen, Q Liu. Lattice Boltzmann methods for multiphase flow and phase-change heat transfer, Progress in Energy and Combustion Science. 52 (2016) 62-105.

[25] S Chen, G Doolen. Lattice Boltzmann method for fluid flows, Annu.Rev.Fluid Mech. 30 (1998) 329-364.

[26] AK Gunstensen, DH Rothman, S Zaleski, G Zanetti. Lattice Boltzmann model of immiscible fluids, Phys.Rev., A. 43 (1991) 4320-4327.

[27] T Reis, TN Phillips. Lattice Boltzmann model for simulating immiscible two-phase flows, Journal of Physics A: Mathematical and Theoretical. 40 (2007) 4033.

[28] D Grunau, S Chen, K Eggert. A lattice Boltzmann model for multiphase fluid flows, Physics of Fluids A: Fluid Dynamics. 5 (1993) 2557-2562.

[29] J Tolke, X Krafczyk, M Schulz, E Rank. Lattice Boltzmann simulations of binary fluid flow through porous media, PHILOSOPHICAL TRANSACTIONS OF THE ROYAL SOCIETY OF LONDON SERIES A-MATHEMATICAL PHYSICAL AND ENGINEERING SCIENCES}. 360} (2002}) 535-545}.

[30] M Latva-Kokko, DH Rothman. Diffusion properties of gradient-based lattice Boltzmann models of immiscible fluids, Phys Rev E. 71 (2005) 056702.

[31] S Leclaire, M Reggio, J Trepanier. Numerical evaluation of two recoloring operators for an immiscible two-phase flow lattice Boltzmann model, APPLIED MATHEMATICAL MODELLING}. 36} (2012}) 2237-2252}.

[32] CM Pooley, H Kusumaatmaja, JM Yeomans. Contact line dynamics in binary lattice Boltzmann simulations, Phys Rev E. 78 (2008) 056709.

[33] C Zhang, Y Cheng, S Huang, J Wu. Improving the Stability of theMultiple-Relaxation-Time Lattice Boltzmann Method by a Viscosity Counteracting Approach, Advances in Applied Mathematics and Mechanics. 8 (2016) 37-51.

[34] JM Buick, CA Greated. Gravity in a lattice Boltzmann model, Phys Rev E. 61 (2000) 5307-5320.

[35] Z Fan, Y Zhao, A Kaufman, Y He, Adapted Unstructured LBM for Flow Simulation on Curved Surfaces, (2005).

[36] S Ubertini, G Bella, S Succi. Lattice Boltzmann method on unstructured grids: Further developments, Phys Rev E. 68 (2003) 016701.

[37] AJC Ladd. Numerical simulations of particulate suspensions via a discretized Boltzmann equation. Part 1. Theoretical foundation, J.Fluid Mech. 271 (1994) 285-309.

[38] RW Nash, HB Carver, MO Bernabeu, J Hetherington, D Groen, T Krueger, et al. Choice of boundary condition for lattice-Boltzmann simulation of moderate-Reynolds-number flow in complex domains, Phys Rev E. 89 (2014) 023303.

[39] H Liu, JG Zhou, R Burrows. Inlet and outlet boundary conditions for the Lattice-Boltzmann modelling of shallow water flows, Prog.Comput.Fluid Dyn. 12 (2012) 11-18.

[40] Q Zou, X He. On pressure and velocity boundary conditions for the lattice Boltzmann BGK model, Phys.Fluids. 9 (1997) 1591-1598.

[41] S Ubertini, S Succi. Recent advances of Lattice Boltzmann techniques on unstructured grids, Prog.Comput.Fluid Dyn. 5 (2005) 85-96.

[42] N Rossi, S Ubertini, G Bella, S Succi. Unstructured lattice Boltzmann method in three dimensions, Int.J.Numer.Methods Fluids. 49 (2005) 619-633.

[43] W Li, L Luo. Finite Volume Lattice Boltzmann Method for Nearly Incompressible Flows on Arbitrary Unstructured Meshes, Commun.Comput.Phys. 20 (2016) 301-324.

[44] S Ubertini, S Succi. A generalised Lattice Boltzmann equation on unstructured grids, Communications in Computational Physics. 3 (2008) 342-356.

[45] MK Misztal, A Hernandez-Garcia, R Matin, HO Sørensen, J Mathiesen, Detailed analysis of the lattice Boltzmann method on unstructured grids, Journal of Computational Physics. 297 (2015) 316-339.

[46] DO MartÃnez, WH Matthaeus, S Chen, DC Montgomery. Comparison of spectral method and lattice Boltzmann simulations of two-dimensional hydrodynamics, Phys.Fluids. 6 (1994) 1285-1298.

[47] S Succi. Lattice Boltzmann 2038, EPL (Europhysics Letters). 109 (2015) 50001.

[48] RS Qin, HK Bhadeshia. Phase field method, Mater.Sci.Technol. 26 (2010) 803-811.

[49] R Kobayashi, Modeling and numerical simulations of dendritic crystal growth, Physica D: Nonlinear Phenomena. 63 (1993) 410-423.

[50] M Yamaguchi, C Beckermann, Simulation of solid deformation during solidification: Compression of a single dendrite, Acta Materialia. 61 (2013) 4053-4065.

[51] F Gibou, RP Fedkiw, L Cheng, M Kang, A Second-Order-Accurate Symmetric Discretization of the Poisson Equation on Irregular Domains, Journal of Computational Physics. 176 (2002) 205-227.

[52] JA Warren, R Kobayashi, AE Lobkovsky, W Craig Carter, Extending phase field models of solidification to polycrystalline materials, Acta Materialia. 51 (2003) 6035-6058.

[53] M Yamaguchi, C Beckermann, Simulation of solid deformation during solidification: Shearing and compression of polycrystalline structures, Acta Materialia. 61 (2013) 2268-2280.

[54] S Subedi, R Pokharel, AD Rollett. Orientation gradients in relation to grain boundaries at varying strain level and spatial resolution, Materials Science and Engineering: A. 638 (2015) 348-356.

[55] JJ Huang, C Shu, JJ Feng, YT Chew. A Phase-Field-Based Hybrid Lattice-Boltzmann Finite-Volume Method and Its Application to Simulate Droplet Motion under Electrowetting Control, J.Adhes.Sci.Technol. 26 (2012) 1825-1851.

[56] J Kim, K Kang. A numerical method for the ternary Cahn-Hilliard system with a degenerate mobility, Applied Numerical Mathematics. 59 (2009) 1029-1042.

[57] D Furihata. A stable and conservative finite difference scheme for the Cahn-Hilliard equation, Numerische Mathematik. 87 (2001) 675-699.

[58] J Blowey, M Copetti, C Elliott. Numerical analysis of a model for phase separation of a multi-component alloy, Ima Journal of Numerical Analysis. 16 (1996) 111-139.

[59] J Barrett, J Blowey, H Garcke. Finite element approximation of the Cahn-Hilliard equation with degenerate mobility, Siam Journal on Numerical Analysis. 37 (1999) 286-318.

[60] HD Ceniceros, RL N\'os, AM Roma. Three-dimensional, Fully Adaptive Simulations of Phase-field Fluid Models, J.Comput.Phys. 229 (2010) 6135-6155.

[61] J Kim. Phase-Field Models for Multi-Component Fluid Flows, Communications in Computational Physics. 12 (2012) 613-661.

[62] G Soderlind, L Wang. Adaptive time-stepping and computational stability, J.Comput.Appl.Math. 185 (2006) 225-243.

[63] Y He, Y Liu. Stability and Convergence of the Spectral Galerkin Method for the Cahn-Hilliard Equation, Numerical Methods for Partial Differential Equations. 24 (2008) 1485-1500.

[64] P Howard. Spectral analysis of planar transition fronts for the Cahn-Hilliard equation, Journal of Differential Equations. 245 (2008) 594-615.

[65] X Ye. The Fourier collocation method for the Cahn-Hilliard equation, Comput.Math.Appl. 44 (2002) 213-229.

[66] X Ye, X Cheng. The Fourier spectral method for the Cahn-Hilliard equation, Applied Mathematics and Computation. 171 (2005) 345-357.

[67] S Chai, Y Zou. The Spectral Method for the Cahn-Hilliard Equation with Concentration-Dependent Mobility, J.Appl.Math. (2012) 808216.

[68] J Zhu, L Chen, J Shen, V Tikare. Coarsening kinetics from a variable-mobility Cahn-Hilliard equation: Application of a semi-implicit Fourier spectral method, Phys Rev E. 60 (1999) 3564-3572.

[69] JS Langer, M Bar-on, HD Miller. New computational method in the theory of spinodal decomposition, Phys.Rev., A. 11 (1975) 1417-1429.

[70] K Kitahara, M Imada. On the Kinetic Equations for Binary Mixtures*), Progress of Theoretical Physics Supplement. 64 (1978) 65-73.

[71] HW Zheng, C Shu, YT Chew, A lattice Boltzmann model for multiphase flows with large density ratio, Journal of Computational Physics. 218 (2006) 353-371.

[72] T Lee, L Liu, Lattice Boltzmann simulations of micron-scale drop impact on dry surfaces, Journal of Computational Physics. 229 (2010) 8045-8063.

[73] L Zheng, S Zheng, Q Zhai. Lattice Boltzmann equation method for the Cahn-Hilliard equation, Physical Review E. 91 (2015) 013309.

[74] L Chen, J Shen. Applications of semi-implicit Fourier-spectral method to phase field equations, Comput.Phys.Commun. 108 (1998) 147-158.

[75] H Fu, C Liu. A Buffered Fourier Spectral Method for Non-Periodic Pde, Int.J.Numer.Anal.Model. 9 (2012) 460-478.

[76] K Langaas, J Yeomans. Lattice Boltzmann simulation of a binary fluid with different phase viscosities and its application to fingering in two dimensions, European Physical Journal B. 15 (2000) 133-141.

[77] H Huang, L Wang, X Lu, Evaluation of three lattice Boltzmann models for multiphase flows in porous media, Computers & Mathematics with Applications. 61 (2011) 3606-3617.

[78] R Rojas, T Takaki, M Ohno, A phase-field-lattice Boltzmann method for modeling motion and growth of a dendrite for binary alloy solidification in the presence of melt convection, Journal of Computational Physics. 298 (2015) 29-40.

[79] P Joly, R Mehrabian. The rheology of a partially solid alloy, J.Mater.Sci. 11 (1976) 1393-1418.

[80] F MOORE. The rheology of ceramic slip and bodies, Trans.Brit.Ceram.Soc. 58 (1959) 470-492.

[81] M Modigell, J Koke. Rheological modelling on semi-solid metal alloys and simulation of thixocasting processes, J.Mater.Process.Technol. 111 (2001) 53-58.

[82] Z Fan, JY Chen. Modelling of rheological behaviour of semisolid metal slurries Part 2 – Steady state behaviour, 18 (2002) 243-249.

[83] A Hadadzadeh, MA Wells. Mathematical modeling of thermo-mechanical behavior of strip during twin roll casting of an AZ31 magnesium alloy, Journal of Magnesium and Alloys. 1 (2013) 101-114.

[84] J Park. Numerical analyses of cladding processes by twin-roll casting: Mg-AZ31 with aluminum alloys, Int.J.Heat Mass Transfer. 93 (2016) 491-499.

[85] S Lee, HJ Ham, SY Kwon, SW Kim, CM Suh. Thermal Conductivity of Magnesium Alloys in the Temperature Range from −125 °C to 400 °C, Int.J.Thermophys. 34 (2013) 2343-2350.

[86] AZoMaterials, H13 Tool Steel Material Properties Database, 2017.

[87] GH Tang, SB Wang, PX Ye, WQ Tao, Bingham fluid simulation with the incompressible lattice Boltzmann model, Journal of Non-Newtonian Fluid Mechanics. 166 (2011) 145-151.

[88] X He, L Luo. Lattice Boltzmann Model for the Incompressible Navier–Stokes Equation, Journal of Statistical Physics. 88 (1997) 927-944.

[89] TC Papanastasiou. Flows of Materials with Yield, J.Rheol. 31 (1987) 385-404.

[90] C Wang, J Ho, Lattice Boltzmann modeling of Bingham plastics, Physica A: Statistical Mechanics and its Applications. 387 (2008) 4740-4748.

[91] H Assadi, M Oghabi, DM Herlach. Influence of ordering kinetics on dendritic growth morphology, Acta Materialia. 57 (2009) 1639-1647.

[92] P Thomas, Experimental data of pure Al TRC, Personal communication (2017).

Appendix 1. Material properties used in the macroscale model

1.1. Mg material *properties*

Table 19. Thermal conductivity of Mg as a function of temperature

Thermal conductivity (S/m)	Temperature (°C)
83.9	50
87.3	100
97	200
101.8	250
118.5	424
60	630
120	635
240	680

Table 20. Young’s modulus of Mg as a function of temperature

Young’s modulus (Pa)	Poisson ratio	Temperature (°C)
4.50E+10	0.33	27
4.30E+10	0.33	102
4.10E+10	0.33	202
3.80E+10	0.33	297
3.70E+10	0.33	342
3.55E+10	0.33	397
3.45E+10	0.33	424
1.50E+10	0.33	578
1.00E+09	0.33	608

Table 21. Thermal expansion coefficient of Mg as a function of temperature

Thermal expansion coefficient (K^{-1})	Temperature (°C)
3.07E-05	27
3.14E-05	102
3.24E-05	202

3.32E-05	297
3.37E-05	342
3.42E-05	397
3.44E-05	424
3.59E-05	578
0	608

Table 22. Plastic stress-strain behaviour of Mg as a function of temperature and strain rate

Plastic strain rate (s^{-1})	**Yield stress (Pa)**	**Plastic strain**	**Temperature (°C)**
0	2.41E+07	0	25
0	4.51E+07	0.01	25
0	5.65E+07	0.02	25
0	7.80E+07	0.05	25
0	1.01E+08	0.1	25
0	1.30E+08	0.2	25
0	1.84E+08	0.5	25
0	2.40E+08	1	25
0	2.41E+07	0	118
0	4.51E+07	0.01	118
0	5.65E+07	0.02	118
0	7.80E+07	0.05	118
0	1.01E+08	0.1	118
0	1.30E+08	0.2	118
0	1.84E+08	0.5	118
0	2.40E+08	1	118
0	1.74E+07	0	200
0	3.25E+07	0.01	200
0	4.07E+07	0.02	200
0	5.62E+07	0.05	200
0	7.25E+07	0.1	200
0	9.39E+07	0.2	200
0	1.33E+08	0.5	200
0	1.72E+08	1	200
0	1.01E+07	0	300
0	1.89E+07	0.01	300
0	2.37E+07	0.02	300
0	3.28E+07	0.05	300
0	4.23E+07	0.1	300
0	5.48E+07	0.2	300
0	7.74E+07	0.5	300
0	1.01E+08	1	300
0	5.30E+06	0	400
0	9.92E+06	0.01	400
0	1.24E+07	0.02	400

0	1.72E+07	0.05	400
0	2.21E+07	0.1	400
0	2.87E+07	0.2	400
0	4.05E+07	0.5	400
0	5.27E+07	1	400
0	2.89E+06	0	500
0	5.41E+06	0.01	500
0	6.78E+06	0.02	500
0	9.36E+06	0.05	500
0	1.21E+07	0.1	500
0	1.56E+07	0.2	500
0	2.21E+07	0.5	500
0	2.87E+07	1	500
0	1.93E+06	0	578
0	3.61E+06	0.01	578
0	4.52E+06	0.02	578
0	6.24E+06	0.05	578
0	8.05E+06	0.1	578
0	1.04E+07	0.2	578
0	1.47E+07	0.5	578
0	1.92E+07	1	578
0	24110	0	600
0	45105	0.01	600
0	56484	0.02	600
0	78028	0.05	600
0	100658	0.1	600
0	130409	0.2	600
0	184228	0.5	600
0	239527	1	600
0	24110	0	635
0	45105	0.01	635
0	56484	0.02	635
0	78028	0.05	635
0	100658	0.1	635
0	130409	0.2	635
0	184228	0.5	635
0	239527	1	635
0.1	2.81E+07	0	25
0.1	5.25E+07	0.01	25
0.1	6.57E+07	0.02	25
0.1	9.08E+07	0.05	25
0.1	1.17E+08	0.1	25
0.1	1.52E+08	0.2	25
0.1	2.14E+08	0.5	25
0.1	2.79E+08	1	25
0.1	2.81E+07	0	118

0.1	5.25E+07	0.01	118
0.1	6.57E+07	0.02	118
0.1	9.08E+07	0.05	118
0.1	1.17E+08	0.1	118
0.1	1.52E+08	0.2	118
0.1	2.14E+08	0.5	118
0.1	2.79E+08	1	118
0.1	2.02E+07	0	200
0.1	3.78E+07	0.01	200
0.1	4.73E+07	0.02	200
0.1	6.54E+07	0.05	200
0.1	8.44E+07	0.1	200
0.1	1.09E+08	0.2	200
0.1	1.54E+08	0.5	200
0.1	2.01E+08	1	200
0.1	1.18E+07	0	300
0.1	2.20E+07	0.01	300
0.1	2.76E+07	0.02	300
0.1	3.81E+07	0.05	300
0.1	4.92E+07	0.1	300
0.1	6.38E+07	0.2	300
0.1	9.01E+07	0.5	300
0.1	1.17E+08	1	300
0.1	6.17E+06	0	400
0.1	1.15E+07	0.01	400
0.1	1.45E+07	0.02	400
0.1	2.00E+07	0.05	400
0.1	2.58E+07	0.1	400
0.1	3.34E+07	0.2	400
0.1	4.72E+07	0.5	400
0.1	6.13E+07	1	400
0.1	3.37E+06	0	500
0.1	6.30E+06	0.01	500
0.1	7.89E+06	0.02	500
0.1	1.09E+07	0.05	500
0.1	1.41E+07	0.1	500
0.1	1.82E+07	0.2	500
0.1	2.57E+07	0.5	500
0.1	3.35E+07	1	500
0.1	2.81E+06	0	578
0.1	5.25E+06	0.01	578
0.1	6.57E+06	0.02	578
0.1	9.08E+06	0.05	578
0.1	1.17E+07	0.1	578
0.1	1.52E+07	0.2	578
0.1	2.14E+07	0.5	578

0.1	2.79E+07	1	578
0.1	28063	0	600
0.1	52499	0.01	600
0.1	65743	0.02	600
0.1	90820	0.05	600
0.1	117159	0.1	600
0.1	151787	0.2	600
0.1	214429	0.5	600
0.1	278794	1	600
0.1	28063	0	635
0.1	52499	0.01	635
0.1	65743	0.02	635
0.1	90820	0.05	635
0.1	117159	0.1	635
0.1	151787	0.2	635
0.1	214429	0.5	635
0.1	278794	1	635
1	3.52E+07	0	25
1	6.58E+07	0.01	25
1	8.24E+07	0.02	25
1	1.14E+08	0.05	25
1	1.47E+08	0.1	25
1	1.90E+08	0.2	25
1	2.69E+08	0.5	25
1	3.49E+08	1	25
1	3.52E+07	0	118
1	6.58E+07	0.01	118
1	8.24E+07	0.02	118
1	1.14E+08	0.05	118
1	1.47E+08	0.1	118
1	1.90E+08	0.2	118
1	2.69E+08	0.5	118
1	3.49E+08	1	118
1	2.53E+07	0	200
1	4.74E+07	0.01	200
1	5.93E+07	0.02	200
1	8.20E+07	0.05	200
1	1.06E+08	0.1	200
1	1.37E+08	0.2	200
1	1.94E+08	0.5	200
1	2.52E+08	1	200
1	1.48E+07	0	300
1	2.76E+07	0.01	300
1	3.46E+07	0.02	300
1	4.78E+07	0.05	300
1	6.17E+07	0.1	300

1	7.99E+07	0.2	300
1	1.13E+08	0.5	300
1	1.47E+08	1	300
1	7.74E+06	0	400
1	1.45E+07	0.01	400
1	1.81E+07	0.02	400
1	2.50E+07	0.05	400
1	3.23E+07	0.1	400
1	4.19E+07	0.2	400
1	5.91E+07	0.5	400
1	7.69E+07	1	400
1	4.22E+06	0	500
1	7.90E+06	0.01	500
1	9.89E+06	0.02	500
1	1.37E+07	0.05	500
1	1.76E+07	0.1	500
1	2.28E+07	0.2	500
1	3.23E+07	0.5	500
1	4.19E+07	1	500
1	3.52E+06	0	578
1	6.58E+06	0.01	578
1	8.24E+06	0.02	578
1	1.14E+07	0.05	578
1	1.47E+07	0.1	578
1	1.90E+07	0.2	578
1	2.69E+07	0.5	578
1	3.49E+07	1	578
1	35177	0	600
1	65809	0.01	600
1	82411	0.02	600
1	113844	0.05	600
1	146861	0.1	600
1	190269	0.2	600
1	268791	0.5	600
1	349474	1	600
1	35177	0	635
1	65809	0.01	635
1	82411	0.02	635
1	113844	0.05	635
1	146861	0.1	635
1	190269	0.2	635
1	268791	0.5	635
1	349474	1	635
10	4.23E+07	0	25
10	7.91E+07	0.01	25
10	9.91E+07	0.02	25

10	1.37E+08	0.05	25
10	1.77E+08	0.1	25
10	2.29E+08	0.2	25
10	3.23E+08	0.5	25
10	4.20E+08	1	25
10	4.23E+07	0	118
10	7.91E+07	0.01	118
10	9.91E+07	0.02	118
10	1.37E+08	0.05	118
10	1.77E+08	0.1	118
10	2.29E+08	0.2	118
10	3.23E+08	0.5	118
10	4.20E+08	1	118
10	3.04E+07	0	200
10	5.70E+07	0.01	200
10	7.13E+07	0.02	200
10	9.85E+07	0.05	200
10	1.27E+08	0.1	200
10	1.65E+08	0.2	200
10	2.33E+08	0.5	200
10	3.03E+08	1	200
10	1.78E+07	0	300
10	3.32E+07	0.01	300
10	4.16E+07	0.02	300
10	5.75E+07	0.05	300
10	7.42E+07	0.1	300
10	9.61E+07	0.2	300
10	1.36E+08	0.5	300
10	1.76E+08	1	300
10	9.30E+06	0	400
10	1.74E+07	0.01	400
10	2.18E+07	0.02	400
10	3.01E+07	0.05	400
10	3.88E+07	0.1	400
10	5.03E+07	0.2	400
10	7.11E+07	0.5	400
10	9.24E+07	1	400
10	5.07E+06	0	500
10	9.49E+06	0.01	500
10	1.19E+07	0.02	500
10	1.64E+07	0.05	500
10	2.12E+07	0.1	500
10	2.75E+07	0.2	500
10	3.88E+07	0.5	500
10	5.04E+07	1	500
10	4.23E+06	0	578

10	7.91E+06	0.01	578
10	9.91E+06	0.02	578
10	1.37E+07	0.05	578
10	1.77E+07	0.1	578
10	2.29E+07	0.2	578
10	3.23E+07	0.5	578
10	4.20E+07	1	578
10	42292	0	600
10	79118	0.01	600
10	99078	0.02	600
10	136869	0.05	600
10	176563	0.1	600
10	228750	0.2	600
10	323154	0.5	600
10	420154	1	600
10	42292	0	635
10	79118	0.01	635
10	99078	0.02	635
10	136869	0.05	635
10	176563	0.1	635
10	228750	0.2	635
10	323154	0.5	635
10	420154	1	635
100	4.45E+07	0	25
100	8.32E+07	0.01	25
100	1.04E+08	0.02	25
100	1.44E+08	0.05	25
100	1.86E+08	0.1	25
100	2.41E+08	0.2	25
100	3.40E+08	0.5	25
100	4.42E+08	1	25
100	4.45E+07	0	118
100	8.32E+07	0.01	118
100	1.04E+08	0.02	118
100	1.44E+08	0.05	118
100	1.86E+08	0.1	118
100	2.41E+08	0.2	118
100	3.40E+08	0.5	118
100	4.42E+08	1	118
100	3.20E+07	0	200
100	5.99E+07	0.01	200
100	7.50E+07	0.02	200
100	1.04E+08	0.05	200
100	1.34E+08	0.1	200
100	1.73E+08	0.2	200
100	2.45E+08	0.5	200

100	3.18E+08	1	200
100	1.87E+07	0	300
100	3.49E+07	0.01	300
100	4.38E+07	0.02	300
100	6.04E+07	0.05	300
100	7.80E+07	0.1	300
100	1.01E+08	0.2	300
100	1.43E+08	0.5	300
100	1.86E+08	1	300
100	9.78E+06	0	400
100	1.83E+07	0.01	400
100	2.29E+07	0.02	400
100	3.17E+07	0.05	400
100	4.08E+07	0.1	400
100	5.29E+07	0.2	400
100	7.47E+07	0.5	400
100	9.72E+07	1	400
100	5.34E+06	0	500
100	9.98E+06	0.01	500
100	1.25E+07	0.02	500
100	1.73E+07	0.05	500
100	2.23E+07	0.1	500
100	2.89E+07	0.2	500
100	4.08E+07	0.5	500
100	5.30E+07	1	500
100	4.45E+06	0	578
100	8.32E+06	0.01	578
100	1.04E+07	0.02	578
100	1.44E+07	0.05	578
100	1.86E+07	0.1	578
100	2.41E+07	0.2	578
100	3.40E+07	0.5	578
100	4.42E+07	1	578
100	44465	0	600
100	83185	0.01	600
100	104171	0.02	600
100	143904	0.05	600
100	185639	0.1	600
100	240508	0.2	600
100	339764	0.5	600
100	441751	1	600
100	44465	0	635
100	83185	0.01	635
100	104171	0.02	635
100	143904	0.05	635
100	185639	0.1	635

100	240508	0.2	635
100	339764	0.5	635
100	441751	1	635

1.2. Al material *properties*

Table 23. Thermal conductivity of Al as a function of temperature

Thermal conductivity (S/m)	**Temperature (°C)**
295.8974	22.98507
289.7436	45.97015
280	100.2985
265.641	152.5373
261.5385	198.5075
256.4103	252.8358
252.8205	300.8955
251.7949	348.9552
248.7179	401.194
246.6667	426.2687
244.6154	468.0597
243.0769	501.4925
241.5385	524.4776
238.9744	564.1791
232.8205	620.597
230.2564	656.1194
95.38462	660
97.4359	700
99.48718	762.6866

Table 24. Young's modulus of Al as a function of temperature

Young's modulus (Pa)	**Poisson ratio**	**Temperature (°C)**
5.45E+10	0.36	12
5.28E+10	0.36	60
5.16E+10	0.36	140
4.65E+10	0.36	215
4.09E+10	0.36	290
3.32E+10	0.36	372
2.43E+10	0.36	445

Table 25. Thermal expansion coefficient of Al as a function of temperature

Thermal expansion coefficient (K^{-1})	**Temperature (°C)**
3.07E-05	27
3.14E-05	102

3.24E-05	202
3.32E-05	297
3.37E-05	342
3.42E-05	397
3.44E-05	424
3.59E-05	578
0	660

Table 26. Specific heat capacity of Al as a function of temperature

Specific heat capacity (J/(kg·K))	Temperature (°C)
1063.457	375
1086.407	425
1109.357	475
1132.307	525
1155.257	575
1178.206	625
1193.812	659
1085.464	660
1085.464	710
1085.464	760
1085.464	810
1085.464	860
1085.464	910
1085.464	1000

Table 27. Plastic stress-strain behaviour of Mg as a function of temperature

Yield stress (Pa)	Plastic strain	Temperature (°C)
2.62E+07	0	26.85
3.03E+07	0.01	26.85
3.56E+07	0.02	26.85
4.43E+07	0.05	26.85
5.24E+07	0.1	26.85
2.14E+07	0	126.85
2.41E+07	0.01	126.85
2.74E+07	0.02	126.85
3.30E+07	0.05	126.85
3.86E+07	0.1	126.85
4.34E+07	0.2	126.85
1.10E+07	0	249.85
1.20E+07	0.01	249.85

1.37E+07	0.02	249.85
1.62E+07	0.05	249.85
1.86E+07	0.1	249.85
2.08E+07	0.2	249.85
6.34E+06	0	349.85
6.89E+06	0.01	349.85
7.52E+06	0.02	349.85
8.34E+06	0.05	349.85
8.96E+06	0.1	349.85
9.17E+06	0.2	349.85
8.83E+06	0.3	349.85
2.55E+06	0	499.85
2.76E+06	0.01	499.85
2.90E+06	0.02	499.85
3.03E+06	0.05	499.85
1.79E+06	0	599.85
1.83E+06	0.01	599.85
1.83E+06	0.02	599.85
1.82E+06	0.05	599.85

1.3. AZ31 material *properties*

Table 28. Thermal conductivity of AZ31 as a function of temperature

Thermal conductivity (S/m)	**Temperature (°C)**
1063.457	375
1086.407	425
1109.357	475
1132.307	525
1155.257	575
1178.206	625
1193.812	659
1085.464	660
1085.464	710
1085.464	760
1085.464	810
1085.464	860
1085.464	910
1085.464	1000

Table 29. Young’s modulus of AZ31 as a function of temperature

Young’s modulus (Pa)	**Poisson ratio**	**Temperature (°C)**
4.5E+10	0.33	27
4.3E+10	0.33	102
4.1E+10	0.33	202

3.8E+10	0.33	297
3.7E+10	0.33	342
3.55E+10	0.33	397
3.45E+10	0.33	424
1.5E+10	0.33	578
1E+09	0.33	608

Table 30. Thermal expansion coefficient of AZ31 as a function of temperature

Thermal expansion coefficient (K^{-1})	Temperature (°C)
3.07E-05	27
3.14E-05	102
3.24E-05	202
3.32E-05	297
3.37E-05	342
3.42E-05	397
3.44E-05	424
3.59E-05	578
0	608

Table 31. Specific heat capacity of AZ31 as a function of temperature

Specific heat capacity (J/(kg·K))	Temperature (°C)
1005.9	25
1031.9	100
1049.3	200
1068.9	300
1091.9	400

Table 32. Plastic stress-strain behaviour of AZ31 as a function of temperature and strain rate

Plastic strain rate (s^{-1})	Yield stress (Pa)	Plastic strain	Temperature (°C)
0	24110100	0	25
0	45104800	0.01	25
0	56483800	0.02	25
0	78028100	0.05	25
0	1.01E+08	0.1	25
0	1.3E+08	0.2	25
0	1.84E+08	0.5	25
0	2.4E+08	1	25
0.1	28062600	0	25
0.1	52499000	0.01	25
0.1	65743400	0.02	25
0.1	90819600	0.05	25
0.1	1.17E+08	0.1	25

0.1	1.52E+08	0.2	25
0.1	2.14E+08	0.5	25
0.1	2.79E+08	1	25
1	35177100	0	25
1	65808600	0.01	25
1	82410700	0.02	25
1	1.14E+08	0.05	25
1	1.47E+08	0.1	25
1	1.9E+08	0.2	25
1	2.69E+08	0.5	25
1	3.49E+08	1	25
10	42291600	0	25
10	79118200	0.01	25
10	99078100	0.02	25
10	1.37E+08	0.05	25
10	1.77E+08	0.1	25
10	2.29E+08	0.2	25
10	3.23E+08	0.5	25
10	4.2E+08	1	25
100	44465400	0	25
100	83185000	0.01	25
100	1.04E+08	0.02	25
100	1.44E+08	0.05	25
100	1.86E+08	0.1	25
100	2.41E+08	0.2	25
100	3.4E+08	0.5	25
100	4.42E+08	1	25
0	24110100	0	118
0	45104800	0.01	118
0	56483800	0.02	118
0	78028100	0.05	118
0	1.01E+08	0.1	118
0	1.3E+08	0.2	118
0	1.84E+08	0.5	118
0	2.4E+08	1	118
0.1	28062600	0	118
0.1	52499000	0.01	118
0.1	65743400	0.02	118
0.1	90819600	0.05	118
0.1	1.17E+08	0.1	118
0.1	1.52E+08	0.2	118
0.1	2.14E+08	0.5	118
0.1	2.79E+08	1	118
1	35177100	0	118
1	65808600	0.01	118
1	82410700	0.02	118

1	1.14E+08	0.05	118
1	1.47E+08	0.1	118
1	1.9E+08	0.2	118
1	2.69E+08	0.5	118
1	3.49E+08	1	118
10	42291600	0	118
10	79118200	0.01	118
10	99078100	0.02	118
10	1.37E+08	0.05	118
10	1.77E+08	0.1	118
10	2.29E+08	0.2	118
10	3.23E+08	0.5	118
10	4.2E+08	1	118
100	44465400	0	118
100	83185000	0.01	118
100	1.04E+08	0.02	118
100	1.44E+08	0.05	118
100	1.86E+08	0.1	118
100	2.41E+08	0.2	118
100	3.4E+08	0.5	118
100	4.42E+08	1	118
0	17359300	0	200
0	32475400	0.01	200
0	40668300	0.02	200
0	56180200	0.05	200
0	72473500	0.1	200
0	93894400	0.2	200
0	1.33E+08	0.5	200
0	1.72E+08	1	200
0.1	20205100	0	200
0.1	37799300	0.01	200
0.1	47335200	0.02	200
0.1	65390100	0.05	200
0.1	84354400	0.1	200
0.1	1.09E+08	0.2	200
0.1	1.54E+08	0.5	200
0.1	2.01E+08	1	200
1	25327500	0	200
1	47382200	0.01	200
1	59335700	0.02	200
1	81967900	0.05	200
1	1.06E+08	0.1	200
1	1.37E+08	0.2	200
1	1.94E+08	0.5	200
1	2.52E+08	1	200
10	30449900	0	200

10	56965100	0.01	200
10	71336200	0.02	200
10	98545700	0.05	200
10	1.27E+08	0.1	200
10	1.65E+08	0.2	200
10	2.33E+08	0.5	200
10	3.03E+08	1	200
100	32015100	0	200
100	59893200	0.01	200
100	75003000	0.02	200
100	1.04E+08	0.05	200
100	1.34E+08	0.1	200
100	1.73E+08	0.2	200
100	2.45E+08	0.5	200
100	3.18E+08	1	200
0	10126300	0	300
0	18944000	0.01	300
0	23723200	0.02	300
0	32771800	0.05	300
0	42276200	0.1	300
0	54771700	0.2	300
0	77375600	0.5	300
0	1.01E+08	1	300
0.1	11786300	0	300
0.1	22049600	0.01	300
0.1	27612200	0.02	300
0.1	38144200	0.05	300
0.1	49206800	0.1	300
0.1	63750700	0.2	300
0.1	90060200	0.5	300
0.1	1.17E+08	1	300
1	14774400	0	300
1	27639600	0.01	300
1	34612500	0.02	300
1	47814600	0.05	300
1	61681700	0.1	300
1	79912900	0.2	300
1	1.13E+08	0.5	300
1	1.47E+08	1	300
10	17762500	0	300
10	33229600	0.01	300
10	41612800	0.02	300
10	57485000	0.05	300
10	74156700	0.1	300
10	96075000	0.2	300
10	1.36E+08	0.5	300

10	1.76E+08	1	300
100	18675500	0	300
100	34937700	0.01	300
100	43751800	0.02	300
100	60439800	0.05	300
100	77968500	0.1	300
100	1.01E+08	0.2	300
100	1.43E+08	0.5	300
100	1.86E+08	1	300
0	5304230	0	400
0	9923050	0.01	400
0	12426400	0.02	400
0	17166200	0.05	400
0	22144700	0.1	400
0	28690000	0.2	400
0	40530100	0.5	400
0	52696000	1	400
0.1	6173780	0	400
0.1	11549800	0.01	400
0.1	14463500	0.02	400
0.1	19980300	0.05	400
0.1	25775000	0.1	400
0.1	33393200	0.2	400
0.1	47174400	0.5	400
0.1	61334600	1	400
1	7738960	0	400
1	14477900	0.01	400
1	18130400	0.02	400
1	25045700	0.05	400
1	32309500	0.1	400
1	41859100	0.2	400
1	59134100	0.5	400
1	76884300	1	400
10	9304150	0	400
10	17406000	0.01	400
10	21797200	0.02	400
10	30111200	0.05	400
10	38844000	0.1	400
10	50325000	0.2	400
10	71093800	0.5	400
10	92433900	1	400
100	9782400	0	400
100	18300700	0.01	400
100	22917600	0.02	400
100	31659000	0.05	400
100	40840600	0.1	400

100	52911800	0.2	400
100	74748100	0.5	400
100	97185200	1	400
0	2893220	0	500
0	5412570	0.01	500
0	6778050	0.02	500
0	9363370	0.05	500
0	12078900	0.1	500
0	15649100	0.2	500
0	22107300	0.5	500
0	28743200	1	500
0.1	3367520	0	500
0.1	6299880	0.01	500
0.1	7889210	0.02	500
0.1	10898400	0.05	500
0.1	14059100	0.1	500
0.1	18214500	0.2	500
0.1	25731500	0.5	500
0.1	33455300	1	500
1	4221250	0	500
1	7897030	0.01	500
1	9889290	0.02	500
1	13661300	0.05	500
1	17623300	0.1	500
1	22832300	0.2	500
1	32254900	0.5	500
1	41936900	1	500
10	5074990	0	500
10	9494180	0.01	500
10	11889400	0.02	500
10	16424300	0.05	500
10	21187600	0.1	500
10	27450000	0.2	500
10	38778400	0.5	500
10	50418500	1	500
100	5335850	0	500
100	9982200	0.01	500
100	12500500	0.02	500
100	17268500	0.05	500
100	22276700	0.1	500
100	28861000	0.2	500
100	40771700	0.5	500
100	53010100	1	500
0	1928810	0	578
0	3608380	0.01	578
0	4518700	0.02	578

0	6242250	0.05	578
0	8052620	0.1	578
0	10432700	0.2	578
0	14738200	0.5	578
0	19162200	1	578
0.1	2806260	0	578
0.1	5249900	0.01	578
0.1	6574340	0.02	578
0.1	9081960	0.05	578
0.1	11715900	0.1	578
0.1	15178700	0.2	578
0.1	21442900	0.5	578
0.1	27879400	1	578
1	3517710	0	578
1	6580860	0.01	578
1	8241070	0.02	578
1	11384400	0.05	578
1	14686100	0.1	578
1	19026900	0.2	578
1	26879100	0.5	578
1	34947400	1	578
10	4229160	0	578
10	7911820	0.01	578
10	9907810	0.02	578
10	13686900	0.05	578
10	17656300	0.1	578
10	22875000	0.2	578
10	32315400	0.5	578
10	42015400	1	578
100	4446540	0	578
100	8318500	0.01	578
100	10417100	0.02	578
100	14390400	0.05	578
100	18563900	0.1	578
100	24050800	0.2	578
100	33976400	0.5	578
100	44175100	1	578
0	24110	0	600
0	45105	0.01	600
0	56484	0.02	600
0	78028	0.05	600
0	100658	0.1	600
0	130409	0.2	600
0	184228	0.5	600
0	239527	1	600
0.1	28063	0	600

0.1	52499	0.01	600
0.1	65743	0.02	600
0.1	90820	0.05	600
0.1	117159	0.1	600
0.1	151787	0.2	600
0.1	214429	0.5	600
0.1	278794	1	600
1	35177	0	600
1	65809	0.01	600
1	82411	0.02	600
1	113844	0.05	600
1	146861	0.1	600
1	190269	0.2	600
1	268791	0.5	600
1	349474	1	600
10	42292	0	600
10	79118	0.01	600
10	99078	0.02	600
10	136869	0.05	600
10	176563	0.1	600
10	228750	0.2	600
10	323154	0.5	600
10	420154	1	600
100	44465	0	600
100	83185	0.01	600
100	104171	0.02	600
100	143904	0.05	600
100	185639	0.1	600
100	240508	0.2	600
100	339764	0.5	600
100	441751	1	600
0	24110	0	635
0	45105	0.01	635
0	56484	0.02	635
0	78028	0.05	635
0	100658	0.1	635
0	130409	0.2	635
0	184228	0.5	635
0	239527	1	635
0.1	28063	0	635
0.1	52499	0.01	635
0.1	65743	0.02	635
0.1	90820	0.05	635
0.1	117159	0.1	635
0.1	151787	0.2	635
0.1	214429	0.5	635

0.1	278794	1	635
1	35177	0	635
1	65809	0.01	635
1	82411	0.02	635
1	113844	0.05	635
1	146861	0.1	635
1	190269	0.2	635
1	268791	0.5	635
1	349474	1	635
10	42292	0	635
10	79118	0.01	635
10	99078	0.02	635
10	136869	0.05	635
10	176563	0.1	635
10	228750	0.2	635
10	323154	0.5	635
10	420154	1	635
100	44465	0	635
100	83185	0.01	635
100	104171	0.02	635
100	143904	0.05	635
100	185639	0.1	635
100	240508	0.2	635
100	339764	0.5	635
100	441751	1	635